



AFRL-AFOSR-VA-TR-2015-0306

Uncovering and Validating Toughening Mechanisms in High Performance Composites

David Kisailus
REGENTS OF THE UNIVERSITY OF CALIFORNIA AT RIVERSIDE

09/17/2015
Final Report

DISTRIBUTION A: Distribution approved for public release.

Air Force Research Laboratory
AF Office Of Scientific Research (AFOSR)/ RTB2
Arlington, Virginia 22203
Air Force Materiel Command

REPORT DOCUMENTATION PAGE		Form Approved OMB No. 0704-0188	
<p>The public reporting burden for this collection of information is estimated to average 1 hour per response, including the time for reviewing instructions, searching existing data sources, gathering and maintaining the data needed, and completing and reviewing the collection of information. Send comments regarding this burden estimate or any other aspect of this collection of information, including suggestions for reducing the burden, to Department of Defense, Executive Services, Directorate (0704-0188). Respondents should be aware that notwithstanding any other provision of law, no person shall be subject to any penalty for failing to comply with a collection of information if it does not display a currently valid OMB control number.</p> <p>PLEASE DO NOT RETURN YOUR FORM TO THE ABOVE ORGANIZATION.</p>			
1. REPORT DATE (DD-MM-YYYY)		2. REPORT TYPE Final Performance	
		3. DATES COVERED (From - To) 15-05-2012 to 14-05-2015	
4. TITLE AND SUBTITLE Uncovering and Validating Toughening Mechanisms in High Performance Composites		5a. CONTRACT NUMBER	
		5b. GRANT NUMBER FA9550-12-1-0245	
		5c. PROGRAM ELEMENT NUMBER 61102F	
6. AUTHOR(S) David Kisailus		5d. PROJECT NUMBER	
		5e. TASK NUMBER	
		5f. WORK UNIT NUMBER	
7. PERFORMING ORGANIZATION NAME(S) AND ADDRESS(ES) REGENTS OF THE UNIVERSITY OF CALIFORNIA AT RIVERSIDE 200 UNIVERSITY OFFICE BLDG RIVERSIDE, CA 925210001 US		8. PERFORMING ORGANIZATION REPORT NUMBER	
9. SPONSORING/MONITORING AGENCY NAME(S) AND ADDRESS(ES) AF Office of Scientific Research 875 N. Randolph St. Room 3112 Arlington, VA 22203		10. SPONSOR/MONITOR'S ACRONYM(S) AFRL/AFOSR RTB2	
		11. SPONSOR/MONITOR'S REPORT NUMBER(S)	
12. DISTRIBUTION/AVAILABILITY STATEMENT A DISTRIBUTION UNLIMITED: PB Public Release			
13. SUPPLEMENTARY NOTES			
14. ABSTRACT <p>The research goal of this project is to study and understand the structure-function relationships in damage-tolerant impact/shock-resistant stomatopod dactyl club while addressing the ongoing quest to develop the new generation of scalable high-performance biologically-inspired multifunctional materials. Our ultrastructural investigations have identified that within this multi-regional composite structure, specific regions play very specific roles. We uncovered structural details from the striated region, which exists on the sides of the club. Unidirectional mineralized fibers in this region wrap circumferentially around the club, keeping it under compression during impact and preventing crack growth. To confirm this, we produced new models at multiple length scales and across length scales to show the effects of this outer layer. We compared this to the spearing dactyl of another species of mantis, in which this striated region is located on all sides (supporting flexural loads). We also observed a unique structure within the impact region of the dactyl. Specifically, the helicoidal structure previously identified in the periodic region extended into the impact region with a change in periodicity and forming a herringbone-like structure based on compression of this helicoid. Evidence is provided for the effects of this herringbone structure, which in combination with an outer dense particulate apatite layer, enhances stress redistribution under compressive loading. Within the periodic region, which contains the helicoidal structure, we observed that the periodicity enables not only crack twisting, which toughens the club, but also shear wave filtering, as confirmed using analytical models. In addition, we have fabricated carbon fiber based biomimetic composites that recreate the structure within periodic region in order to highlight its ability to absorb energy by re</p>			
15. SUBJECT TERMS Biomaterials, biocomposite, cavitation			

16. SECURITY CLASSIFICATION OF:			17. LIMITATION OF ABSTRACT	18. NUMBER OF PAGES	19a. NAME OF RESPONSIBLE PERSON
a. REPORT	b. ABSTRACT	c. THIS PAGE			David Kisailus
Unclassified	Unclassified	Unclassified	UU		19b. TELEPHONE NUMBER (Include area code) 951-827-2260

Final Report (August 2015)

Uncovering and Validating Toughening Mechanisms in High Performance Composites

FA9550-12-1-0245

PI: David Kisailus, UC Riverside

Co-PI: Pablo Zavattieri, Purdue University

Abstract

Based on the three years of this project, we have been largely successful in staying on schedule and achieving the milestones outlined in the proposal. The research goal of this project is to study and understand the structure-function relationships in damage-tolerant impact/shock-resistant stomatopod dactyl club while addressing the ongoing quest to develop the new generation of scalable high-performance *biologically-inspired* multifunctional materials. We achieved this by (i) providing details of the nano- and microstructural features of the stomatopod dactyl clubs with state-of-the-art microscopy and synchrotron x-ray studies, (ii) deriving the structure-property relationship through a combined experimental/ computational methodology to properly characterize the mechanical properties of the different regions of the dactyl club and (iii) studying the multiscale hierarchical structure of the periodic region to elucidate critical energy and shock mitigation mechanisms. Our ultrastructural investigations have identified that within this multi-regional composite structure, specific regions play very specific roles. We uncovered structural details from the striated region, which exists on the sides of the club. Unidirectional mineralized fibers in this region wrap circumferentially around the club, keeping it under compression during impact and preventing crack growth. To confirm this, we produced new models at multiple length scales and across length scales to show the effects of this outer layer. We compared this to the spearing dactyl of another species of mantis, in which this striated region is located on all sides (supporting flexural loads). We also observed a unique structure within the impact region of the dactyl. Specifically, the helicoidal structure previously identified in the periodic region extended into the impact region with a change in periodicity and forming a herringbone-like structure based on compression of this helicoid. Evidence is provided for the effects of this “herringbone structure”, which in combination with an outer dense particulate apatite layer, enhances stress redistribution under compressive loading. Within the periodic region, which contains the helicoidal structure, we observed that the periodicity enables not only crack twisting (as demonstrated by models and 3D printed samples), which toughens the club, but also shear wave filtering, as confirmed using analytical models. In addition, we have fabricated carbon fiber based biomimetic composites that recreate the structure within periodic region in order to highlight its ability to absorb energy by redistributing impact. These biomimetic composites outperformed those used in the aircraft industry (e.g., quasi-isotropic found in Boeing and Airbus commercial aircraft) by 49% (based on dent-depth) and more than 15% higher compressive strength after impact. We have also identified macro-morphological designs that reduce hydrodynamic drag over ballistic forms and initiated observations for the telson and merus regions of the mantis. We have published multiple papers in high impact journals, graduated multiple Ph.D. students, mentored post-doctoral and undergraduate students and held outreach events involving middle school students and the general public. Finally, new interactions with other investigators have lead to new research directions.

Overall objectives

The mineralized dactyl club of the raptorial appendages can inflict significant damage to its prey. These formidable structures are capable of accelerations to 10,400 g and speeds of 23 m/s from a standing start [Patek, S.N., Korff, W.L. & Caldwell, R.L. Biomechanics: Deadly strike mechanism of a mantis shrimp - This shrimp packs a punch powerful enough to smash its prey's shell underwater. *Nature* **428**, 819-820 (2004).] Because of their rapid strike, they can generate cavitation bubbles between the appendage and the striking surface. The collapse of these cavitation bubbles produces significant forces on the prey in addition to the instantaneous forces of 1,500 N that are caused by the direct impact of the dactyl club [Patek, S.N. & Caldwell, R.L. Extreme impact and cavitation forces of a biological hammer: strike forces of the peacock mantis shrimp *Odontodactylus scyllarus*. *Journal of Experimental Biology* **208**, 3655-3664 (2005).] Despite these significant forces, the dactyl clubs are extremely fracture-resistant and are able to tolerate thousands of highly energetic blows, a characteristic that can be directly linked to their ultrastructural features that impart exceptionally high strength, stiffness, and toughness. We investigated the underlying structures and mechanics that yield this incredibly strong and tough composite.

Thus, the overall objectives of this project were to (i) provide details of the nano- and microstructural features of the stomatopod dactyl clubs with state-of-the-art microscopy and synchrotron x-ray studies, (ii) derive the structure-property relationship through a combined experimental/ computational methodology to properly characterize the mechanical properties of the different regions of the dactyl club, (iii) study the multiscale hierarchical structure of the periodic region to elucidate critical energy and shock mitigation mechanisms.

We achieved this by (i) acquiring high-resolution, three-dimensional chemical and phase maps of the nano- and microstructural features in the impact, periodic and striated regions of the dactyl club, (ii) conducting combined multiscale experimental/computational mechanical investigation of regional structures, (iii) resolving the detailed structural features and multiscale mechanics of the hierarchical assembled organic scaffold within the primary energy absorption region of the club using state-of-the-art microscopy, experimental techniques and computational modeling from the atomistic scale to the mm-scale and (iv) directing a biomimetic effort aimed at elucidating toughening features of the dactyl club.

Over the span of this project, we have accomplished the majority of these objectives. We report accomplishments by each task, specifically highlighting each accomplishment.

Accomplishments of Specific objectives:

During the course of this project, specimens of *Odontodactylus scyllarus* were collected from the tropical Western Pacific and were maintained in an environmentally controlled closed-loop seawater system in the Kisailus Lab at UCR until they were ready for use. Thus, specimens were kept in prime condition for analyses including maintained hydration of specimens. Stomatopods used in this study were adult individuals measuring between 7.5 and 12.5cm in total length. The clubs that were separated from the stomatopods were between 3 – 5 mm in diameter, enabling ease of analyses.

Acquire high-resolution, three-dimensional chemical and phase maps of the nano- and microstructural features in the impact, periodic and striated regions of the dactyl club.

During the duration of this project, we have utilized dactyl clubs from more than 50 stomatopods. Each stomatopod was contained in the same close-looped system and had the same feeding schedule to maintain a similar growth environment. Here, microscopic and spectroscopic techniques were used to uncover ultrastructural features that yield a remarkable tough and strong structure.

Intact dactyl clubs (Figure 1) were investigated by a combination of techniques. Initially, a cross-section of the stomatopod including body and clubs was investigated by μ -CT scans (Figure 2). This revealed the heavily mineralized nature of the club with respect to the rest of the body.

In addition, we embedded clubs in Spurr's epoxy resin and subsequently cut into longitudinal and cross-sectional slices (Figure 3) using a diamond cutting wheel and polished with lapping films down to a 0.1 mm grit size for optical microscopy, high-resolution SEM imaging, energy

dispersive spectroscopy and other spectroscopic and mechanical analyses. In addition, high resolution and backscattered SEM were used to investigate the presence of structural and compositional boundaries within these three regions of the dactyl club and spatially correlated with the elemental spectroscopy data.



Figure 1. Stomatopod with exposed dactyl clubs highlighted with white arrows.

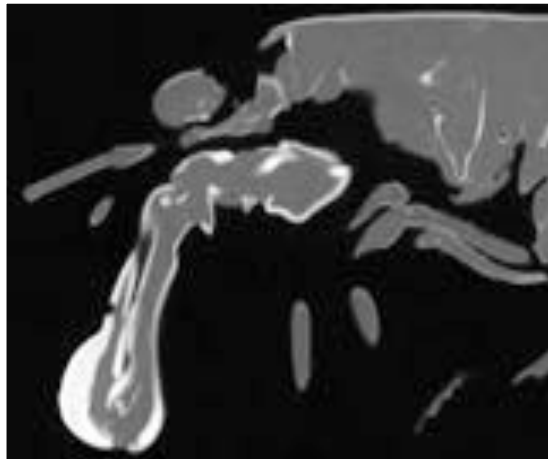


Figure 2. μ -CT imaging of a cross-sectional body plan of the stomatopod, highlighting the heavily mineralized dactyl club.

Cross-sectional imaging highlights the combined dactyl (D) plus propodus (P) (Figure 3) structure.

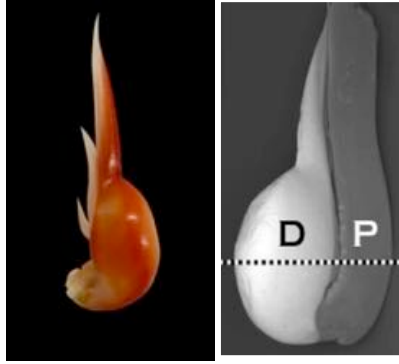


Figure 3. Dactyl plus propodus structure. (left) Optical micrograph showing intact dactyl where cross-sectioning was performed. (right) Schematic of cross-section of dactyl plus propodus.

After performing cross-sectioning, Back-scatter electron microscopy confirmed a highly mineralized outer region within the dactyl club (Figure 4) as well as two additional regions within the club (directly beneath the outer, impact region as well as on the sides of the club). These regions (impact, periodic and striated) were further highlighted using optical microscopy (Figure 5).

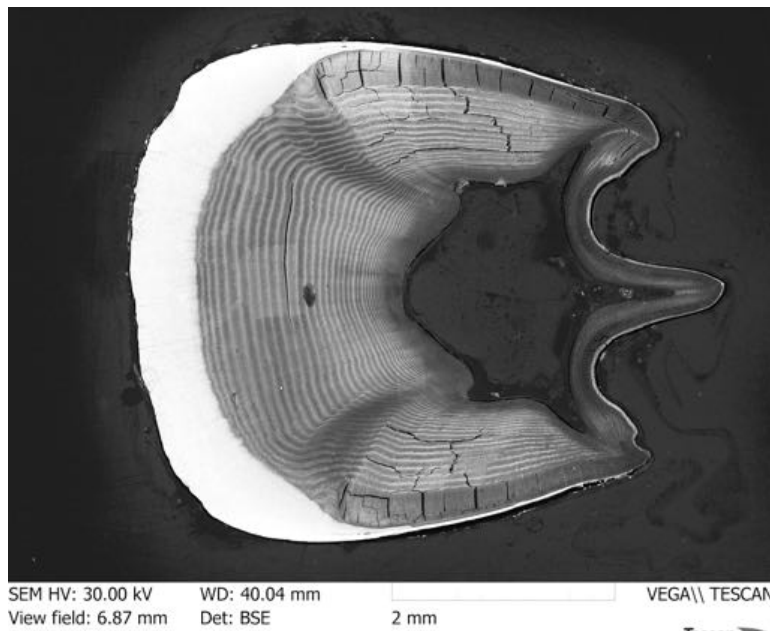
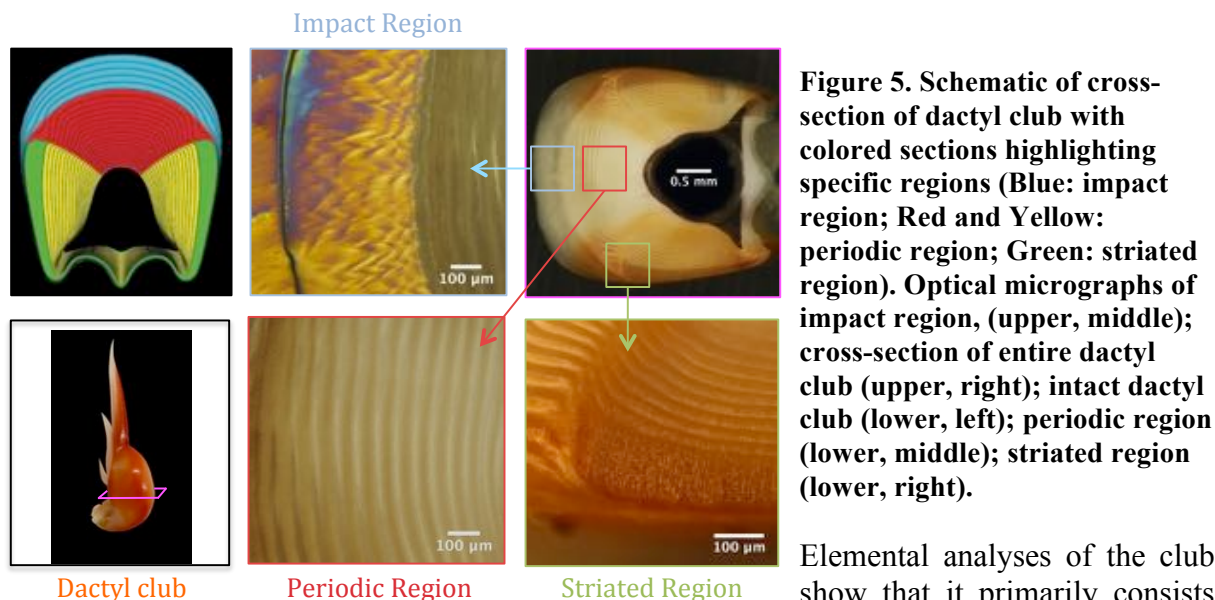


Figure 4. Back scatter electron micrograph of cross-section of dactyl club. White region on the left is the impact region. Immediately beneath the impact region is the periodic region and on the sides of the club are the striated regions.



Elemental analyses of the club show that it primarily consists of Calcium and Phosphorus (Figure 6), confirming previous XRD analyses which showed the presence of crystalline hydroxylapatite [Weaver, J., Milliron, G., Miserez, A., Evans-Lutterodt, K., Herrera, S., Gallana, I., Mershon, W., Swanson, B., Zavattieri, P., DiMasi, E., Kisailus, D., “The Stomatopod Dactyl Club: A Formidable Damage-Tolerant Biological Hammer,” *Science*, **336** (2012) 1275-1280.]



The presence of magnesium is known to stabilize amorphous calcium phosphate and will be discussed more in the periodic region section. Sulfur is likely present as a modified organic (e.g., sulfated polysaccharide) that guides nucleation and growth of the crystalline calcium phosphate.

Previous work had shown that the different regions of the dactyl club consisted of varying content of crystalline and amorphous calcium phosphate and calcium carbonates (Figure 7, [Weaver, J., Milliron, G., Miserez, A., Evans-Lutterodt, K., Herrera, S., Gallana, I., Mershon, W., Swanson, B., Zavattieri, P., DiMasi, E., Kisailus, D., “The Stomatopod Dactyl Club: A Formidable Damage-Tolerant Biological Hammer,” *Science*, **336** (2012) 1275-1280].

Figure 6. Elemental analysis of cross-section of dactyl club via EDS. Back-scatter electron micrograph highlighting mineral rich impact region (upper, left); optical micrograph (upper, right); Calcium map (middle, left); Phosphorus map (middle, right); Magnesium map (lower, left); Sulfur map (lower, right).

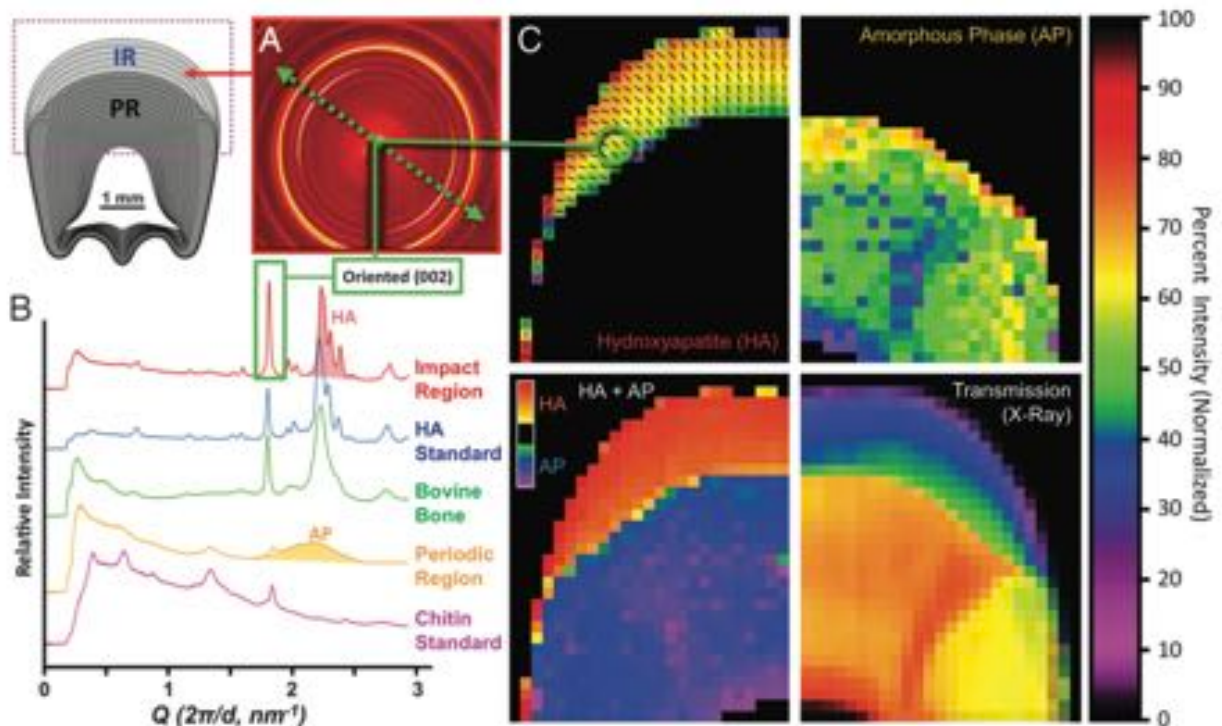


Figure 7. Synchrotron X-ray analyses revealing a highly oriented (along the (002) direction) hydroxylapatite structure within the impact region and an amorphous structure in the periodic and striated regions.

Further investigations of each region within the dactyl club are described below.

Impact region:

Initial analysis (in year 1) of a powdered sample of the impact region revealed the presence of hydroxyapatite (HAP, from $\text{Ca}_{10}(\text{PO}_4)_6(\text{OH})_2$, Figure 8). A geological HAP standard confirmed this phase and the increased full width at half maximum (FWHM) indicates a decreased crystallite size versus the geological standard. This is common for grain sizes of mineral to be smaller than their geological counterparts since organic templates often exist to reduce barriers for nucleation and thus yield smaller crystallites.

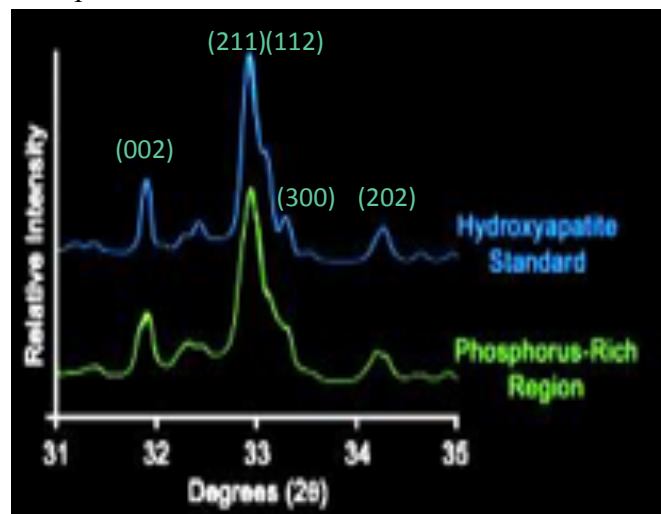


Figure 8. Powder X-ray diffraction of impact region of dactyl club.

Raman spectroscopy confirmed the XRD observation (Figure 9).

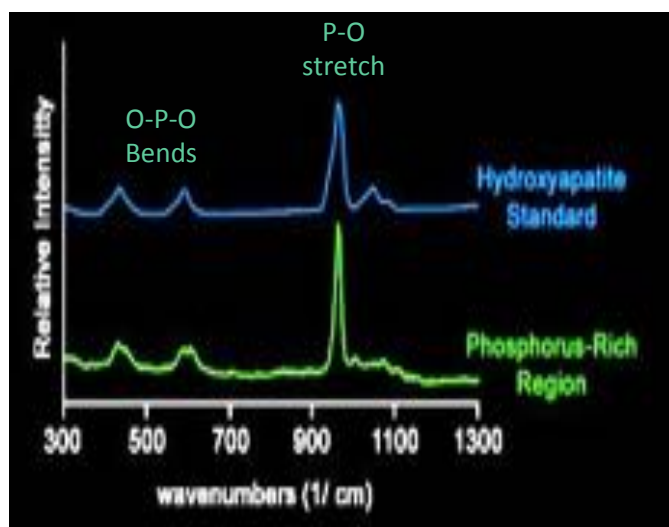


Figure 9. Raman spectroscopy of impact region of dactyl club.

In order to determine if there is a preferred orientation within the club, a cross-section of the club was placed in a synchrotron. A $100\text{ }\mu\text{m}$ beam was used to map the club (Figure 10). Each pixel within this figure represents an individual diffraction frame of that region within the club. The region in yellow, which represents a lower transmission intensity (due to increased scattering) is the impact region of the club. Here, it was determined that the (002) HAP planes were oriented perpendicular to the surface of the club. An individual synchrotron frame is also shown (Figure 11) to highlight this preferred orientation.

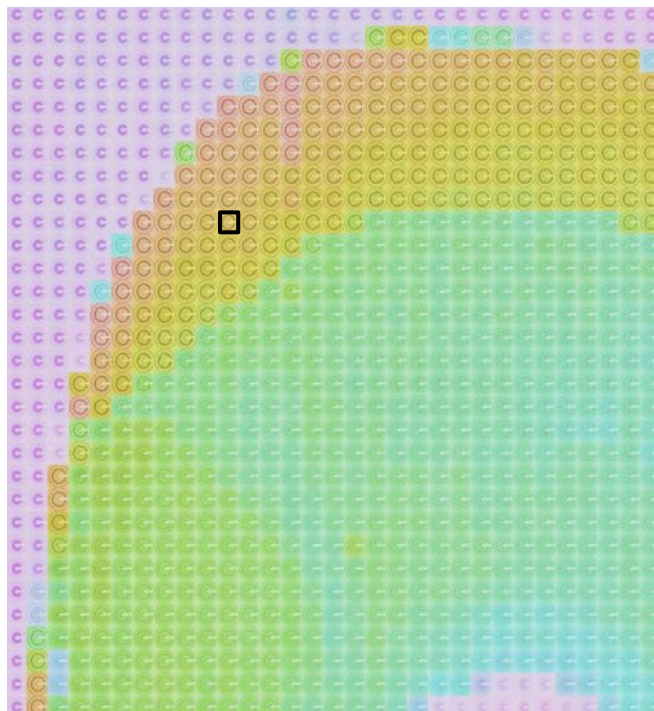


Figure 10. Synchrotron X-ray map of a cross section of the dactyl club. Each pixel represents a $100\text{ }\mu\text{m} \times 100\text{ }\mu\text{m}$ region. The impact region is clearly distinguishable (yellow) from the rest of the club.

In addition to the preferred orientation of the (002) HAP planes, faint rings are observed that likely represent the chitinous organic, which in combination with peptides (that are likely co-located with structural organic), template the formation and guide the orientation of HAP.

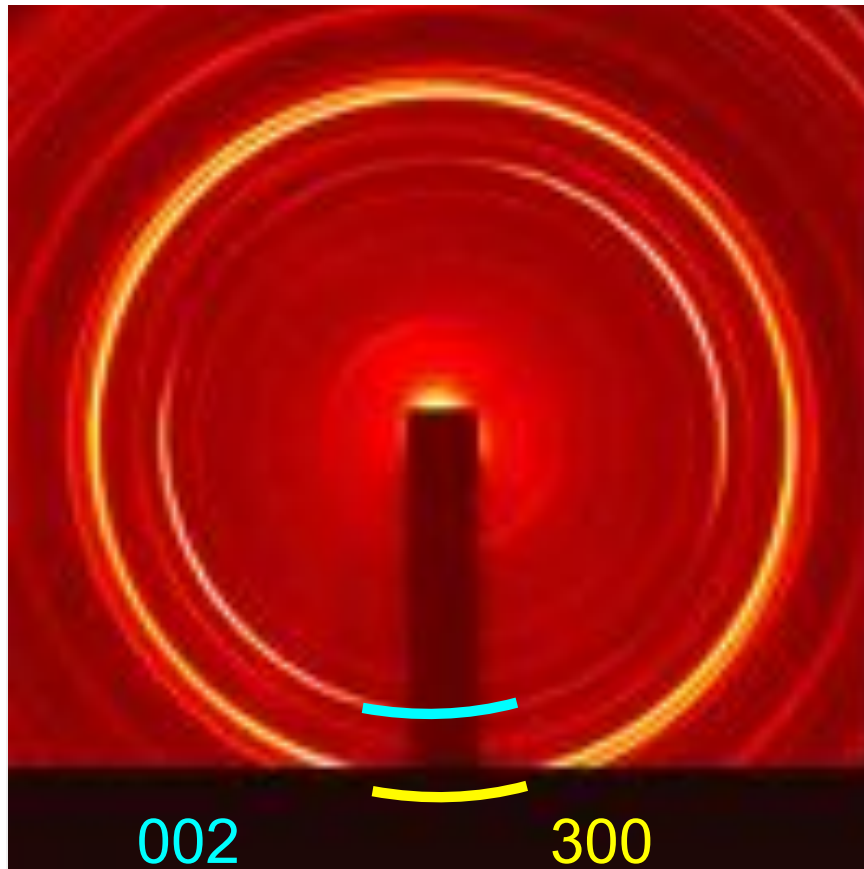


Figure 11. Individual Synchrotron X-ray diffraction frame from the dactyl club map in Figure 10 (selected pixel highlighted in black). The (002) planes display a preferred orientation. Faint inner arcs represent organic (chitin).

In year 2 of this project, we revealed more details about the impact region of the dactyl club. Specifically, optical analyses of the club from different perspectives: transverse, sagittal and coronal revealed a *herringbone-like* structure within the impact region (Figure 12).

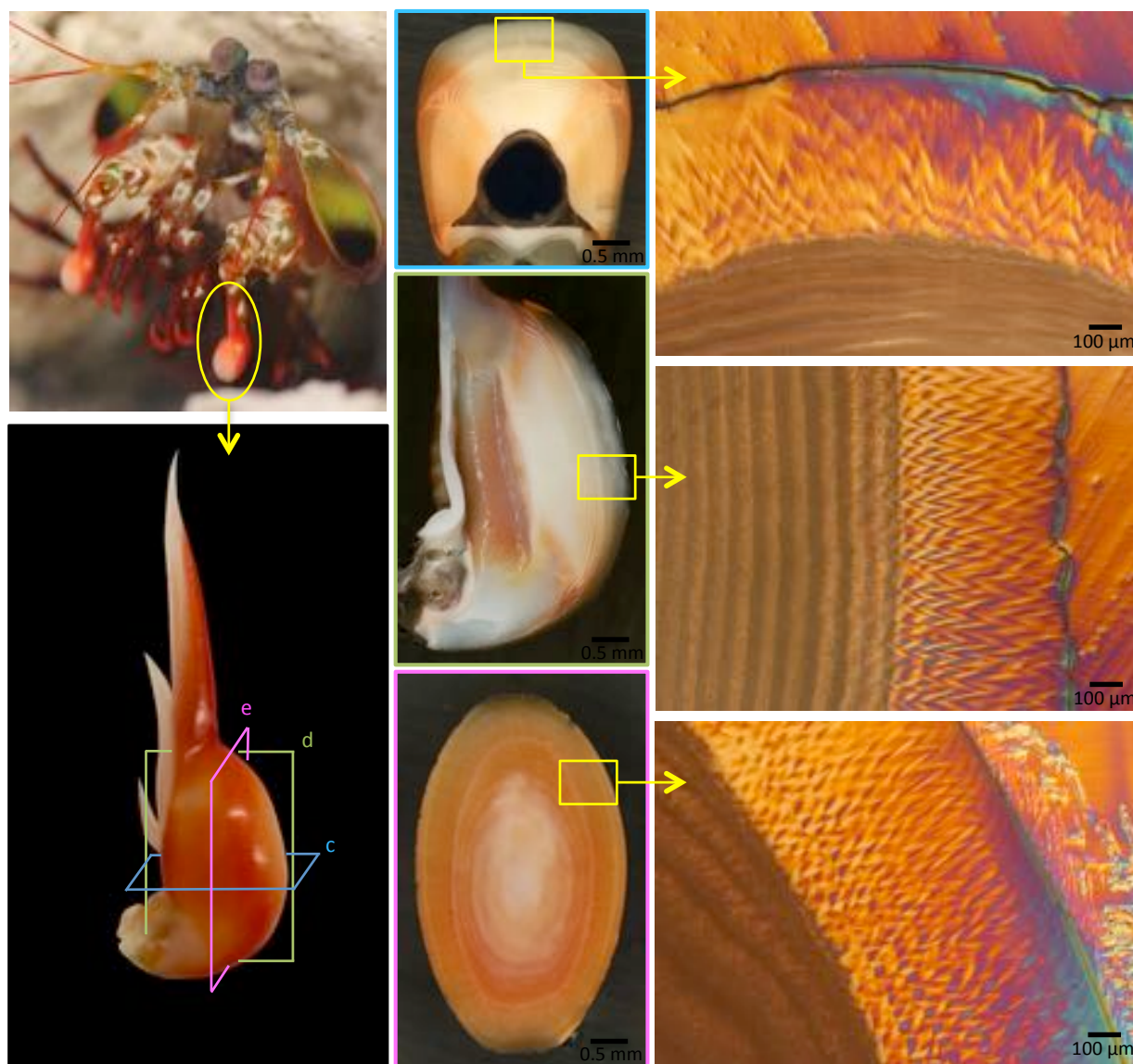


Figure 12. Upper left: Optical micrograph of stomatopod with dactyl circled in yellow. Lower left: Various sections made for imaging of dactyl club (blue: transverse, green: sagittal, pink: coronal). Upper middle and right: low and high magnification optical micrographs of transverse section; Center middle and right: low and high magnification optical micrographs of sagittal section; Lower middle and right: low and high magnification optical micrographs of coronal section).

We have taken the sagittal fractured sample and imaged using SEM (Figure 13). This micrograph clearly enables us to distinguish between the impact and periodic regions. A closer observation of the impact region does in fact reveal the helicoidal structure (Figure 14). Highlighted in Figure 15 are the herringbone-like structures we observe in this region. These structures appear to be a convoluted structure of the Bouligand, where in and out of plane fibers seem to be compressed in a sinusoidal like manner. Although details of how this structure has formed remain elusive, it seems that a potential mechanism is due to the differential in crystallization stresses between amorphous and crystalline calcium phosphate/carbonates.

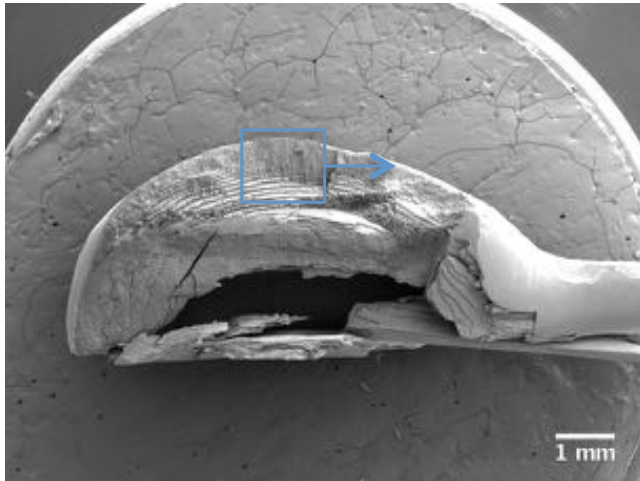


Figure 13. SEM micrograph of a sagittal fracture of the entire dactyl club.

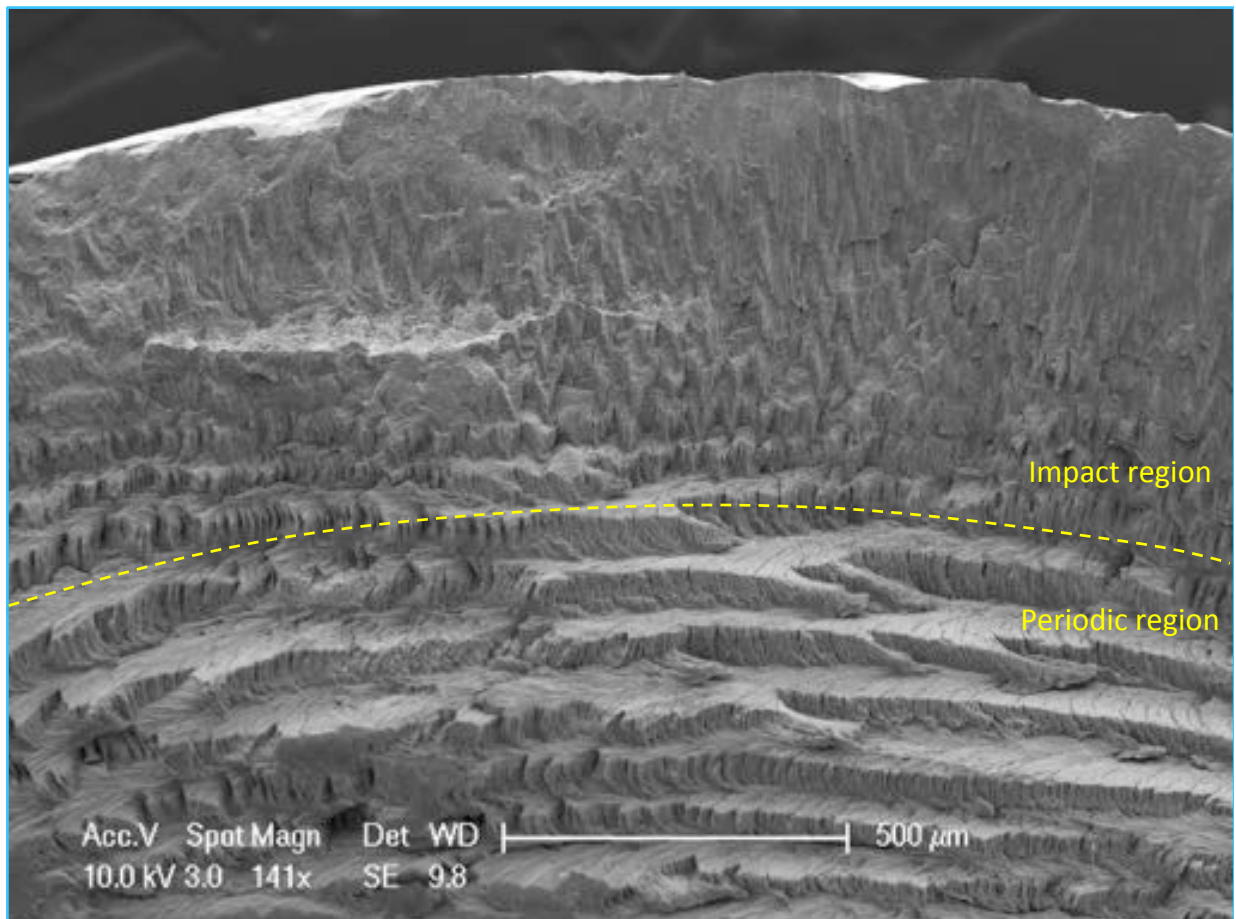


Figure 14. Higher magnification SEM micrograph of a sagittal fracture of the entire dactyl club. Impact and Periodic regions are differentiated with a yellow dotted line.

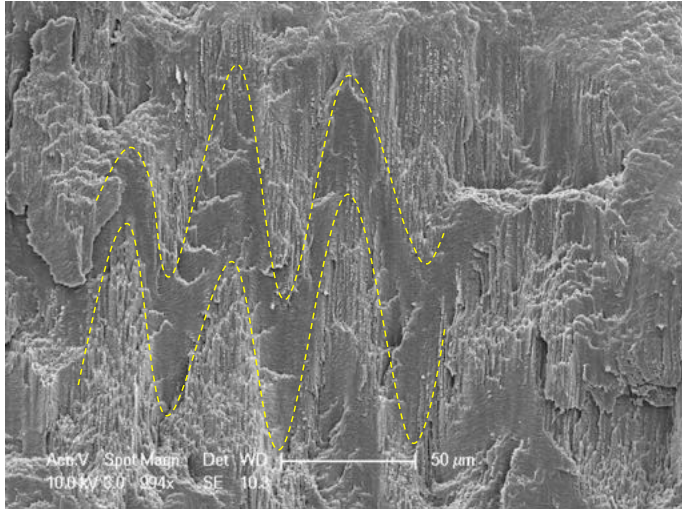


Figure 15. Herringbone structure highlighted with a yellow dotted line.

Evidence of this may be seen in the relative amplitude of the herringbone structure (Figure 16), which initiates slightly below the impact region, where the concentration of phosphorus and the onset of crystallization occurs.

Closer observation of the region in Figure 15 reveal that indeed, this is a Bouligand structure (Figure 17), and that fibers are rotating in a continuous manner within one period.

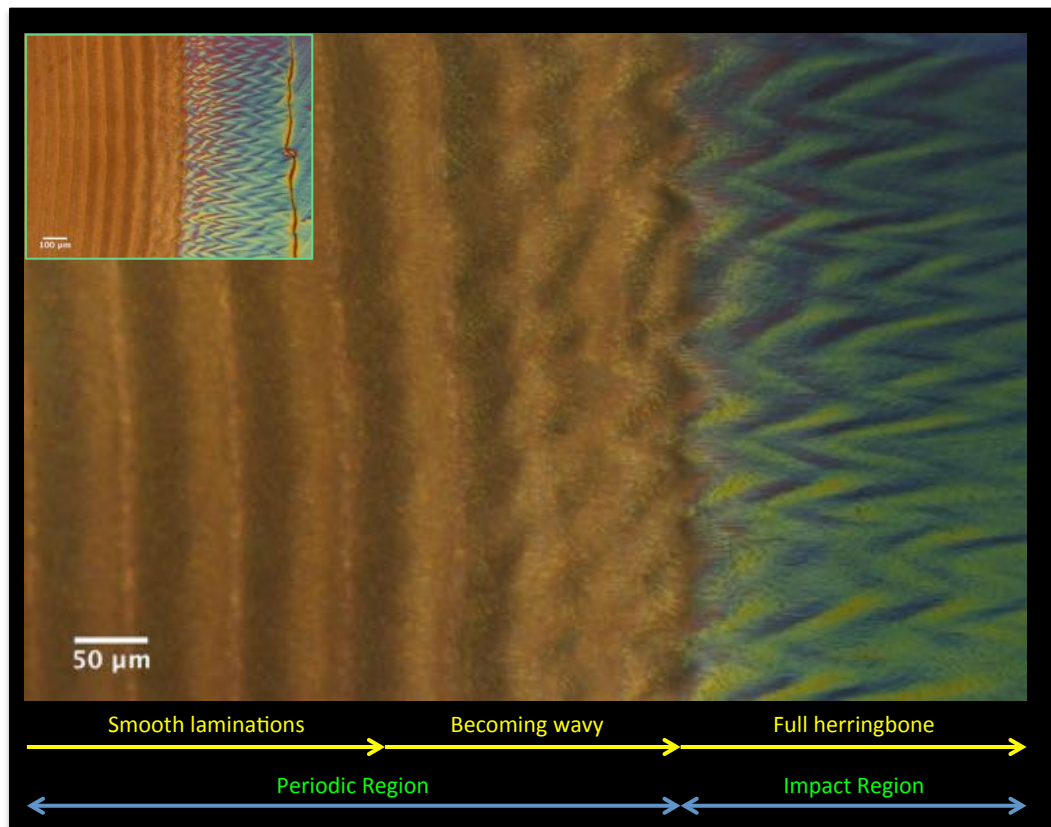


Figure 16. Optical micrograph of a graded transition towards a compacted (Herringbone) arrangement of fibers.

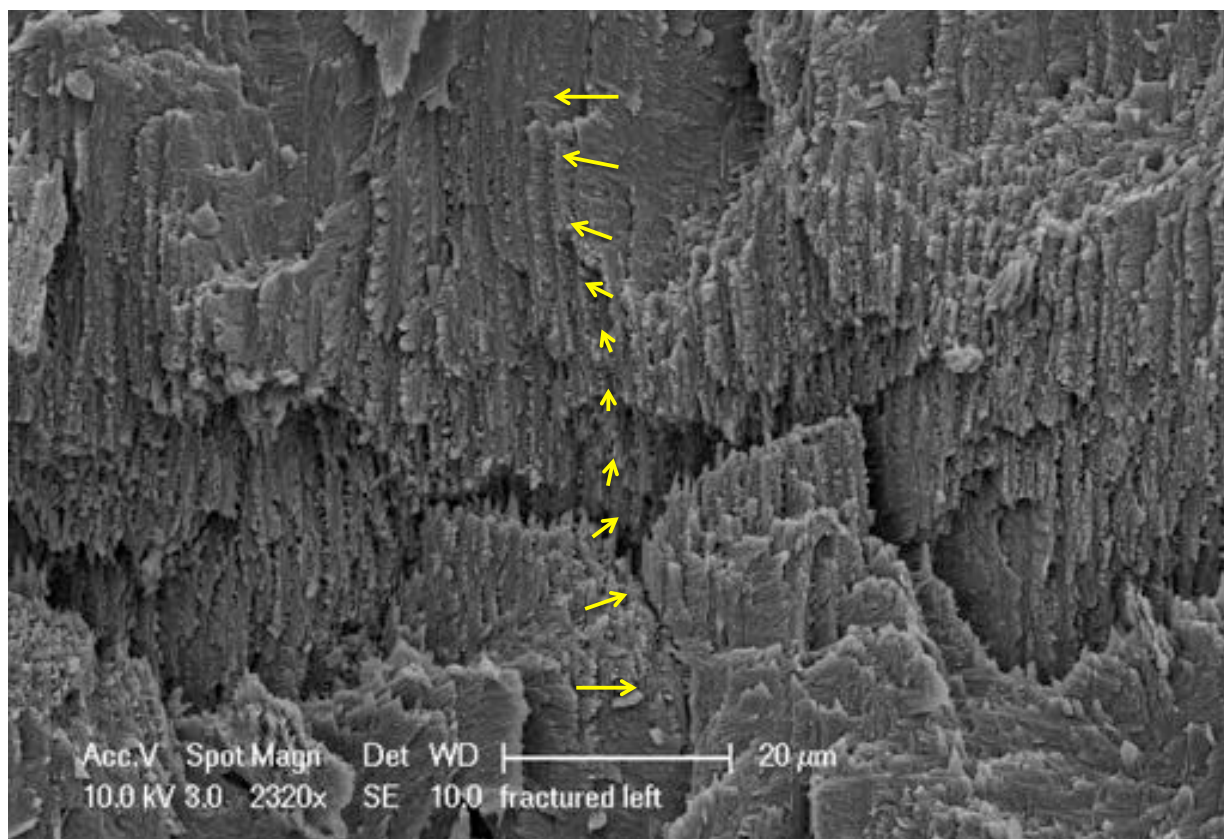


Figure 17. SEM micrograph showing the rotational alignment (yellow arrows) of fibers.

Here, the in-plane fibers show a rotation (Figure 18) and each fiber seems to consist of individual crystalline nanoparticles (Figure 19).

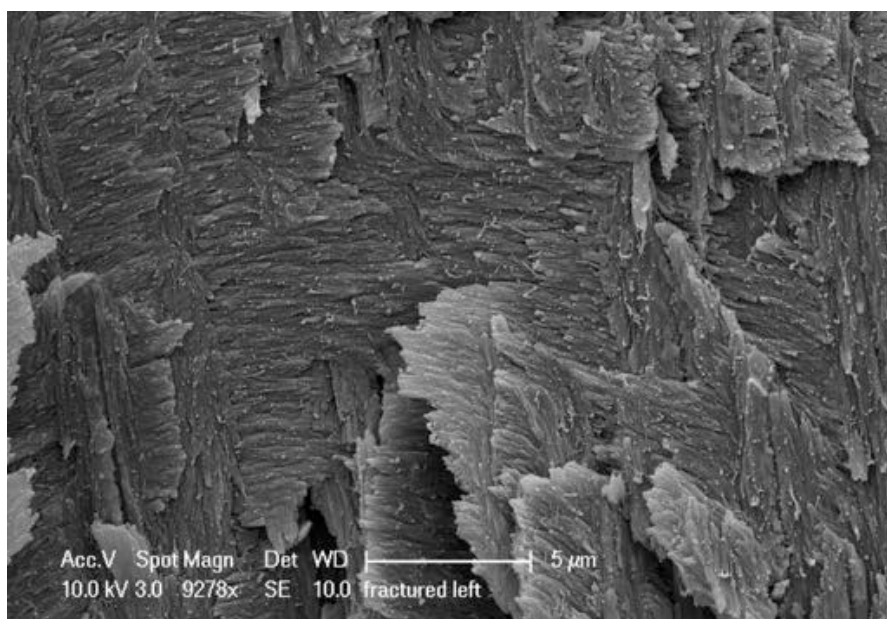


Figure 18. SEM micrograph showing in-plane alignment and rotation of fibers.

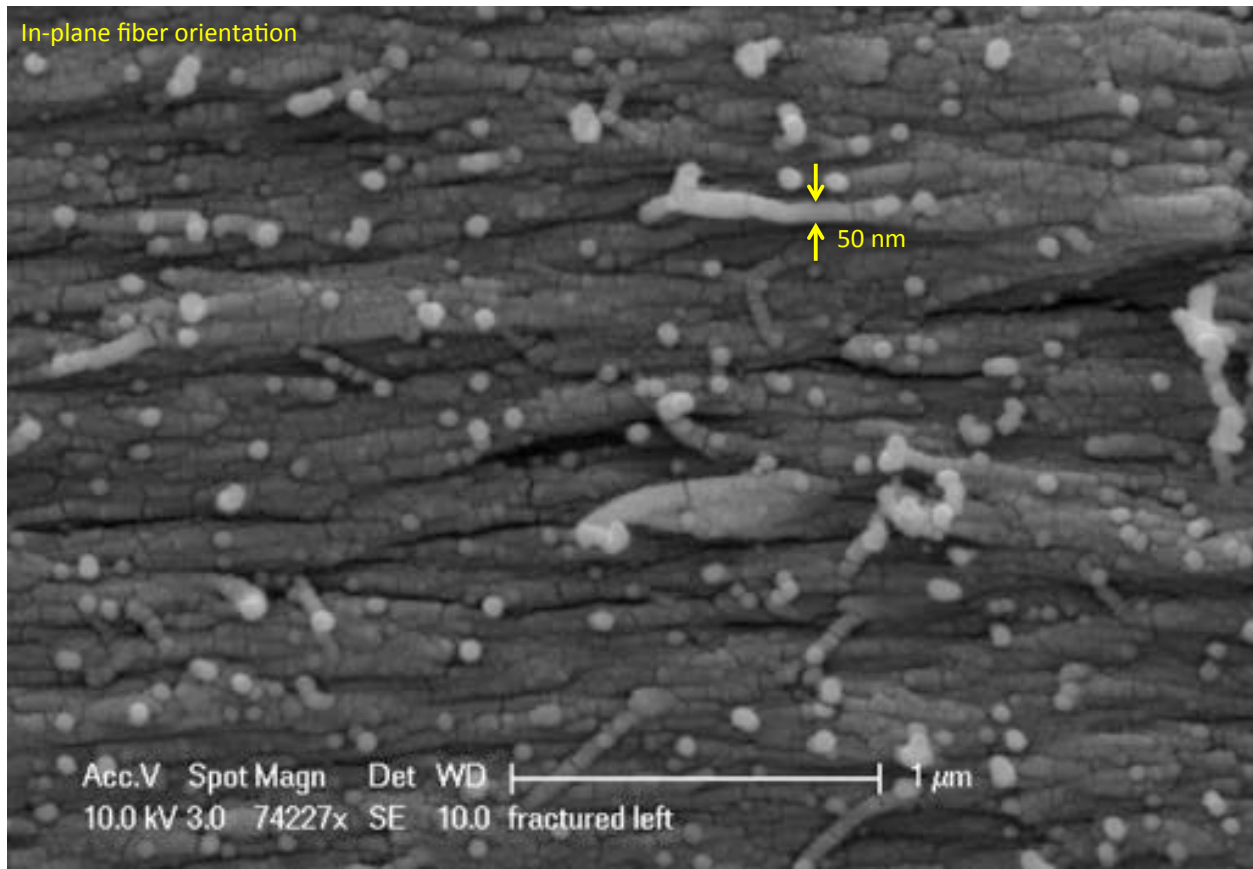


Figure 19. SEM micrograph of in-plane fibers; Highlighted are the individual constituent nanoparticles that are contained within each fiber.

In the final period of this project, we continued the investigation of the herringbone structure within the impact region as well as observed some additional features of the impact region of the dactyl club. TEM observations of the herringbone structure confirmed the rotational alignment of in and out of plane fibers (Figure 20). What is clear here is that based on dark field analysis of the in-plane and out of plane regions within the herringbone structure, (002) HAP planes are present within the in-plane fibers and therefore rotate 90° when in the region adjacent to them.

In fact, when we image this region more closely, the particulate nature of these fibers highlights the rotation between the sheets of fibers (Figure 21).

We performed a demineralization time series to observe any boundaries between inorganic and potentially templating organic phase that would reveal toughening pathways. 4 pieces of transverse sectioned dactyl clubs (2 entire clubs cut in half from one stomatopod) were immersed in a dilute solution of acetic acid for up to 1 hour. During that time, each of the 4 specimens was removed from the etching bath at 1, 5 and 60 minutes, as well as one that was not etched, rinsed with DI water and imaged by SEM (Figure 22). Unetched specimens showed a pore network within impact region. Pore diameters were approximately 500nm in size and spaced 2-3 μm apart. After 1 minute of etching in acetic acid, these pore networks were exposed and a segmented inorganic structure surrounded by organic was left behind. At 5 minutes in acetic acid, more

inorganic was removed and the organic rods were drawn together likely due to capillary stresses. Finally, after 60 minutes in acetic acid most of the inorganic was removed, revealing the underlying organic scaffold as fibrous sheets.

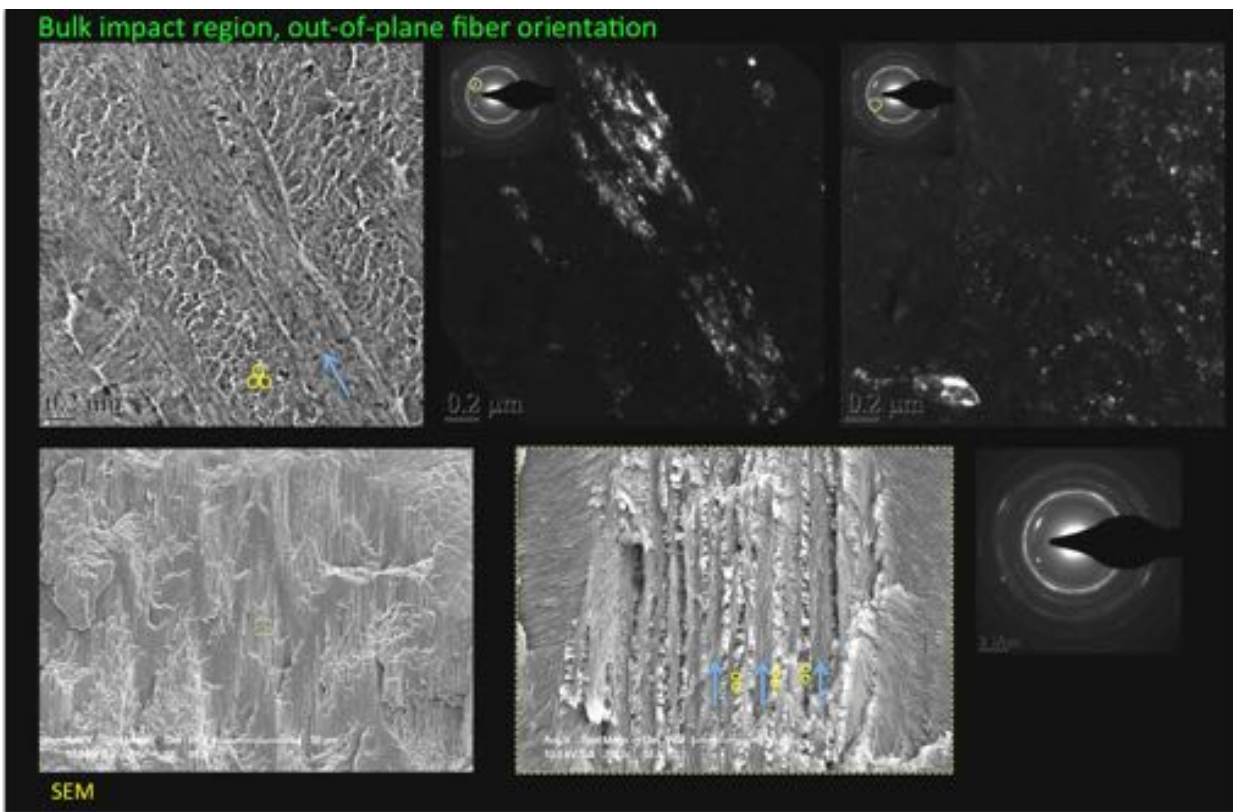


Figure 20. SEM/TEM analyses of herringbone structure. Upper left: Bright field TEM micrograph of in-plane and out of plane fibers (from region highlighted in green box of lower left as well as lower middle SEM micrographs); Dark field TEM micrographs (upper middle and upper right) represent regions where the (002) spot in the selected area electron diffraction pattern (green circle in both SAEDs) is selected and imaged, revealing the (002) HAP planes from the in-plane fibers and the upper middle is from a non (002) selected region, confirming the absence of other planes within the “in-plane” region.

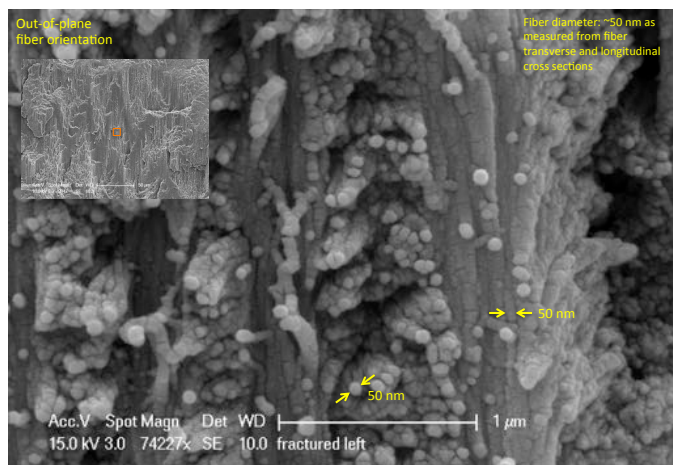


Figure 21. SEM micrograph of rotated interface within herringbone structure. Fiber sheets are clearly consisting of ca. 50 nm particles.

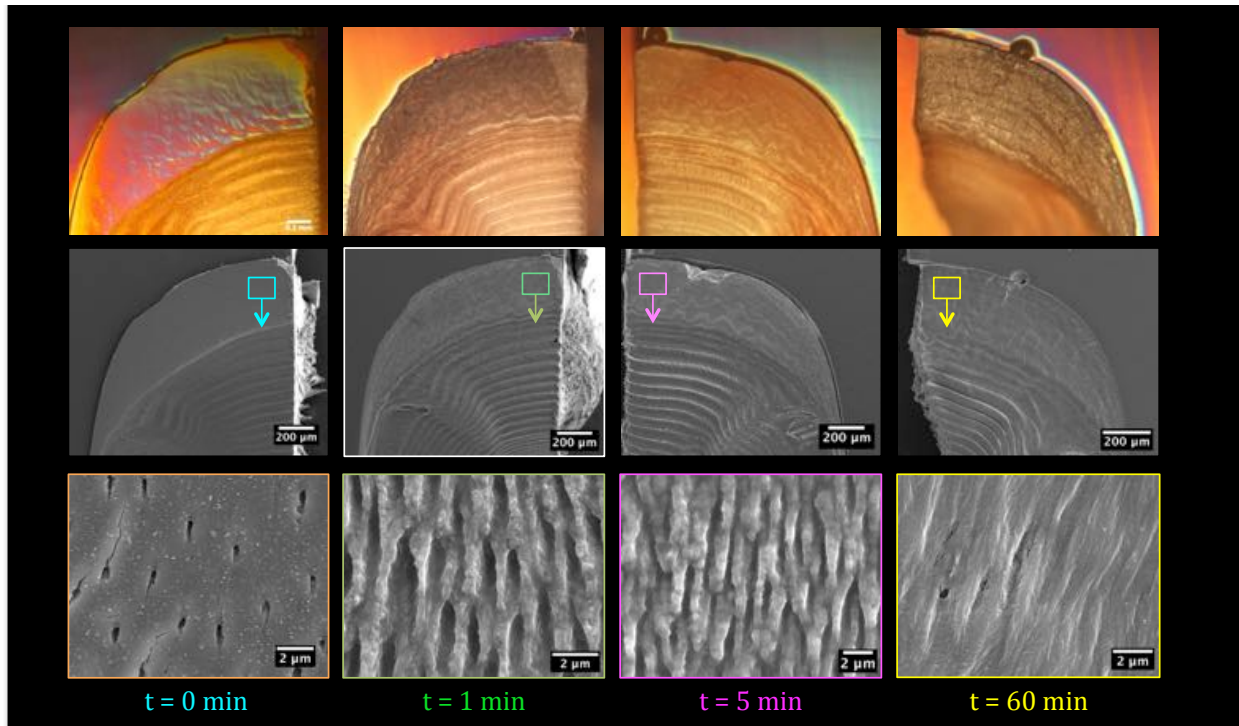


Figure 22. Demineralization time series of dactyl club. 1st (left) column: Intact transverse section of dactyl club (not etched) under polarized light (upper), SEM mode (middle and lower) showing pore network within impact region. 2nd column: Transverse section of dactyl club etched at 1 minute in acetic acid and imaged under polarized light (upper), SEM mode (middle and lower) showing exposed pore networks from receding and *segmented* inorganic crystal. 3rd column: Transverse section of dactyl club etched at 5 minutes in acetic acid and imaged under polarized light (upper), SEM mode (middle and lower) showing exposed pore networks from receding inorganic crystal. 4th column: Transverse section of dactyl club etched at 60 minutes in acetic acid and imaged under polarized light (upper), SEM mode (middle and lower) revealing underlying organic scaffold.

In order to elucidate this segmented structure observed during the demineralization reactions, a section of the herringbone structure was excised using a focused ion beam (FIB) process and imaged in TEM. Bright field TEM highlights the rod-like structure (Figure 23) and shows that each rod consists of ~ 35 nm particles which are stacked on each other. This suggests that the crystallization process involves an infiltration process of amorphous precursor, which subsequently crystallizes in the presence of organic scaffold which is modified with peptides that control the local supersaturation and orientation of HAP. Selected area electron diffraction shows that the (002) planes of HAP are perpendicular to the fiber axis while the (100) planes are parallel to fiber long axis.

Synchrotron analysis (Figures 24, 25) of the sagittal section within this impact region confirmed the presence of highly oriented HAP. Analyses of these scans supported the TEM evidence that (002) planes were perpendicular to the long axis of fibers with (100) planes parallel to them. Interestingly, the initial synchrotron scans through the surface of the club (Figure 25) showed an isotropic region, where HAP is randomly oriented. Subsequently, we investigated this “impact surface”.

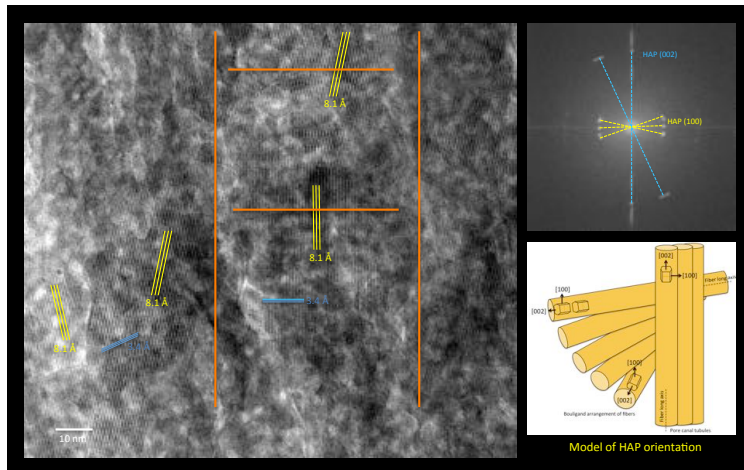


Figure 23. Left: Bright field TEM analysis of oriented rods, highlighting the columnar structure composed of individual nanoparticles. Lattice imaging shows (002) planes perpendicular to the rod's long axis whereas (100) planes are parallel to this axis. Upper, right: Electron diffraction confirming the crystallographic orientation of the rods. Lower, right: schematic showing a potential model of this structure.

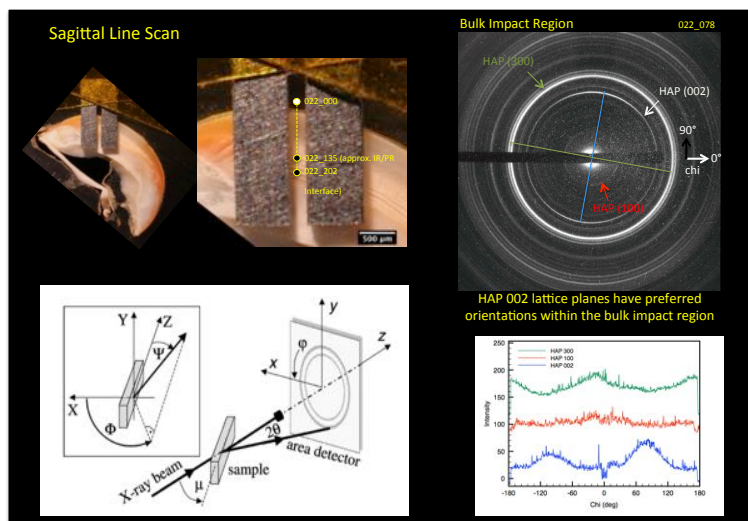


Figure 24. Synchrotron analysis of sagittal section of impact region. Upper, left: Orientation of specimen with slits defining region of interest. Scan was taken from beyond the club surface through the impact region into the periodic region. Lower, left: Schematic of experiment. Upper, right: Diffraction frame from synchrotron, highlighting the preferred orientation of (002) HAP in the impact region. Lower, right: Chi scan showing the in-plane orientation of the same (002) HAP peaks.

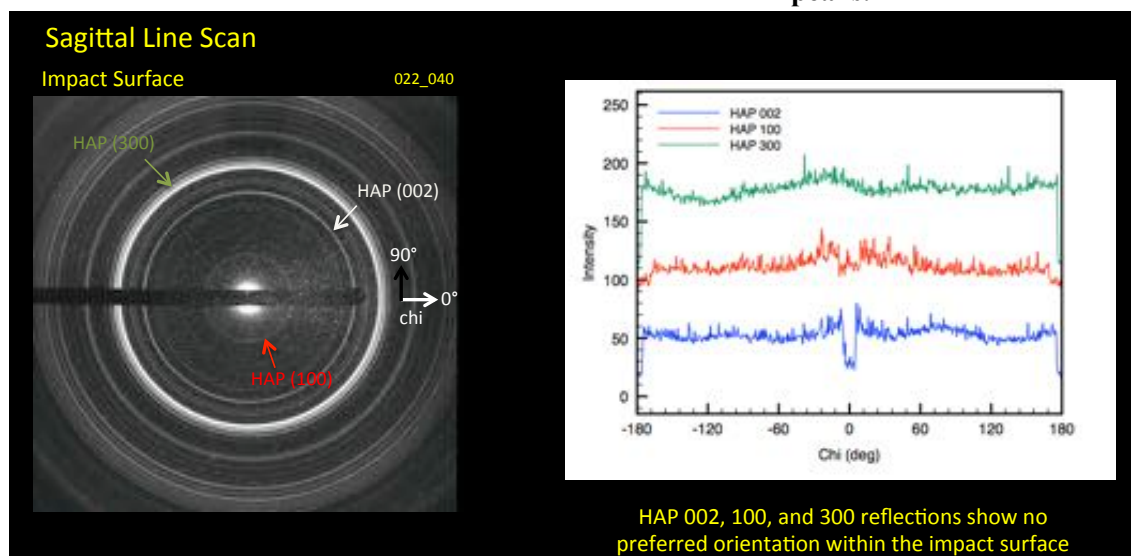


Figure 25. Synchrotron analysis of sagittal section of impact surface confirming random orientation of HAP.

Additional observations by scanning electron microscopy revealed this impact surface and its morphological features (Figure 26).

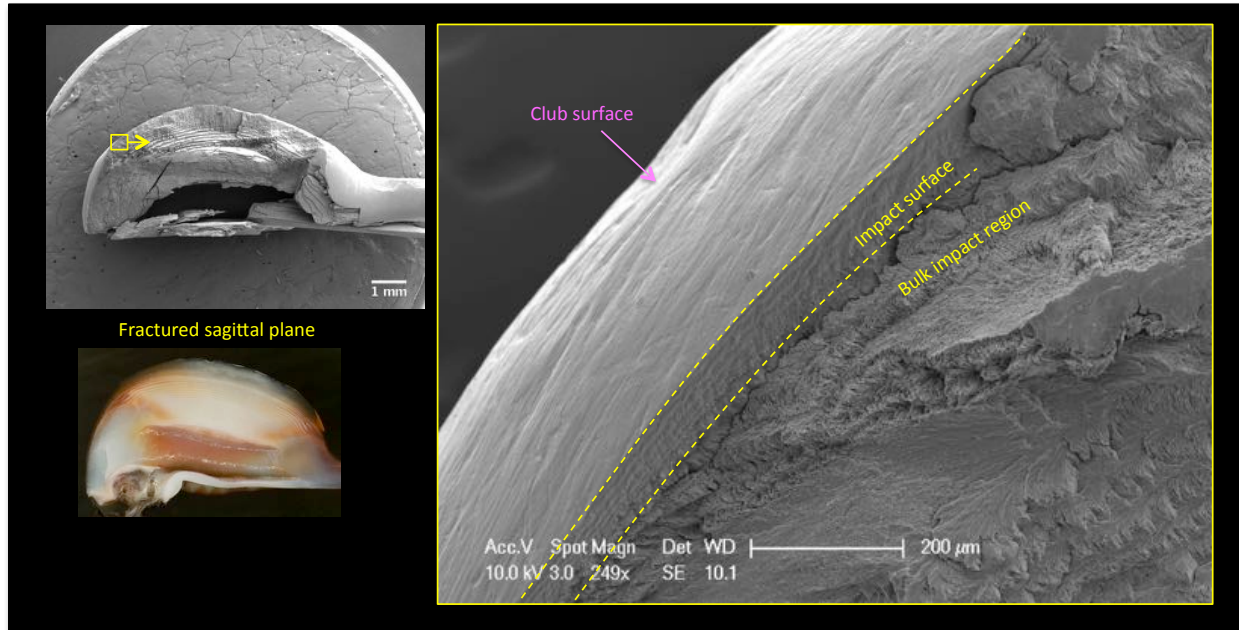


Figure 26. SEM observation of sagittal section of impact surface.

The surface covers most of the surface of the club, although the apex of the club, where most of the impact would occur, was partially worn. This specific club was a few months old and we speculate that the impact surface plays multiple roles in the club (redistributing stress upon impact and serving to indicating a new molting cycle). The pore canals observed in the impact region continue into this impact surface, but taper as they reach the surface of the club. These canals likely transport mineral and indicate a completion of the crystallization process.

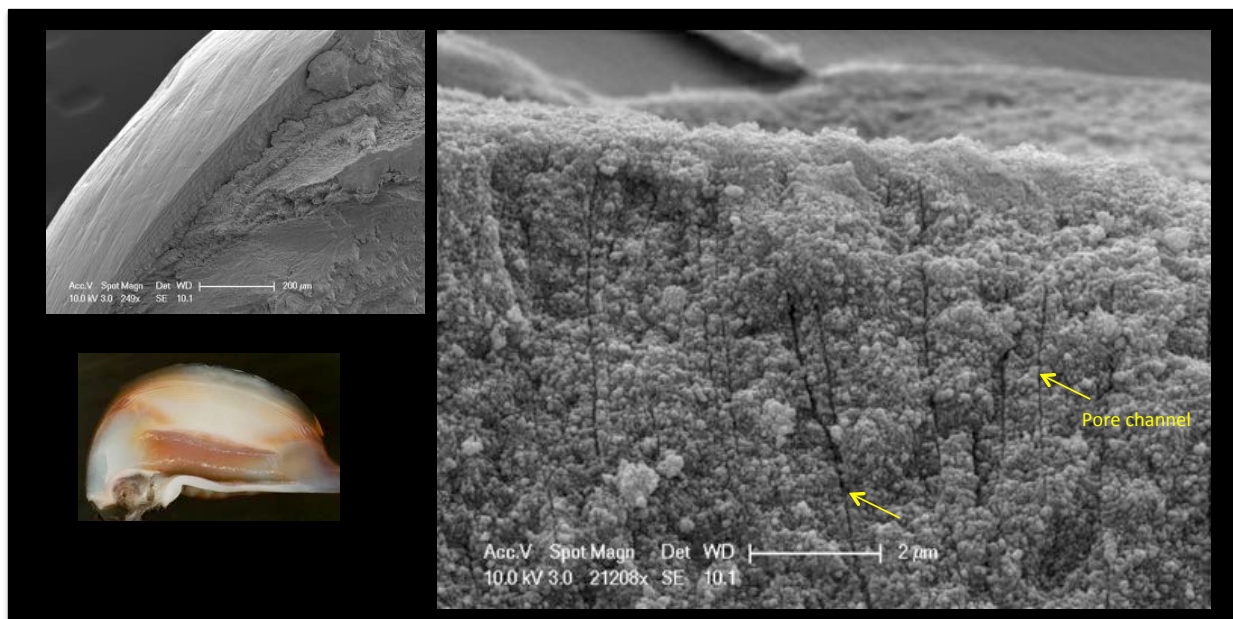


Figure 27. SEM observation of sagittal section of impact surface highlighting pore canals.

TEM analysis of the impact surface and impact region (Figure 28) confirmed the random nature of the grains within the impact surface. Bright field and dark field imaging (Figure 29) highlighted their isotropic nature.

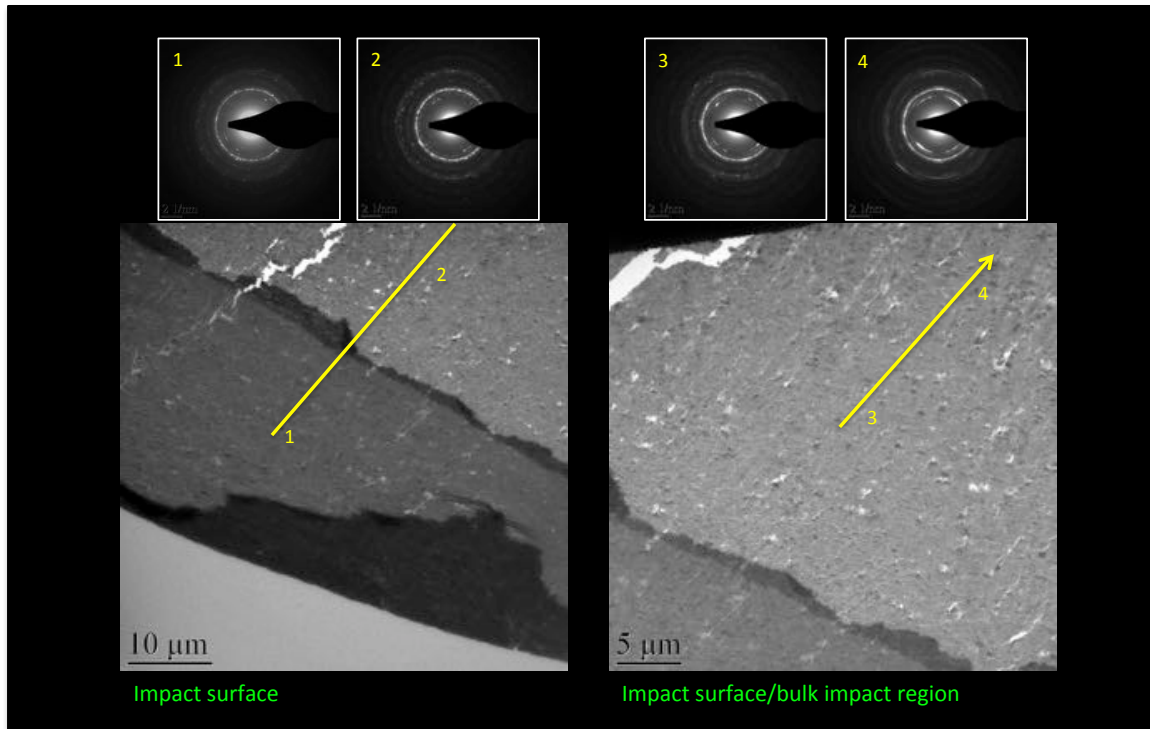


Figure 28. TEM observation of impact surface (left) and impact region (right) with SAED for each labeled points revealing random orientation within the impact surface and orientation in the impact region.

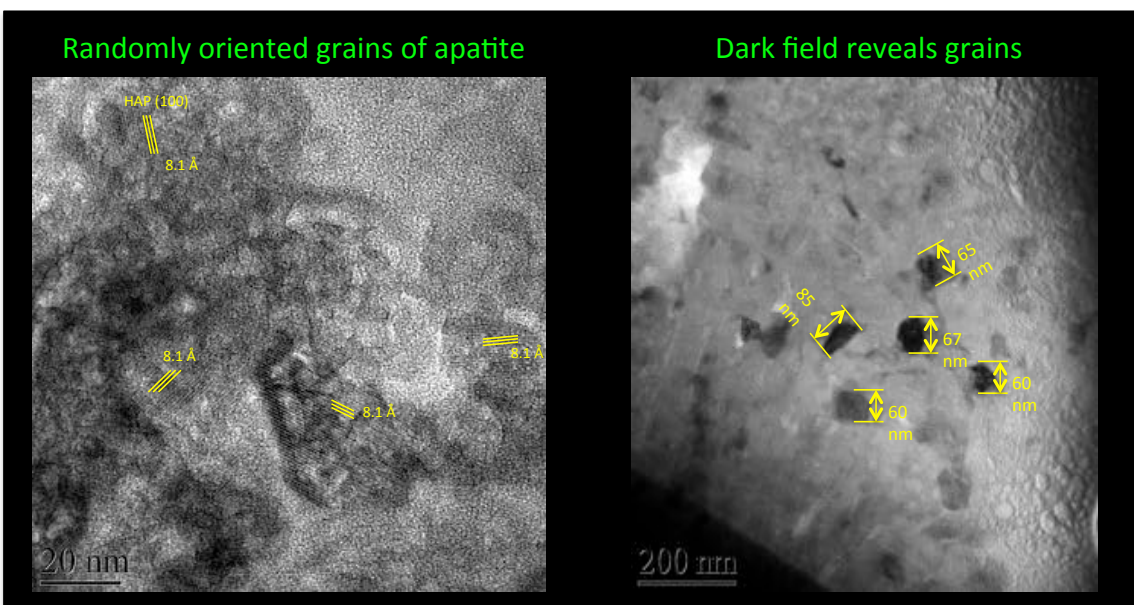


Figure 29. Bright field (left) and dark field (right) TEM observations of impact surface.

The dark field images show that the grains within the impact surface are significantly larger than in the impact region. This is likely due to the lack of organic scaffolding, which would lower the activation barrier to nucleation. Thus, crystals are larger from homogeneous nucleation. In addition, the grains do not form a crystallographic percolation network. Thus, upon impact, particles in this region are free to flow and provide toughening.

Elemental analyses:

Using a dual energy dispersive detection system (EDS), in collaboration with the University of Western Sydney (UWS), a transverse section of the club was mapped (Figure 30). Based on comparison of elemental concentration maps, specific nodes appear which provide information about region-specific variation in phase.

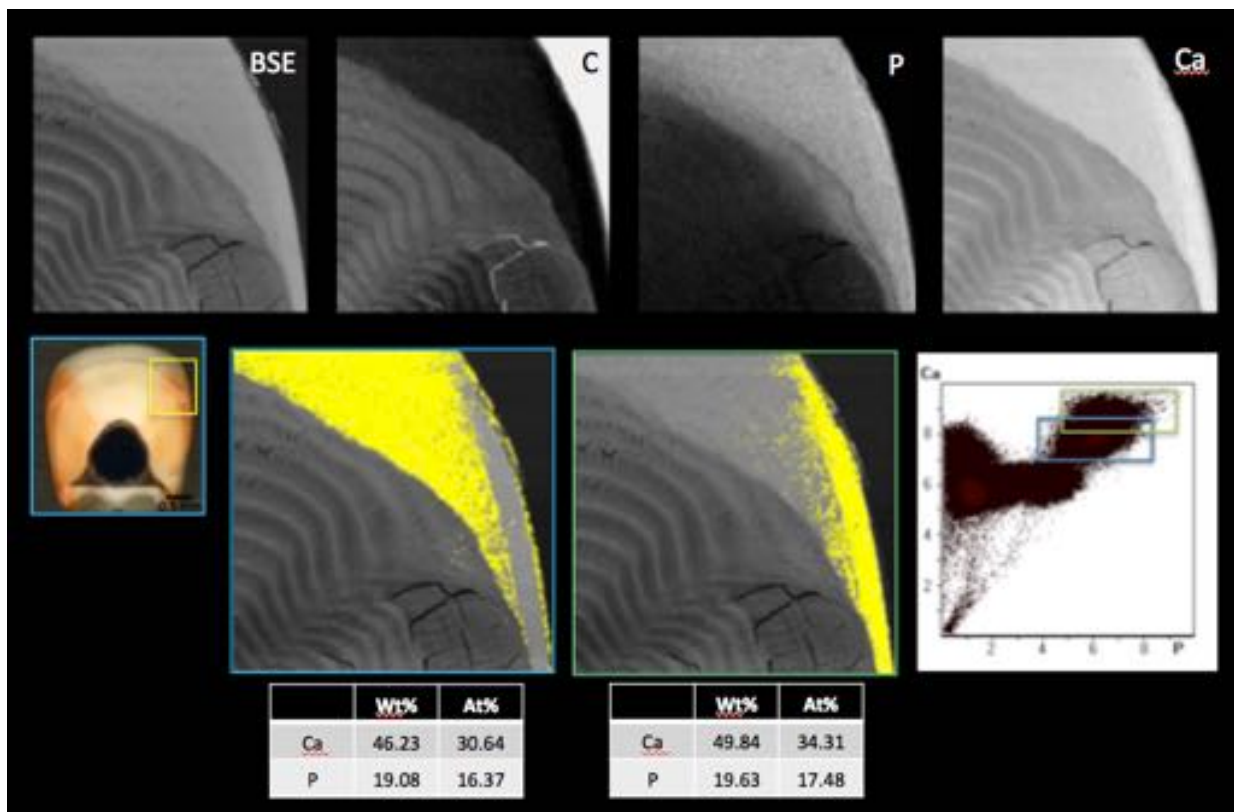


Figure 30. Elemental analysis of impact region and surface of club. With specific nodes highlighted (blue and green boxes on lower right Ca,P map), specific compositional differences can be observed between the impact region and surface.

Based on this analysis, it appears that the impact surface has a higher ratio of calcium to phosphorus (1.96 vs. 1.87), which will likely affect the hardness of this region.

Using the same EDS mapping strategy, but acquiring for 24 hours, a detailed map of the impact region/periodic region interface was attained (Figure 31). Here, it is clear that the change in Ca/P ratio as well as the presence of magnesium significantly controlled the crystallinity and formed a gradient that reduced interfacial stresses between impact and periodic regions.

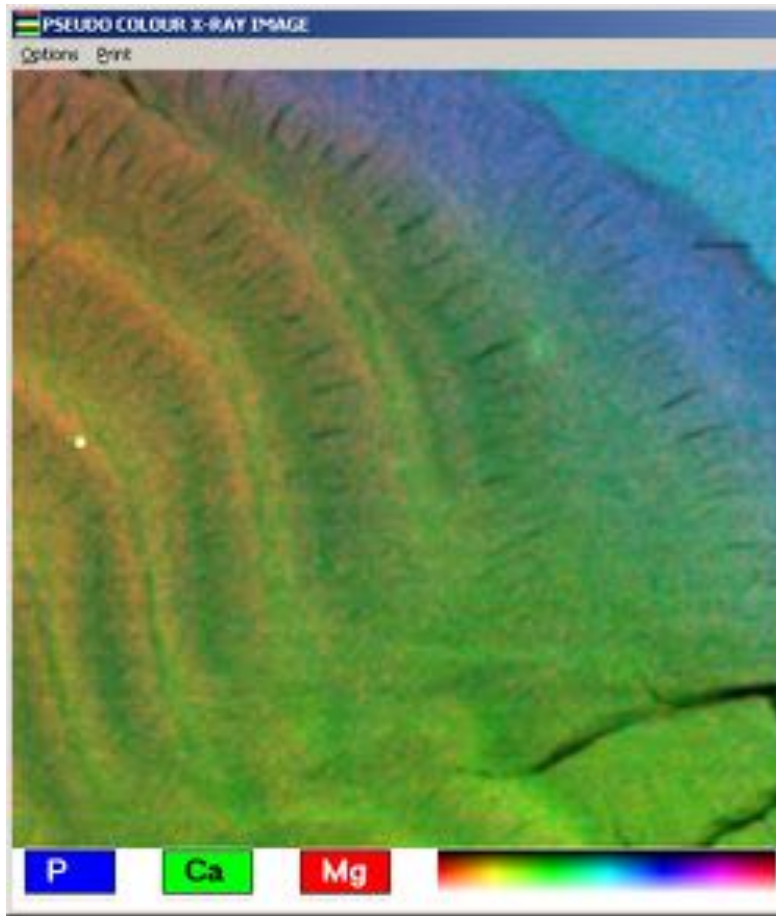


Figure 31. Elemental analysis of impact (blue) and periodic (green/red) regions of the club by acquiring spectra for 24 hours. The presence of Mg is clearly seen in the periodic region and likely stabilizes the amorphous phase.

Periodic region:

In year 1, we analyzed polished cross-sections of the dactyl club using scanning electron microscopy. We found cracks which showed some preferred orientation (Figure 32).

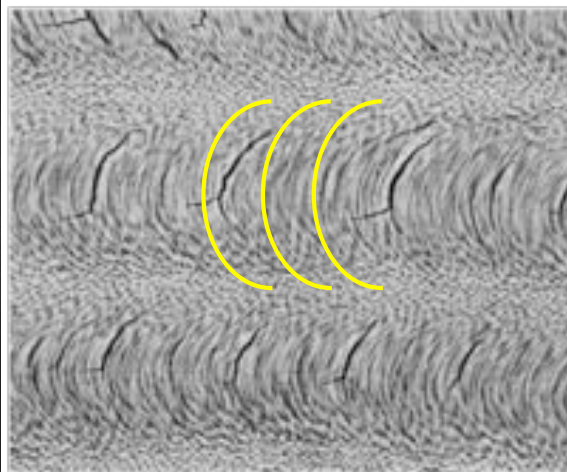
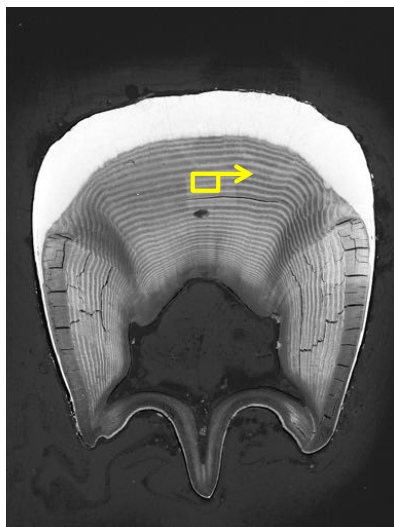


Figure 32. BS-SEM analysis of a polished cross section of the dactyl revealed curved fractures within the periodic region.

Further probing of these cracks was conducted by fracturing the dactyl club. A cross-sectional

fracture revealed the helicoidal nature of this region (Figure 33) and provides insight into potential toughening mechanisms within the dactyl club.

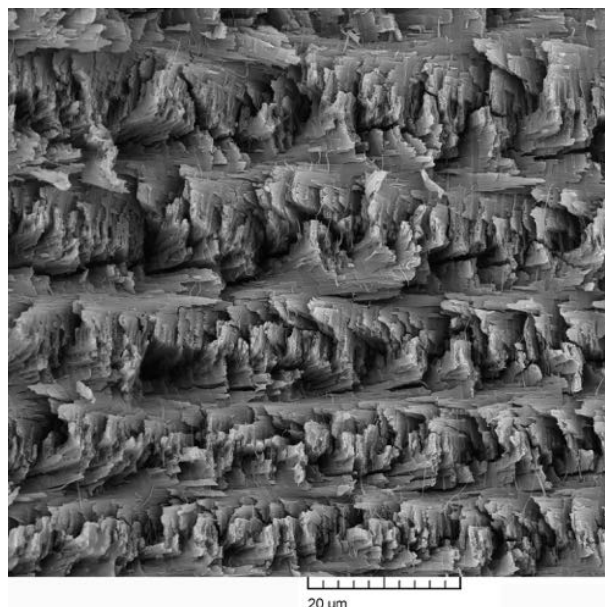


Figure 33. BS-SEM analysis of a polished cross section of the dactyl revealed curved fractures within the periodic region.

Analysis of this region using synchrotron x-ray (Figure 7) showed that this region consists of amorphous calcium carbonate/phosphate with alpha-chitin fibers. This amorphous mineral is likely stabilized by the presence of magnesium (Figure 6). In fact, additional EDS line scans from the impact region into the periodic region (Figure 34) confirms the presence of magnesium as critical in helping to stabilize amorphous mineral. In addition to the presence of magnesium, there is a decrease in phosphorus and calcium concentrations from the impact surface to the interior of the dactyl club and a

concomitant increase in carbon and magnesium throughout the same region. While there is an abrupt step-like decrease in calcium concentration through the transition from the impact region to the periodic region, the phosphorous concentration decreases in a gradient-like fashion. These results indicate a biphasic mineral system, with the impact region dominated by calcium phosphate and the remainder of the club likely consisting of a mixture of calcium phosphate and calcium carbonate.

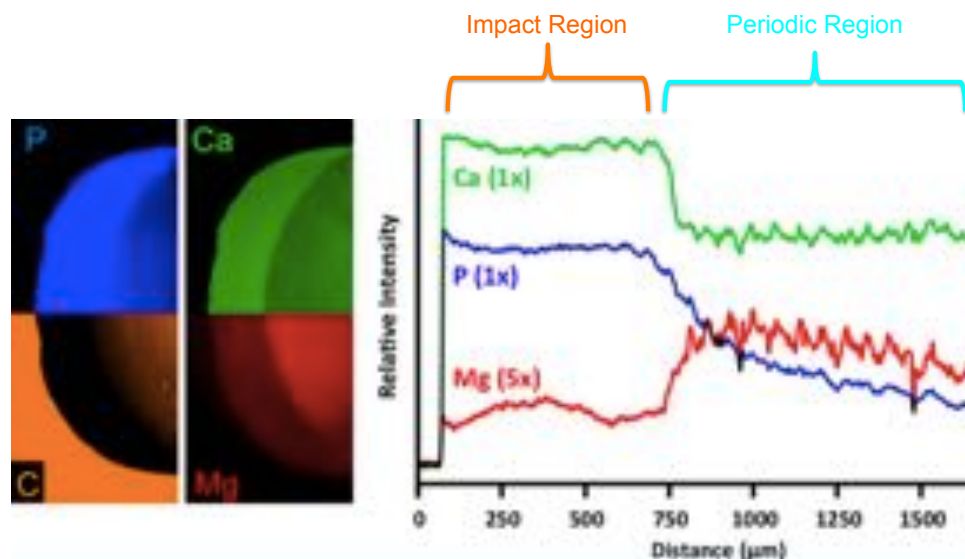


Figure 34. EDS measurements tracking regio-specific elemental distributions of phosphorus and calcium as well as carbon and magnesium throughout the same region.

The sinusoidal-like fluctuations in Mg and Ca concentrations within the periodic regions are likely due to the rotation of mineralized fibers. Since the volumetric element of the EDS is limited, in-plane fiber orientations are likely to reduce mineral interactions with the electron beam and therefore provide the sinusoidal nature to the EDS line scans observed.

In order to determine the rotational angle of these mineralized fibers, synchrotron analysis of the highly expanded periodic region of the stomatopod dactyl club was performed. Texture analysis of the helicoidal ultrastructure using a microdiffraction beam line with a spot size of 5 mm x 5 mm was performed where the white line is shown (Figure 35). Using the d-spacing of the (110) peaks of α -chitin (Figure 36), we confirmed this periodic structure with one superlayer measuring $\sim 75\mu\text{m}$ in this region. By defining each layer as having a thickness of 1 μm , the angle of rotation throughout the periodic region was calculated to range from 1.6° in the outermost region to 6.2° in the inner region of the club.

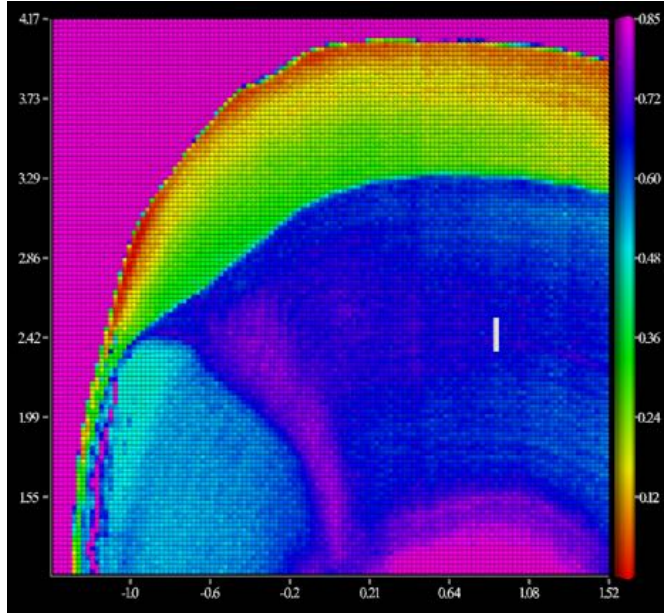


Figure 35. Texture analysis of the helicoidal ultrastructure using a microdiffraction beam line with a spot size of 5 mm x 5 mm (performed at the white line).

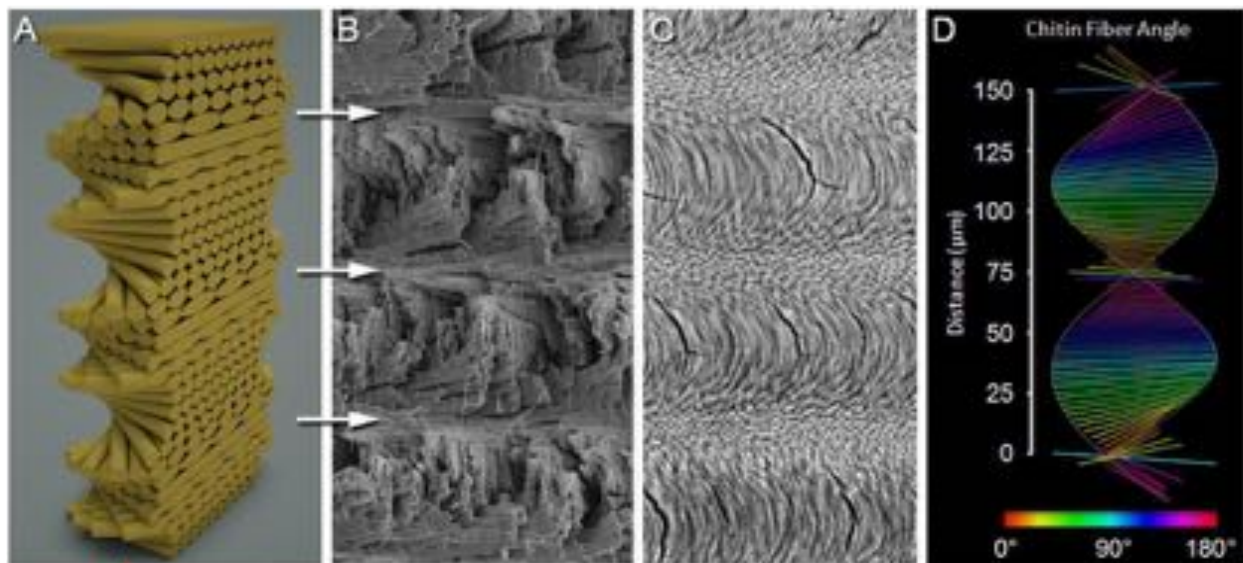


Figure 36. Texture analysis of the helicoidal ultrastructure using a microdiffraction beam line with a spot size of 5 mm by 5 mm using the d-spacing of the (110) peaks of α -chitin. (a) schematic of helicoid; (b) micrograph of fractured region of helicoid; (c) polished region of helicoid with nested arc cracks; (d) plot of rotational angle of chitin fibers.

The sheets of locally parallel chitin fibrils are stacked upon each other such that each sheet is skewed by an angle from the sheet below it. This constant difference in angle between neighboring sheets ultimately produces a rotation of 180° , defining a characteristic wavelength and a superlayer. SEM observations of a fractured coronal section of the club in the periodic region (Figure 37) reveals a spiral of fractures (highlighted with false coloring).

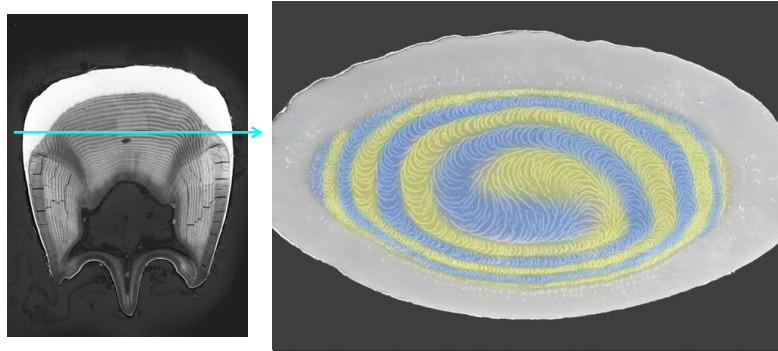


Figure 37. SEM observations of a fractured coronal section of the club in the periodic region reveals a spiral of fractures (highlighted with false coloring).

Using a graphics program, rows of chitin fiber bundles in a helicoidal stack were visualized as close-packed cylinders. Each cylinder was colored half yellow and half blue to better visualize the constant rotational offset between each sequential layer. Curvature was then applied to the entire stack to represent the influence of the hemispherical dactyl club core and exterior. Finally, a plane was chosen to represent a polished cross section through the curved structure, and the points which defined each cylinder were collected from the intersecting plane, and visualized with their colors preserved (Figure 38). The resulting visualization of the fibers precisely reproduces the fractures seen in the charge contrast scanning electron micrographs, providing strong evidence that fractures predominantly propagate between the chitin fibers within the helicoidal assembly.

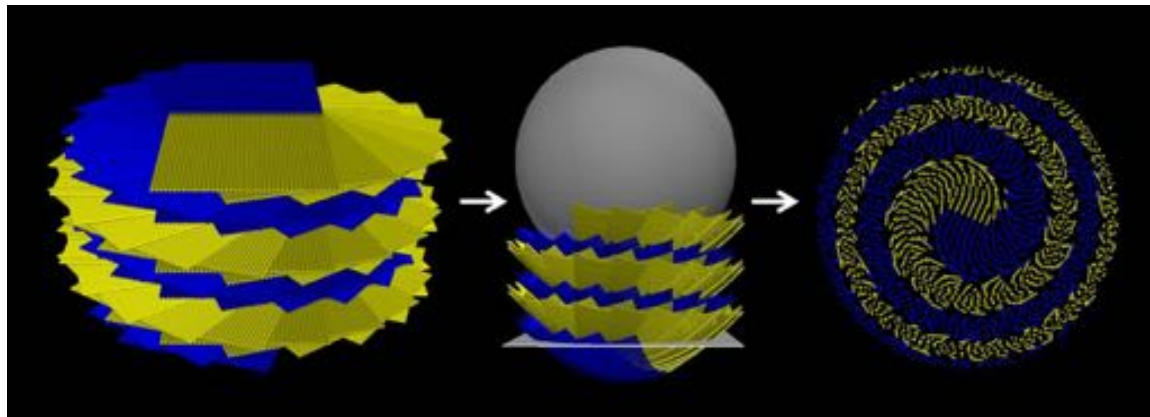


Figure 38: A helicoidal stack of cylinders representing chitin fiber bundles within the dactyl club (left). The same helicoidal stack with an applied curvature was achieved by wrapping the structure around a sphere and an intersecting plane (shown in gray) denotes the location of sectioning (middle). A collection of points representing the chitin fiber bundle locations accurately reproduces both the locations and curvature of the fractures seen in charge contrast scanning electron micrographs.

In fact, we found that this structure indeed does toughen the club by redirecting cracks. Post-damaged clubs proved this. We separated a dactyl from a stomatopod that had been impacted for more than 2 months. Based on feeding habits, we estimated that it had been impacted thousands of times. After separating the club, we sectioned it and placed it under a SEM and allowed the beam to sit on the sample for more than 5 minutes. This enabled the sample to charge (specifically, we called this charge contrast imaging). By doing this, surface features were highlighted due to build up of charge. Thus, this process enabled us to visualize local damage within the club. Figure 39 highlights the periodic region of the club, riddled with nanocracks. However, none of these cracks from within the dactyl were able to propagate through the entire structure, underscoring the importance of this region to absorb energy and redirect cracks.

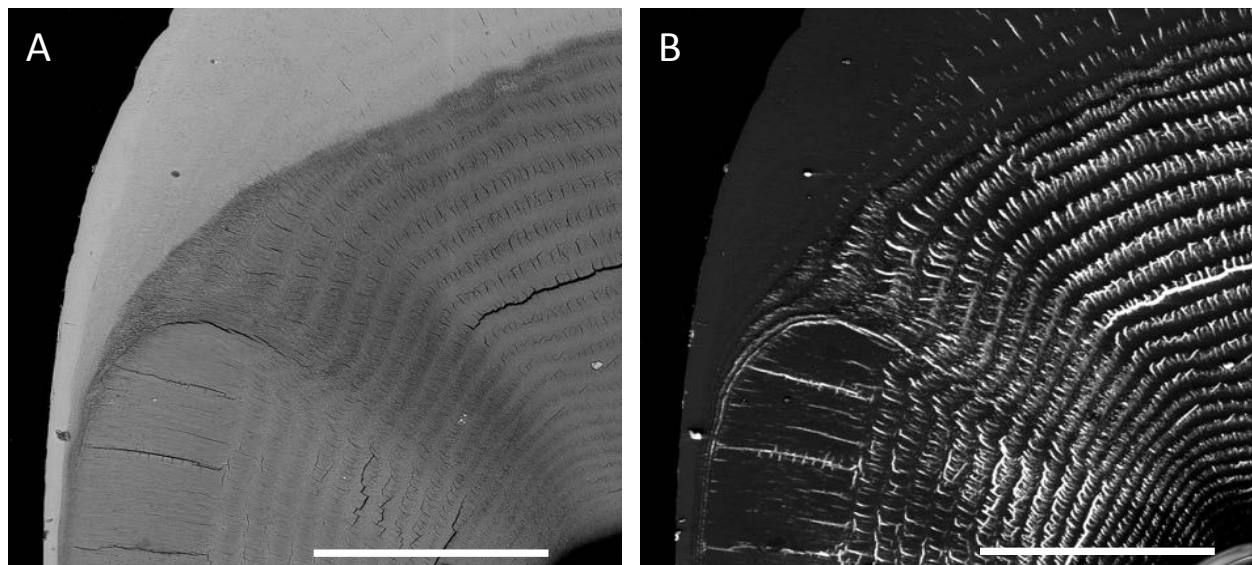


Figure 39: A cross-sectional micrograph of the dactyl club after 2 months of use by the stomatopod. (A) Back scatter SEM. (B) Charge contrast image of the club, showing multiple nanofractures within the periodic region. Scale bar is 500 microns.

In years 2 and 3, we focused ultrastructural investigations on other regions in the club (impact and striated). From the periodic region perspective, we focused on modeling and biomimicry in the later part of the project and this will be described later in this report.

Striated region:

Based on preliminary data, it was known that the striated region consisted of fibrous sheets that were wrapped circumferentially around the club. However, additional analysis was needed.

In year 1, we initially performed ultrastructural analyses using optical and SEM analysis. Dactyl clubs were sectioned across a transverse plane (Figure 40) and subsequently polished to yield a flat and smooth surface. Back scattered SEM revealed that the striated region had similar mineral content to the periodic region. Optical microscopy shows that the striated region, which contains parallel sheets of fibers oriented perpendicular to the transverse section, was approximately 300

microns thick. Initial EDS maps reveal significant amounts of phosphorus, while phase mode AFM revealed the softer organic between mineralized sheets.

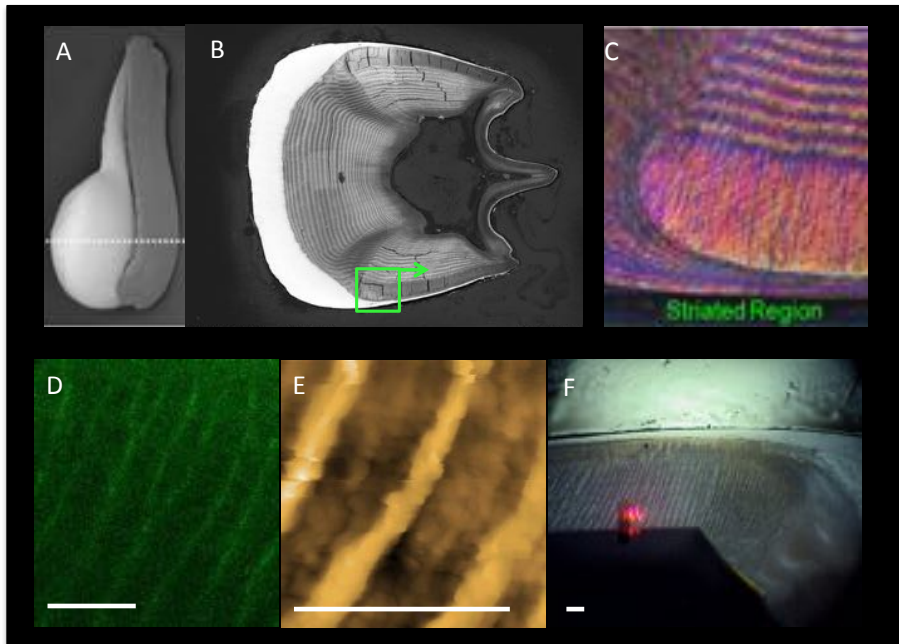


Figure 40. Analysis of striated region. (A) region of club that was sectioned. (B) BSSEM of transverse section. (C) Polarized optical micrograph of striated region. (D) EDS map of Phosphorus (green). (E) AFM Phase map showing softer regions in yellow. (F) Red dot is locator for AFM in (E).

Subsequently, the transverse section was placed in a demineralizing bath (5

vol% acetic acid + 2.5% glutaraldehyde) to reveal the organic substructure (Figure 41). It became evident that the region indeed consisted of structural organic fibers (alpha-chitin) that were assembled perpendicular to the transverse section and were encased in mineral.

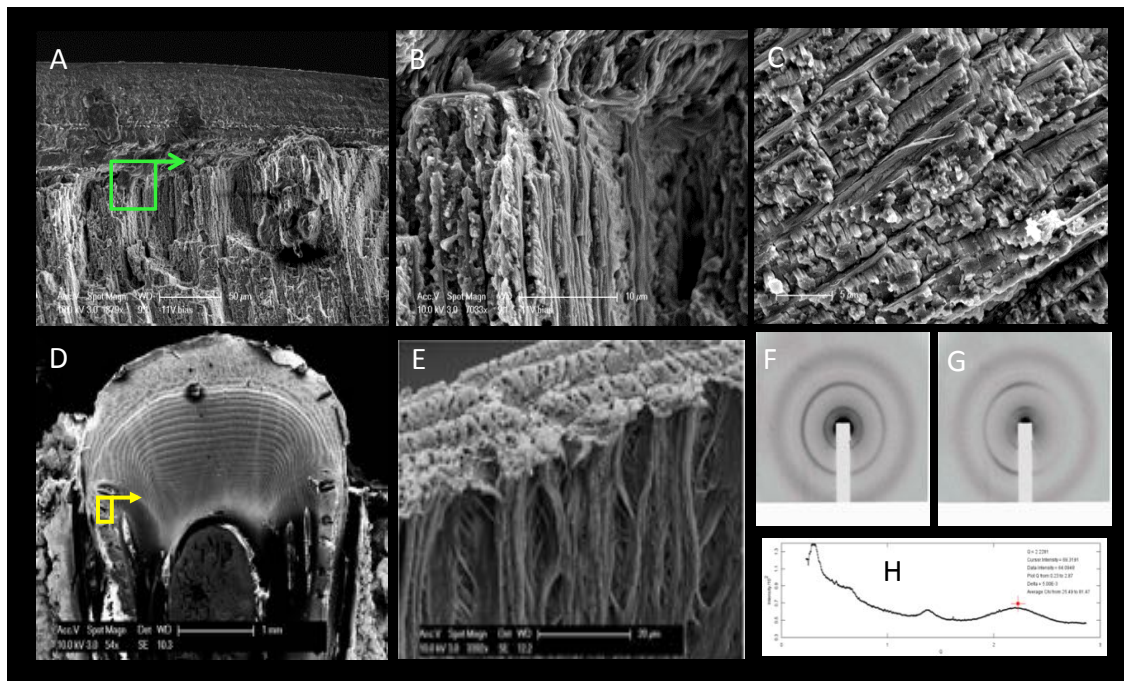


Figure 41. Demineralization of striated region. (A and D) region of club that was examined. (B and E) Longitudinal view of oriented chitin fibers. (C) plan view of transverse section. (F-H) Synchrotron scan showing presence of chitin with orientation perpendicular to transverse surface.

In year 2, we continued our analysis of the striated region by utilizing TEM methods. As seen in Figure 41, fibers seem perpendicular to the transverse section. We investigated this further by taking sections from the club shown in the higher magnification SEM micrographs in Figure 42.

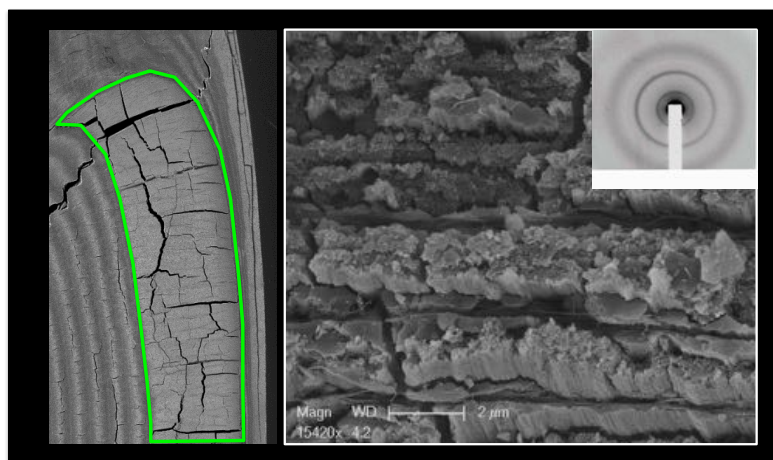


Figure 42. (Left) Transverse section of club with the striated region highlighted in green. (Right) Higher magnification SEM micrograph showing aligned sheets coming out of the plane of the section. (Inset, right) Synchrotron diffractogram from the striated region, with the beam approximately parallel to the chitin's c-axis, confirming the presence of alpha-chitin fibers oriented perpendicular to the transverse plane and surrounding amorphous mineral.

When we looked more closely at the surface of these fibers, we see that they consist of rod-like elements that have a particulate nature (Figure 43).

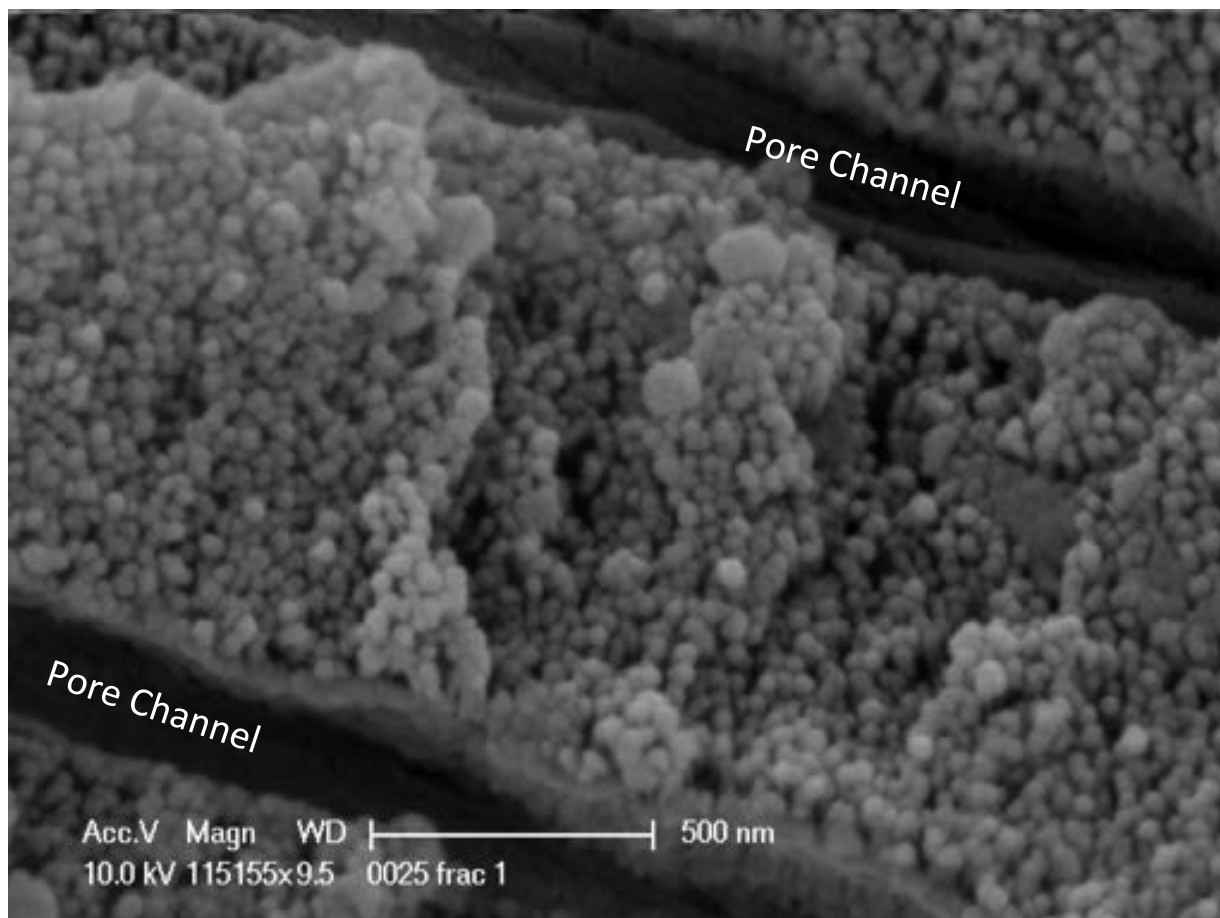


Figure 43. Higher magnification SEM micrograph of striated region showing aligned rods made of particles.

TEM investigations (Figure 44) of this region shows that these are ~ 25 nm mineralized rods with a 3 nm organic core.

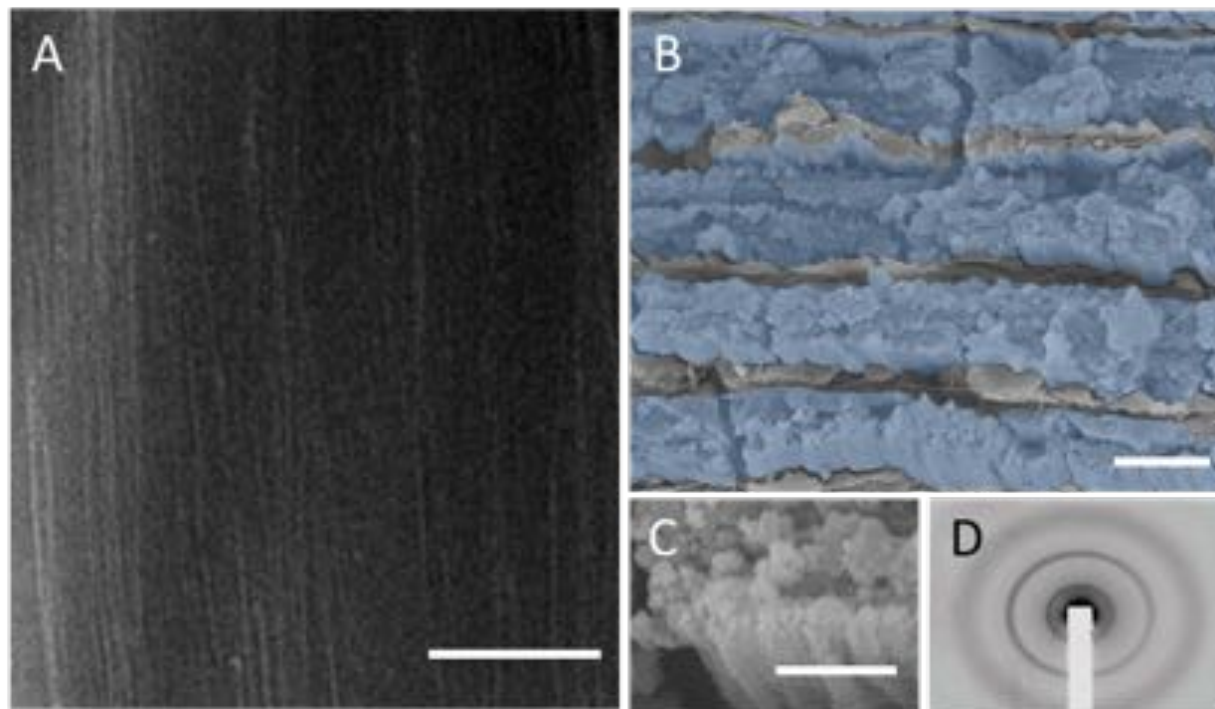


Figure 44. Analysis of striated region from *O. Scyllarus*. (A) TEM of a sagittal thin section again shows the aligned fiber structure in the striated region. Scale bar is 100 nm. (B) Transverse fracture surfaces from the striated region reveal a sheet like structure, composed of mineralized rods, oriented perpendicular to the transverse section. Scale bar is 2 μm . (C) Magnified SEM micrograph of aligned mineralized bundles. Scale bar is 0.5 μm . (D) Representative electron diffraction pattern from a transverse section of the striated region with the (110) α -chitin reflection measured as a non-uniform ring, indicating that the c-axis of the α -chitin fibers is oriented perpendicular to the transverse face (parallel to the beam).

Analysis of this micrograph confirms our SEM and synchrotron observations that alpha-chitin fibers form the basis for inorganic growth and these inorganic/organic hybrid sheets wrap around the club, placing it under compression. It is this compression that provides toughening by resisting crack growth in the club and thus, prevents catastrophic failure.

Sectioning the club through three orthogonal planes (sagittal, coronal, and transverse, Figure 45A) provides a three-dimensional view of the ultrastructural features within the club. Optical micrographs (Figure 45B-E) provide wide field views of the bulk features of the club, with a transverse cross section (Figure 45D, E) demonstrating the multi-regional nature of the club. The striated region (dashed yellow line, Figure 45E) is observed on either side of the periodic region (which constitutes the majority of the endocuticle) and is adjacent to the exterior surface. Observations of a coronal section (Figure 45C) uncovered that the striated region wraps around the circumference of the club.

A transverse fracture (Figure 45F) of the club highlights that the region is shown to indeed be composed of stacked layers of mineralized sheets. Here, the fibers composing the sheets are

oriented perpendicular to the field of view. A coronal fracture (Figure 45G) reveals the presence of pore channels running left to right (highlighted in yellow), with the mineralized fibers that make up each layer of the striated region extending from top to bottom.

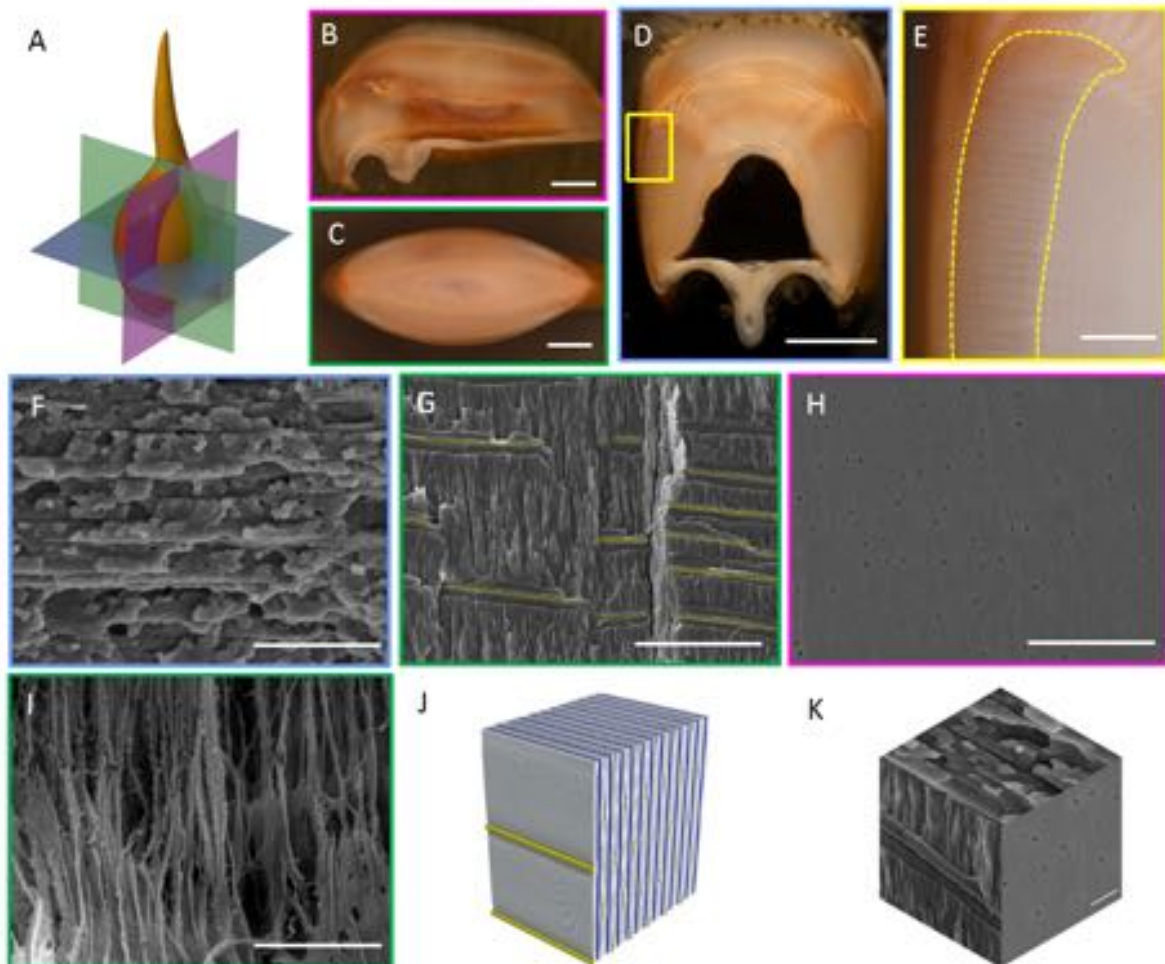


Figure 45: A clarified structure of the striated region viewed in three perpendicular directions. The planes of view are the (A) sagittal (magenta, B), coronal (green, C) and transverse (blue, D). Scale bars in (B)–(D) are 1mm. The striated region is observed on each side of a transverse cross-section and is defined by a series of parallel striations (E). Scale bar in (E) is 200 μm . SEM micrographs of fractured specimens reveal stacked sheets of parallel fiber layers in a transverse section (F), and a side view of pore canals (highlighted in yellow) connected by perpendicular mineralized fiber layers in a coronal section (I). A network of pore canals is clear in an ion polished (H) sagittal section, Scale bars in (F) – (H) are 10 μm . Demineralization of a sagittal section (I) reveals a predominately bundled architecture of the organic –chitin, and the parallel fiber structure. Scale bar in (I) is 2 μm . A schematic showing the architecture of the striated region is presented in (J), and a three-plane representation with SEM micrographs is shown in (K). Scale bar in (K) is 2 μm .

Pore channels run from the interior of the club outward, traversing the entire club and continuing through the periodic region (Figure 46) and are similar in design to the pore channel networks observed in other Crustacea including lobster and crab. These observed pore channels likely serve as ion transport pathways during mineralization, and potentially enable self-healing. An ion

polished sagittal section provides a clearer view of the geometry of pore channels (Figure 45H), which are circular in cross-section, with an average diameter of 246 ± 52 nm and constitute an area fraction of 0.53 ± 0.06 %. In typical crustacean exoskeletal regions, pore channels run perpendicular to the rotating Bouligand fiber layers, and thus take on a twisted ribbon appearance. Because the striated region is formed from mineralized fibers oriented in one direction, however, the clearly visible pore channels in this region run straight, perpendicular to the aligned fibers.

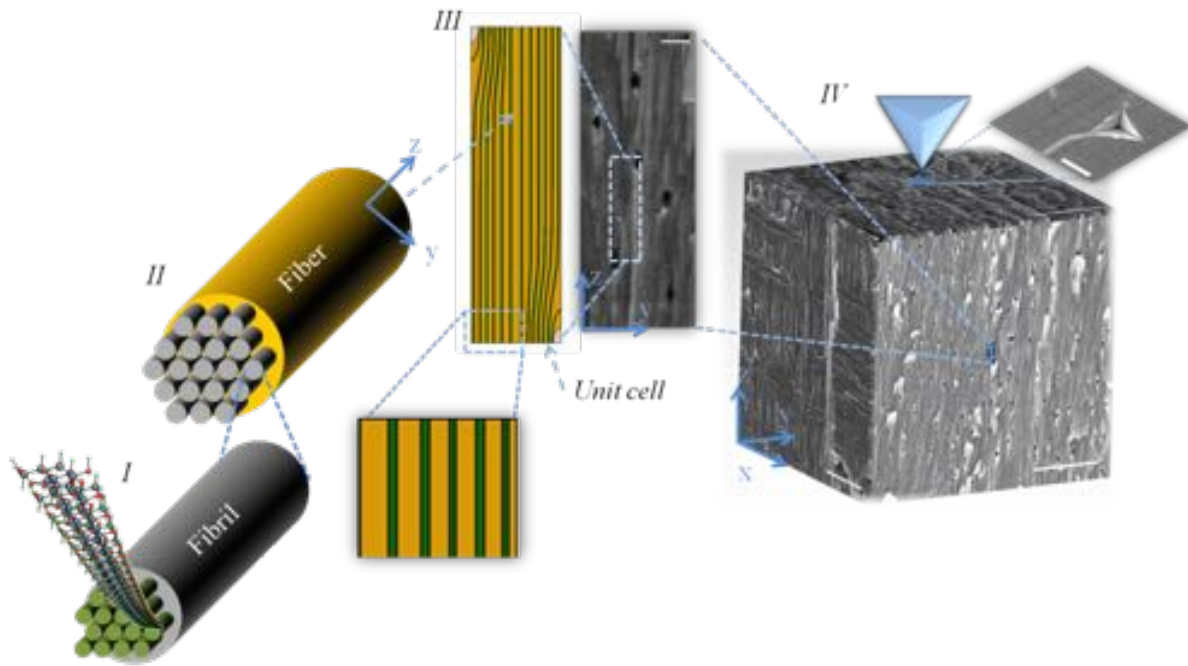


Figure 46. Hierarchical structure of striated region. (I) Hierarchical level I: alpha-chitin chains wrapped by amorphous mineral to form fibrils. (II) Hierarchical level II: Fibril bundles surrounded by mineral-protein matrix to form fibers. (III) Hierarchical level III: Fibers (yellow) surrounded by mineral to form sheets (green). Image III also shows the FEM unit cell employed in this analysis. The scale bar in the SEM micrograph in III is 0.5 μ m. (IV) 3D representative volume element depicting nanoindentation on the transverse face of the striated region. Scale bar 5 μ m.

The mineral phase in the striated region is composed primarily of amorphous calcium carbonate and calcium phosphate. The details of the arrangement of the organic material within the mineral are an important factor in understanding the mechanical properties of the region, and are provided through microscopic analyses of demineralized specimens (Figure 45I), transmission electron microscopy (TEM), and synchrotron x-ray diffraction (see Figure 44). These investigations confirm that the striated region indeed consists of aligned α -chitin fibers oriented parallel to sagittal or coronal sections, and are therefore perpendicular to a transverse section. The organic fibers that form the scaffold of the striated region likely act to template the formation of mineral, yielding a laminated structure.

The interspersed network of pore channels, along with the interfaces between mineralized fiber sheets, give the striated region its striped appearance. A fully developed three-dimensional schematic of the region is presented in Figure 45J, with the mineralized fibers layers in gray,

interfaces in blue, and pore channels in yellow. A corresponding arrangement of SEM micrographs is shown in Figure 45K.

In the final year of this project, we wanted to investigate in more detail, the rationale behind the development of this striated region. The striated region exhibits microstructural features which deviate significantly from the helicoidal motif, initially suggested to be formed from parallel bundles of mineralized rods with α -chitin cores. This region is a unique feature of the stomatopod cuticle, with implications for impact resistance. The aligned fibers of the striated region wrap around the circumference of the stomatopod club, in much the same way that boxers wrap their hands with tape before a fight. The role of the striated region in preventing damage from a high-energy strike has been interrogated through preliminary finite element models. The region has been shown to provide resistance against lateral deformation of the club, along with compressive and torsional stiffness. The atypical architecture of the region is well suited to such a purpose, as aligned fiber composites are known to be stiff and strong in the fiber direction. The strike from a spearing stomatopod is different from that of a smashing stomatopod and therefore, we pose the question: If the forces exerted are different, is there a change in the underlying microstructures within the dactyls? To address this question, we probe the ultrastructures of the striated region in both spearing and smashing stomatopods.

In general terms, stomatopods can be divided into two groups: the “spearers” that attack soft-bodied prey with a harpoon-like structure, and the more recently evolved “smashers” that crush hard-shelled prey using a hammer-like club. The stomatopod fossil record, which extends back at least 350 million years (MA), suggests that early stomatopods employed multiple raptorial, thoracic appendages in prey capture using spearing action. However, some 150 MA ago the second thoracic appendage became distinctly prominent. In many living groups this appendage retains spearing function, but characters associated with the smashing habit evolved by 70 MA. Recent phylogenetic analyses based both on form and genes are congruent in suggesting smashing to be a derived habit. The appearance of the earliest smashers contributed to a dramatic rise in the number of marine families employing predation by shell breakage that was part of the Mesozoic marine revolution. This evolutionary diversification was accompanied by an “arms race” between predators with increasingly sophisticated weaponry and prey with more effective defenses. The appearance of the stomatopod smashing habit coincided both with the appearance of several new clades of fish, other kinds of crustaceans, and predatory gastropods¹¹ that target shell dwellers specifically. Patterns of shell damage arguably specific to smashing stomatopods are known among fossils and extend back at least 15 MA.

Odontodactylus scyllarus is a smashing stomatopod, which employs a raptorial strike that reaches speeds of 14-23 m/s. *Lysiosquilla maculate* in contrast, is a member of the evolutionarily older group of spearing species. Spearing stomatopods utilize a slower strike (average linear speed 2.3 m/s) in an ambush-style attack. While spearing stomatopods exhibit an elongated and barbed raptorial appendage, smashing stomatopods possess a bulbous dactyl club (Figure 47).

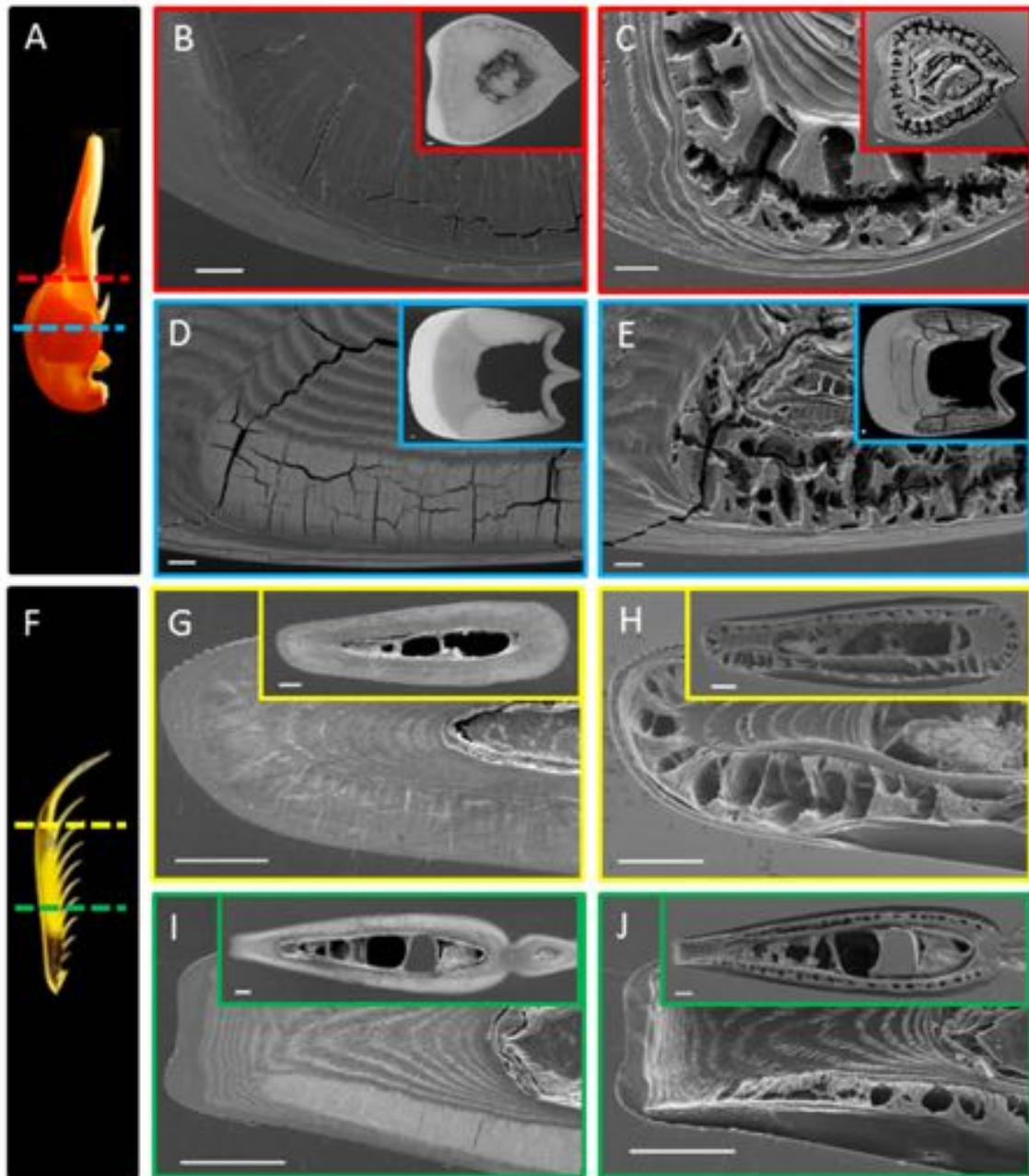


Figure 47: The striated region has been repurposed in the impact zone of the smasher club to provide impact resistance. (A) Bulk view of smasher club, with dashed lines showing the locations of cross sections at the center of the club (blue) and the base of the spike (red). SEM micrographs at the base of the spike before (B) and after (C) demineralization, revealing the striated region, which wraps the entire structure. Micrographs in the impact zone of the bulb of the club before (D) and after (E) demineralization revealing a striated region isolated on either side of the club. (F) Bulk view of a spearer spike, with dashed lines highlighting the locations of cross sections at the center (green) and tip (yellow) of the spear. SEM micrographs near the top of the spike before (G) and after (H) demineralization demonstrating a striated region that wraps the entire structure. Micrographs at the center of the spike before (I) and after (J) demineralization, showing that the striated region wraps the entire club at all locations, providing evidence for impact tolerant exaptation in the smasher club structure.

The forces exerted during a strike, and thus the underlying structures within the dactyls of spearing and smashing stomatopods, should be different. During an impact event, the dactyl of *O. scyllarus* folds into the adjacent propodus to form a functional club. The organism is capable, however, of separating these two segments, revealing a spike that protrudes from the dactyl. This spike functions as a piercing weapon, used to impale soft-bodied prey. Unlike the functional club utilized by the smashing stomatopods, the spearing species elongate and separate the dactyl, propodus and merus during attack, grasping prey between the dactyl and propodus. How these disparate structures influence the stresses generated during a raptorial strike in spearing and smashing species remains unknown. This mystery is best resolved through examination and comparison of the ultrastructure of the smashing stomatopod with its spearing ancestor.

Low magnification electron micrographs of intact and demineralized transverse cross sections at two different positions within the smashing dactyl of *O. scyllarus* and the dactyl of the spearing species, *L. maculate* reveal (Figure 47) the highly oriented mineralized fibers within the striated region (which run perpendicular to the transverse cross section). The rapid demineralization along the fiber direction clearly distinguishes the striated region from the periodic and impact regions, which contain organic layers oriented within the transverse plane, preventing rapid demineralization.

A comparison of transverse cross-sections from the dactyl club of *O. scyllarus* (Figure 47A-C) at the center of the bulb, near the impact zone (dashed blue line) and at the basal support of the protruding spike (dashed red line) reveals a significant change in the location of the striated region. In the region of the protruding spike (Figures 47B, C) the striated region wraps around the entire structure, while in the bulbous region of the club, where impact occurs, the striated region takes on a different morphology (Figure 47D, E). Here, the region is observed only on the sides of a transverse cross section, indicating that it wraps the club, from the top of the bulb to the tip of the spike, but does not extend to the impact surface. This modification to the striated region results in enhanced impact resistance. Upon impact, the helicoidally oriented fiber layers in the periodic region are compressed, leading to a state of biaxial stress in the plane of each sheet. This, in turn, causes Mode I fractures to nucleate and grow within the periodic region. The nucleation, growth, and control of these fractures is the dominant energy dispersion mechanism in the club. Confining cracks within the periodic region is critical to avoiding propagation of fractures through to the surface of the club, which would result in catastrophic failure. The striated region, with aligned fibers wrapping around the circumference of the club, is able to withstand the out of plane tensile loads induced by strain in the periodic region, providing support to the energy absorbing periodic region and aiding in the containment of cracks within the interior of the club. By limiting the strain within the periodic region to allow fractures nucleate and grow, while at the same time constraining their driving force, an optimal energy dispersive and impact resistant structure is formed. Similar observations have been reported for unconfined and confined brittle materials under dynamic impact. This mechanism is explored in further detail in the following section, through the implementation of finite element models.

If, as hypothesized, the striated region serves the function of preventing catastrophic propagation of cracks in the bulb of the stomatopod club during impact, a natural question arises: why does the region surround the spike of the club?

Cross sectional views near the tip (dashed yellow line, Figure 47F, G, H) and the center (dashed green line, Figure 47F, I, J) of a dactyl spear from *L. maculate* reveal a striated region that wraps around the entire structure at the tip (Figure 47G, H). This is in contrast to the morphology observed in the club of *L. maculate*, which nearly connects in the location analogous to the impact surface of a smasher, at the center of the spear (Figure 47 I, J). Unlike the club of the smasher, the critical loading condition encountered by a spearing dactyl is not directional impact loading, but rather a multi-directional flexural stress. A striated region, with aligned fibers oriented along the long axis, is an ideal substructure to support the torsional loading of a high aspect-ratio spear. In fact, because the perimeter of beam's cross-section experiences the largest stresses when loaded, it is common practice in the design of composite materials to reinforce a flexural member with longitudinal fibers. Despite significant differences in the macrostructure between spearing and smashing stomatopods, fractured surfaces of both dactyls confirm that the striated regions have similar microstructures (see Figure 44). This aligned, fiber-reinforced design of the striated region has been adapted from spearing stomatopods into the club of smashing species.

Mechanics and Modeling:

Complementary mechanical characterization experimental techniques, including depth-sensing nanoindentation and microindentation in conjunction with state-of-the-art computational models, were used to characterize the modulus, hardness, strength and toughness of the longitudinal and cross-sections of the dactyl clubs and to elucidate the primary toughening and strengthening mechanisms at various length scales.

Nanoindentation: A stand-alone nanomechanical test instrument (TI 950 Triboindenter, Hysitron, acquired via an AFOSR-sponsored DURIP) was used to perform depth-sensing nanoindentation experiments on the polished longitudinal and cross-sectional specimens of the dactyl clubs to create the higher resolution multi-sectional modulus and hardness maps. Multiple indentations, with spacings dependent on the predetermined local indent damage field, were performed to various depths (10-300 nm) at different locations (in the impact, periodic and striated regions of the club) on each sample to obtain the depth and regio-specific mechanical properties. Prior to these experiments, surface profilometry in combination with SEM was used to monitor the surface roughness to ensure that surface texture will not become a test variable. The elastic modulus and hardness will be derived from the load-displacement information following the Oliver and Pharr method. Additionally, computational multiscale models were employed to simulate the nanoindentation tests, taking into account the underlying ultrastructure to reveal the energy dissipation mechanisms acting at smaller scales.

In addition, our computational models also allowed us to study crack initiation and growth. This combination provided the necessary tools to characterize the intrinsic strength and toughness of the ultrastructure for different failure modes.

Because we are interested in impact tolerance, and the fundamental properties responsible, we used preliminary data of nanoindentation mapping and line scans (Figure 48) to guide our further examination of specific regions of interest. Compressive modulus and hardness maps of the transverse cross-section correlate strongly to mineral concentration as would be expected. The dactyl club exhibits a greater number of specialized modules (regions) at the ultrastructural level

than has previously been seen in biological composites. This is partly due to the club's ability to specialize for a known impact, deviating from the necessity for armor to be translationally symmetric.

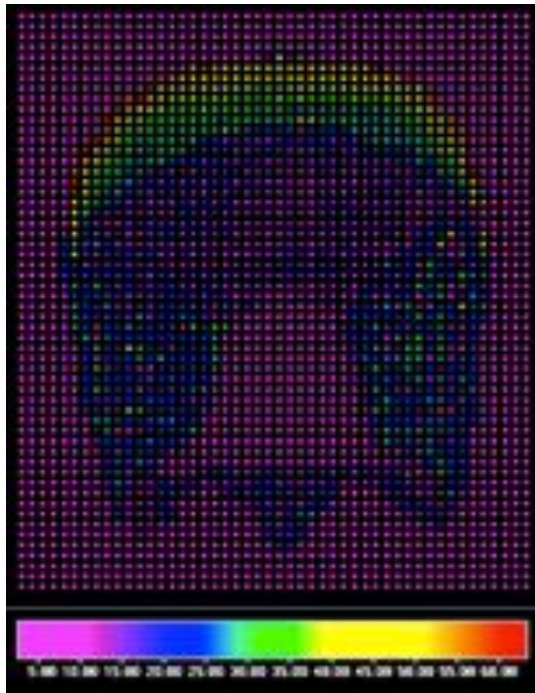


Figure 48. Nanoindentation map (modulus) of transverse section of dactyl club highlighting regional differences in mechanical properties.

Based on nanoindentation results and analyses, it seems our results suggest that crack propagation across layers is hampered by the modulus oscillation, which improves the damage tolerance with an efficiency that depends on the crack propagation direction relative to the chitin fiber orientation. This prediction was supported by the observed presence of micro-cracks crossing the helicoid and arresting within a few layers in scanning electron micrographs of transverse polished cross-sections.

In year one, line scans of indents (similar to those in the preliminary data, but with better prepared samples and closely spaced indents) were performed in the periodic region (Figure 49).

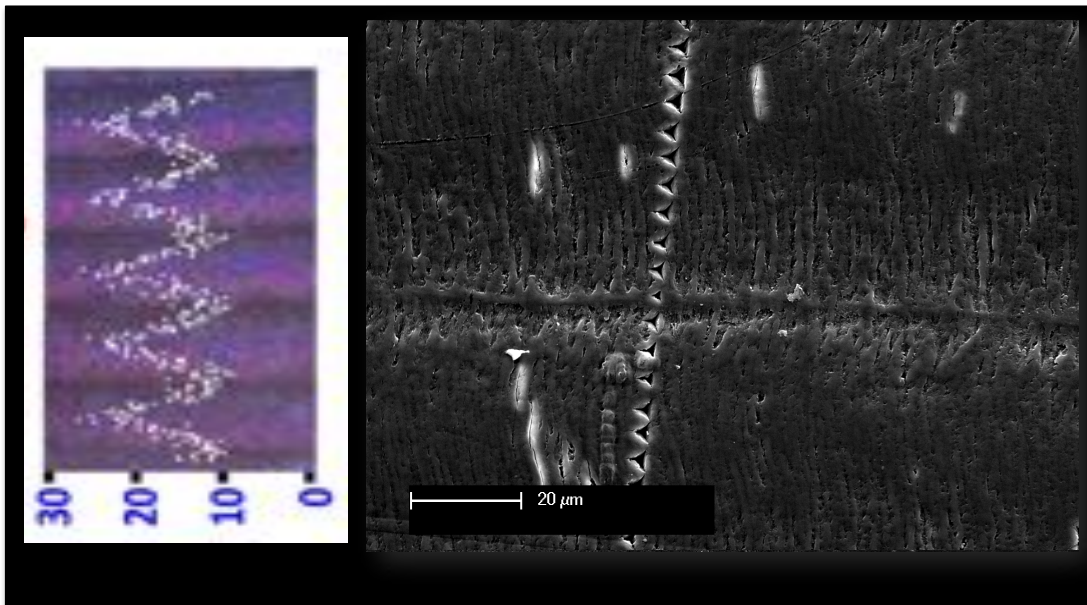


Figure 49. Left: Nanoindentation reveals a periodicity in modulus versus location within the periodic region. Right: Post-indentation SEM highlighting the change in size of indents as they cross a 0° boundary.

Based on our previous observations, one key implication is that this periodic pattern formed within a helicoid creates a much larger surface area per unit crack length in the main direction of propagation, hence amplifying the total energy dissipated during impact and crack propagation. It is known that when a crack deviates from its helicoidal path and propagates straight into neighboring layers, it encounters an elastic modulus oscillation due to their anisotropic stiffness. This oscillation period is on the order of 75 μm , and the relative thickness of stiff (E_{max}) and compliant (E_{min}) layers depends on the angle of the crack front relative to the helicoid axis. Based on work by Fratzl et al., this oscillation provides an additional protection against damage. Indeed, the J-integral crack driving force, J_{far} , surrounding the crack is shielded at the tip, $J_{\text{tip}} = J_{\text{far}} \cdot f_{\text{inh}}$, where f_{inh} is the shielding factor, which directly depends on the relative thickness and modulus ratios $r = E_{\text{max}}/E_{\text{min}}$. We used our nanoindentation line-scan profiles to fit the oscillation wavelength and modulus ratio r , and applied this analysis to the club (Figure 50). These results suggest that crack propagation across layers is hampered by the modulus oscillation, which improves the damage tolerance with an efficiency that depends on the crack propagation direction relative to the chitin fiber orientation.

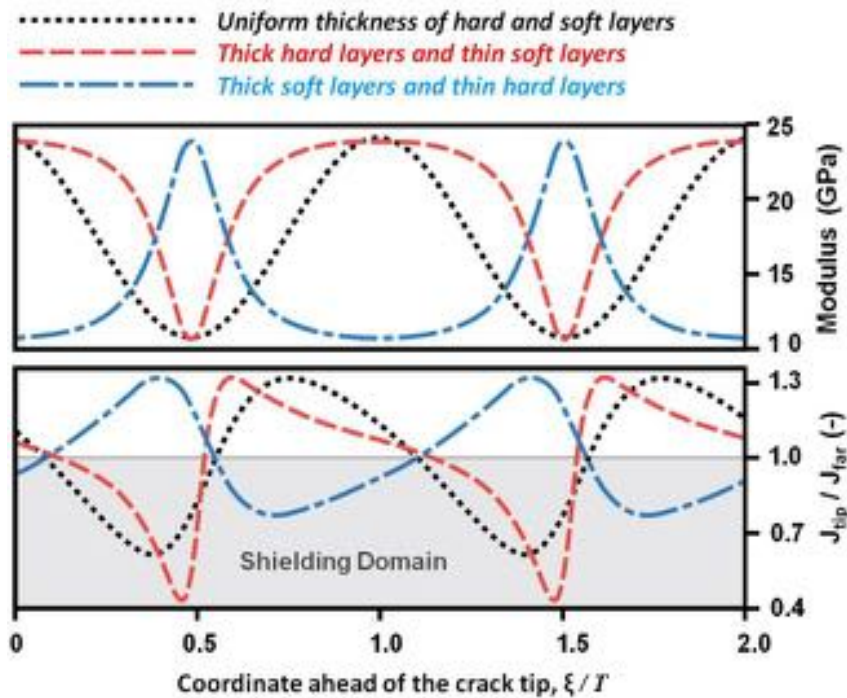


Figure 50. Analytical model showing effect of modulus oscillation on shielding at the crack tip.

In year two, we continued performing high resolution nanoindentation mapping (Figure 51) to make structure-functional relationships with site specific features within the impact region. Here, sagittal-sectioned samples were polished with progressively finer grit down to 50 nm. Each pixel in Figure 51 represents an individual indent. For low magnification arrays there are 40 x 40 points with 30 μm spacing and for high magnification arrays there are 47 x 47 points with 3 μm spacing, which provided excellent resolution.

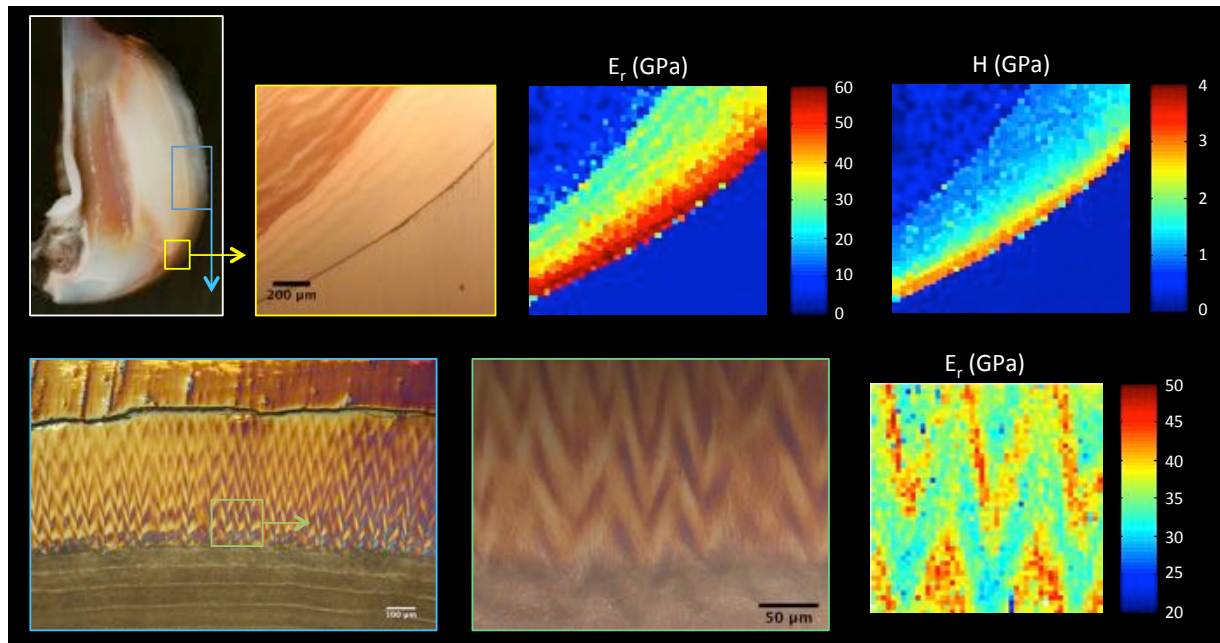


Figure 51. Indentation maps of impact region of dactyl club. Upper, left: Bright field optical images of impact region. Upper, right: Low magnification nanoindentation maps of yellow box region showing gradients in reduced modulus and hardness through the impact region and near the club surface. Lower, left: Differential interference contrast images of boxed blue region highlighting the impact surface, bulk impact, and periodic regions and a high magnification DIC image of bulk impact region as denoted in optical micrographs highlighting the herringbone pattern. Lower, right: High resolution indentation map of blue boxed region displaying oscillating elastic modulus correlating with herringbone pattern observed within the bulk impact region.

A series of higher load indents (50mN – 1600mN) were also placed on the impact region of the club (Figure 52).

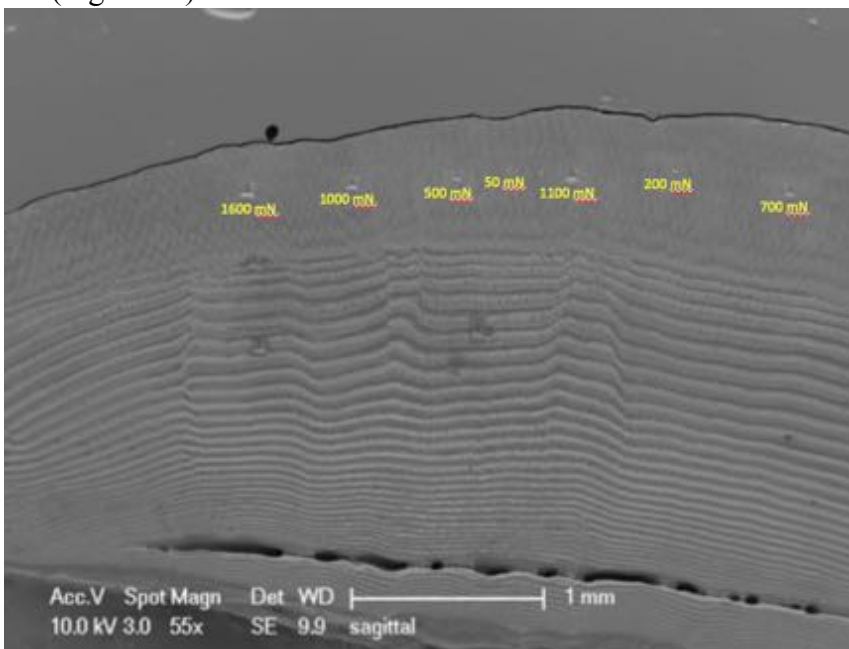


Figure 52. High load nanoindentation on a sagittal surface of the dactyl club in the impact region.

After indentation, closer analysis (Figure 53) revealed interesting trends in crack propagation.

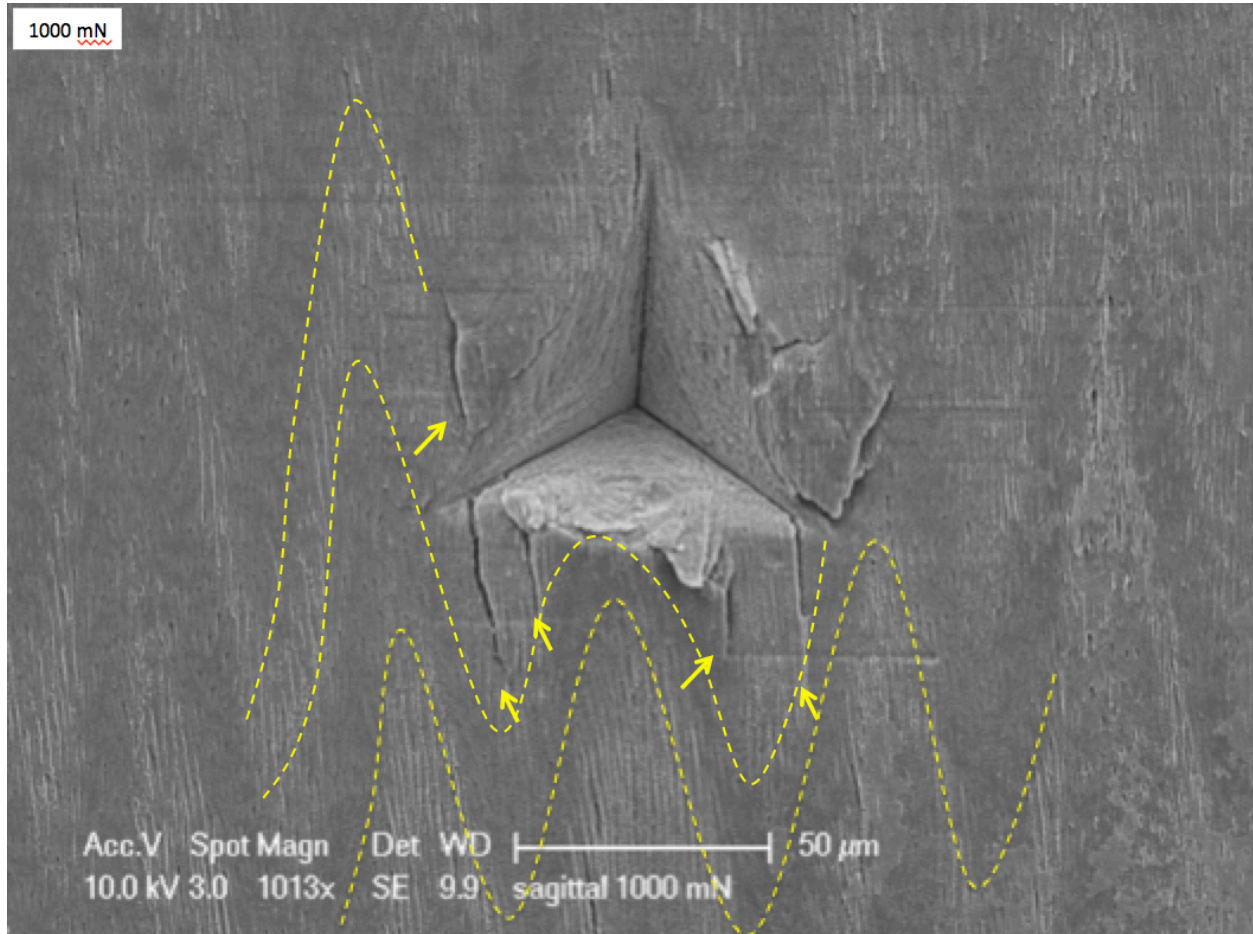


Figure 53. High resolution SEM of post-indent in impact region. Yellow lines highlight herringbone structure and arrows show cracks.

After this indentation, the specimen was treated in 5% acetic acid to reveal specific features of the indentation. Specifically, we see that cracks are only apparent in the areas where there is out-of-plane fiber orientation; however, cracks are most likely following the rotation of the fibers. A close observation of a piece of material that had spalled off from a 1600 mN indent (Figure 54) also shows the presence of fiber bridging, which likely adds toughness to the structure.

It is clear from these observations, that the presence of the helicoid, even in the impact region, provides local toughening that prevents catastrophic failure specific to this region. This way, cracks that form within this region have a tortuous path to enter into another region or out of the club.

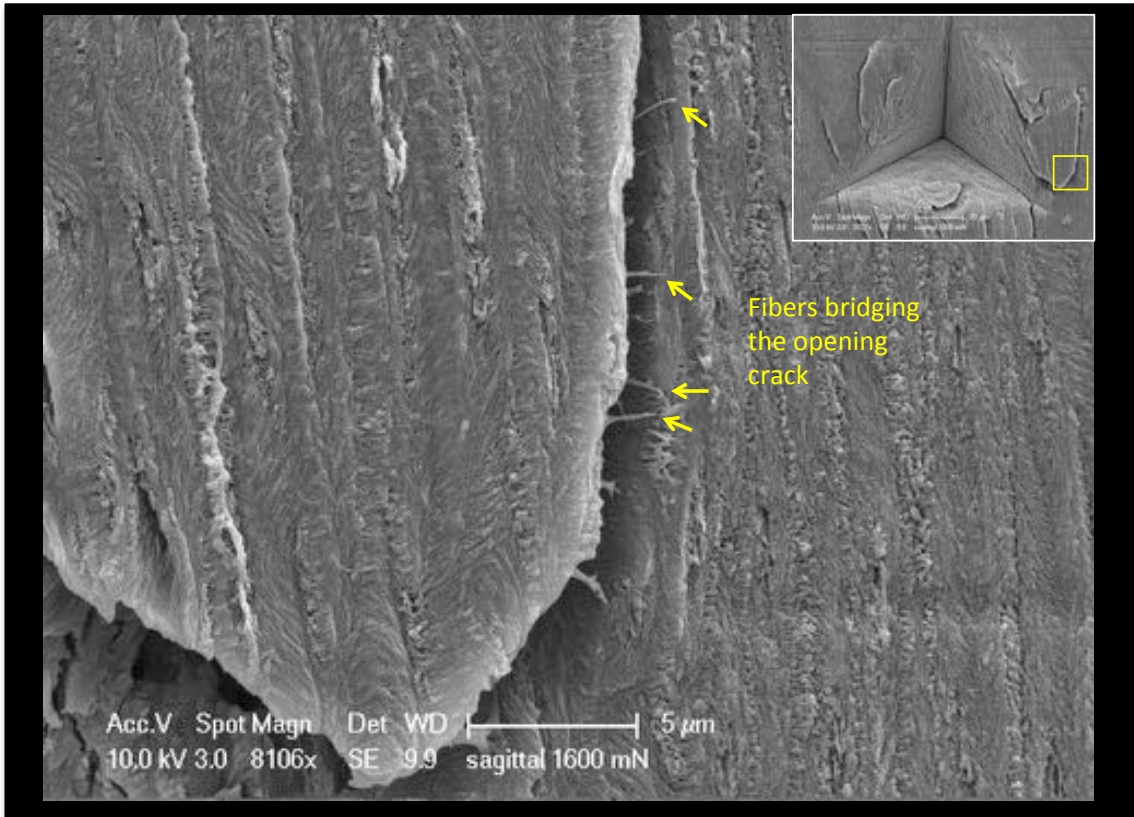


Figure 54. High resolution SEM of post-indent (1600mN) in impact region. Yellow arrows highlight fiber bridging.

In the final year, we investigated the mechanical properties of the impact surface, which revealed some interesting observations about its role. Specifically, we performed high load indentation along the coronal surface of the club, both within impact region and on the impact surface (Figure 55).

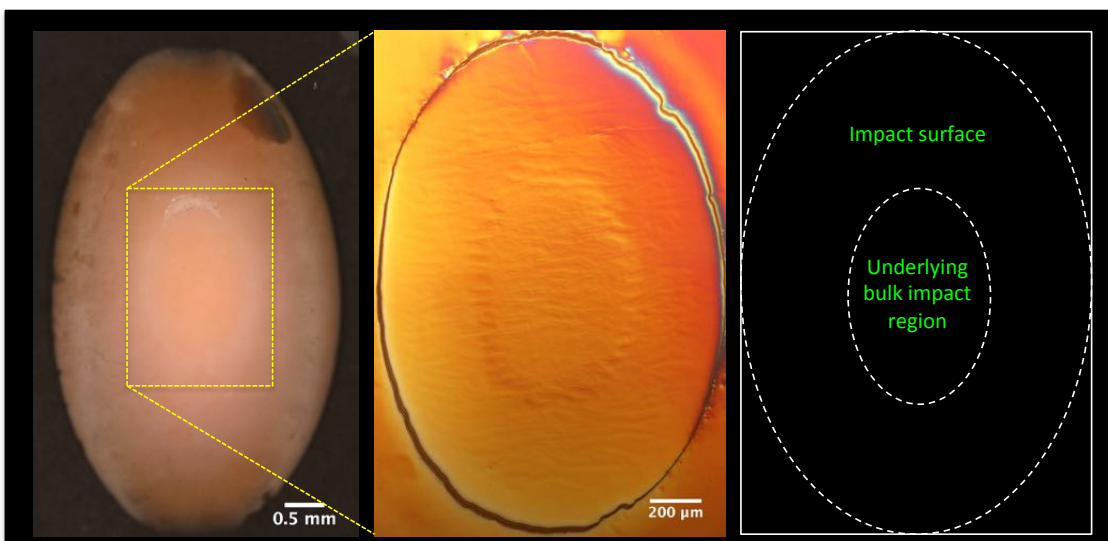


Figure 55. Region of nanoindentation for coronal section of club.

In this work, we performed a series of low to high load nanoindentations (Figure 56). on the coronal section of the club and subsequently polished through this region such that the impact surface was removed and the impact region was revealed.

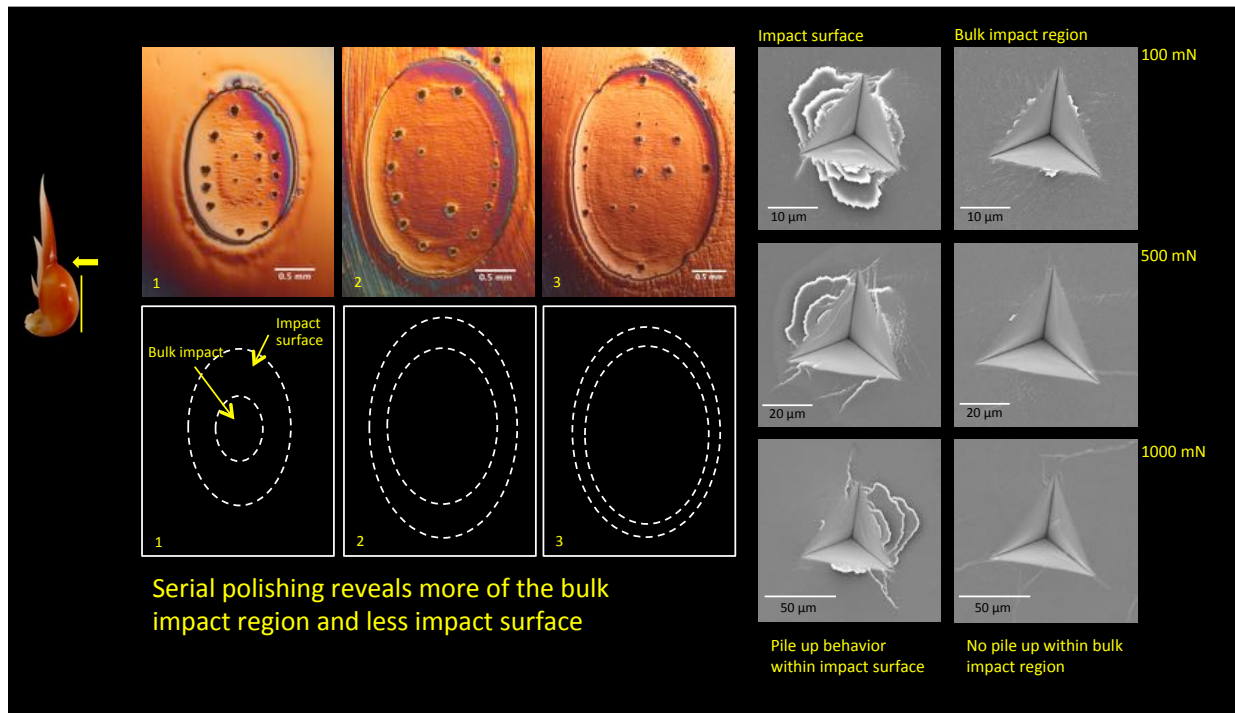


Figure 56. Series of nanoindentations along the impact region of the dactyl club in the coronal direction.

There are a few interesting aspects about this data. The initial indents into the impact surface show a significant amount of plastic deformation and pile-up. Cracks appear to form in this region, but not necessarily from the corners of the indentations. One observation was made in the 500 mN indent for the impact surface. Here, there seems to be a damage field surrounding the region of pile up. What is believed is that the nanoparticulate nature of the impact surface provides toughening via displacement of particles beyond the indent. These particles, which are not crystallographically connected, are surrounded by an organic matrix that provides a pathway for particle sliding and rotation. Additional observations of sliding needs to be confirmed. As the serial polishing removed the impact surface, the impact region (containing the herringbone structure) was revealed. Indentations in this region showed cracking at the indent corners. However, additional investigation of this region beyond these cracks uncovered that some cracking displayed an “s-like” pattern (Figure 57). It is likely that the directionality of this cracking follows the herringbone pattern observe in the impact region. In fact, if we observe the coronal section that was demineralized (Figure 58), this pattern can clearly be observed. Thus, cracks are being redirected not only in the helicoidal pathway, but also along the herringbone interfaces, which contain pore canals that can redirect cracks.

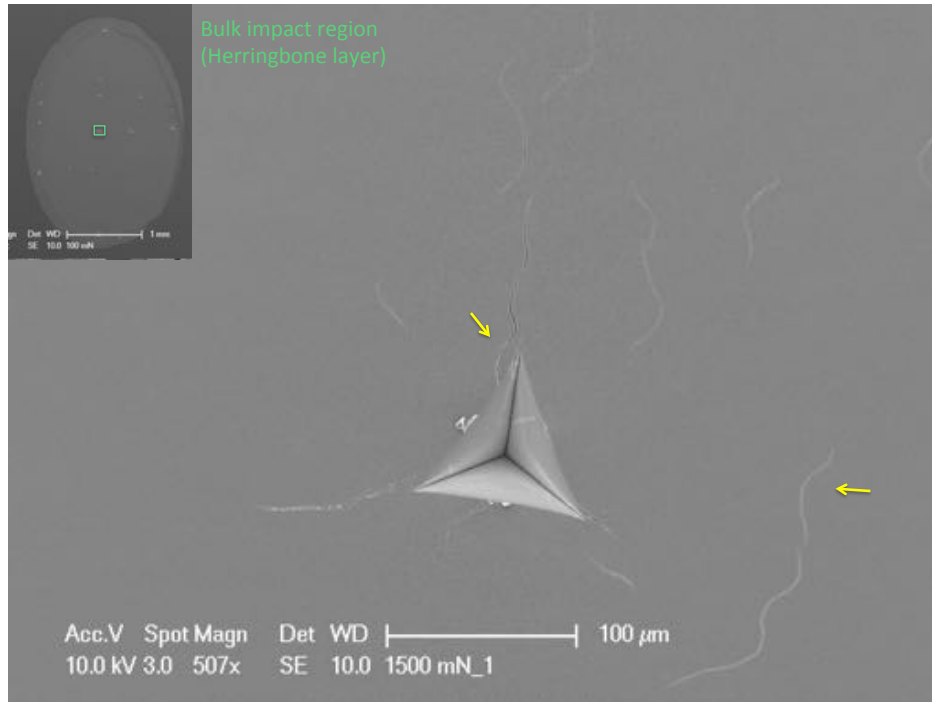


Figure 57. High load (1500 mN) indentation of bulk impact region. Yellow arrows highlight “s-like” cracks that have formed.

In fact, if we look carefully at the network of pores (Figure 59), it becomes apparent that these pores may, in fact, act as nucleation sites for micro-cracking ahead of the crack front - reducing driving force for crack propagation, which would also reduce strain in the club and lead to enhanced toughening.

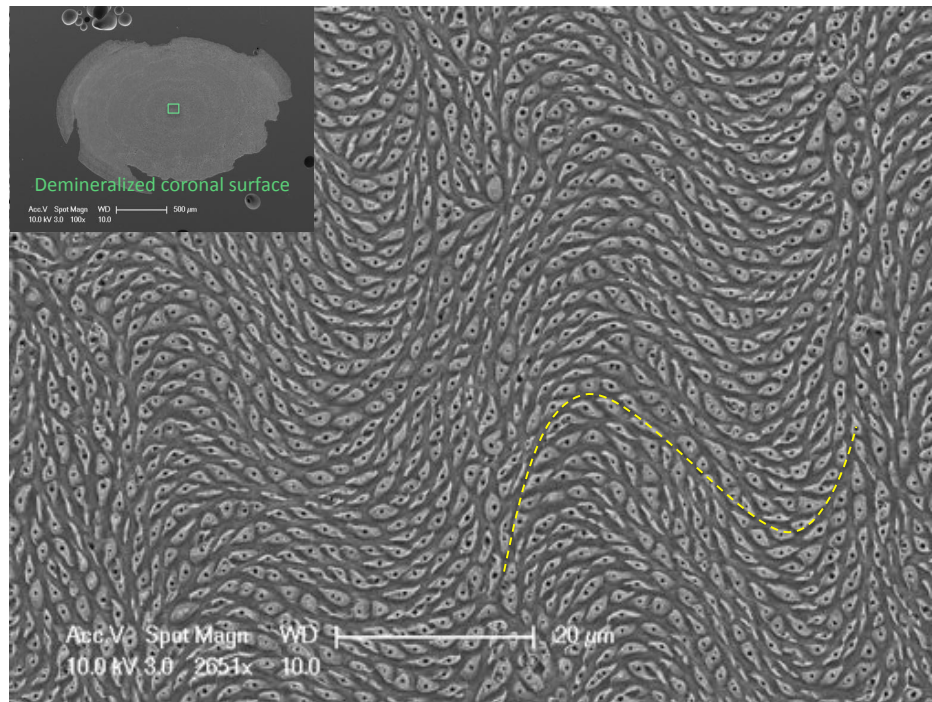


Figure 58. Demineralized coronal section of the impact region that reveals herringbone structure and pore canals.

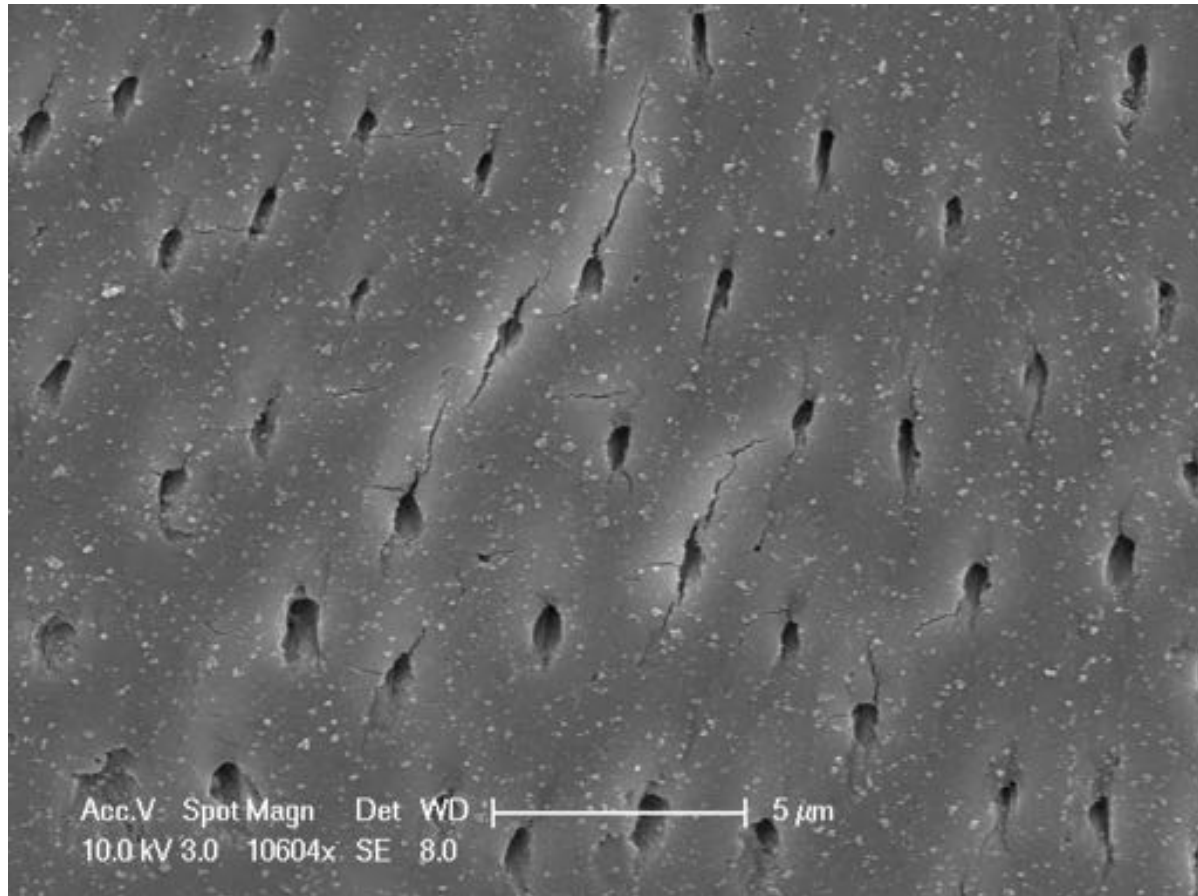


Figure 59. Demineralized coronal section of the impact region that reveals herringbone structure and pore canals.

Self-Healing Observations:

Towards the end of this project, we made some additional observations that were beyond the scope of this project. One of these was the potential ability for the club to heal damaged regions. An example of this was found in a club that had been in use for ~ 2 months. After separation of the club and fracture along the sagittal plane (Figure 60), we observed some region close to the surface of the impact region. A crack which had formed parallel to the club's surface had propagated along the club and had partially separated. This crack had some fibers that seemed to bridge across this crack. The fibers were, in fact, the organic tubes that were the pore canals. However, in regions where the crack had expanded significantly, these fibers were severed. We observed particles that had started to reform across the organic fibers and align along their long axis (Figure 61). Whereas the particles forming in regions where the fibers had severed were not oriented and did not bridge the crack (Figure 62). In either case, the particles had a spherulitic nature, suggesting a high concentration of inorganic precursor had been injected into this region, possibly a response to a damaging event.

Fractured Sagittal plane

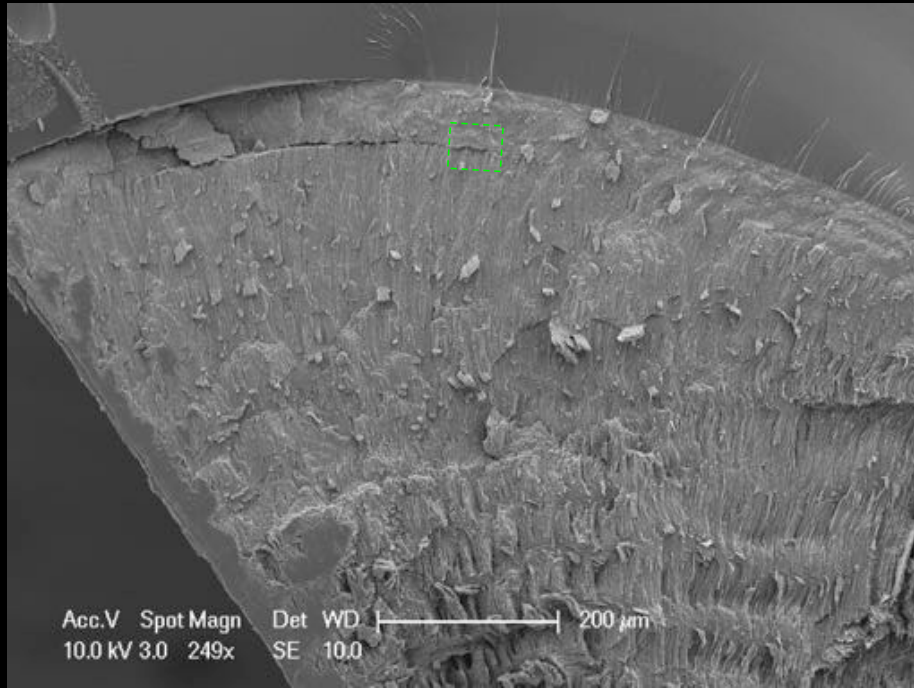


Figure 60. Sagittal fracture of dactyl club that was damaged in use.

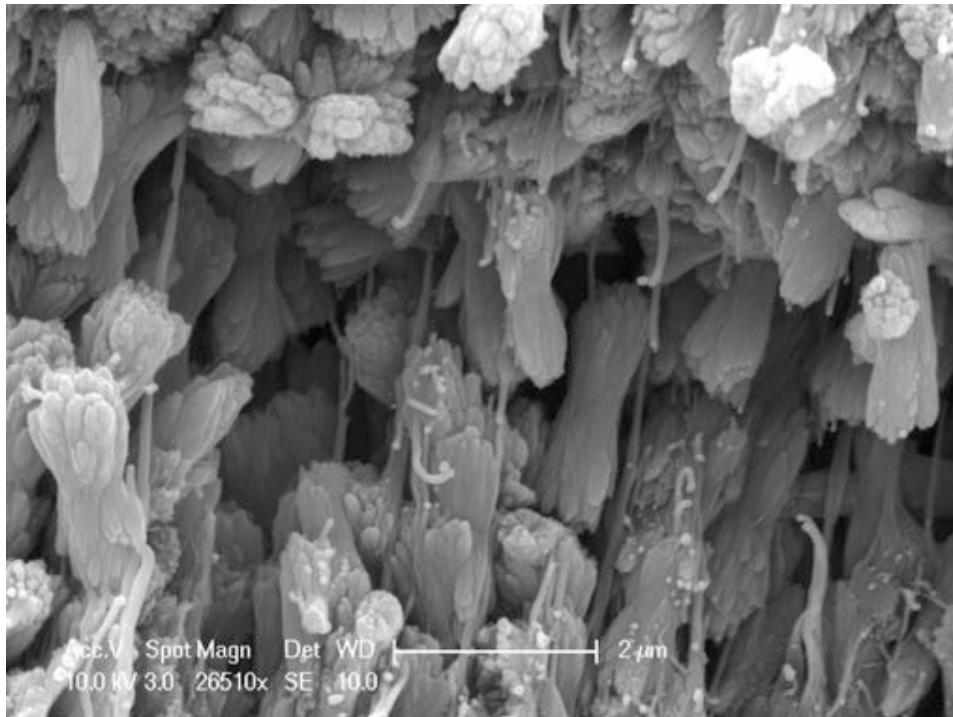


Figure 61. Spherulitic particles growing across crack and aligned parallel to tubules. Particles near the crack surface not attached to fibers are misoriented.

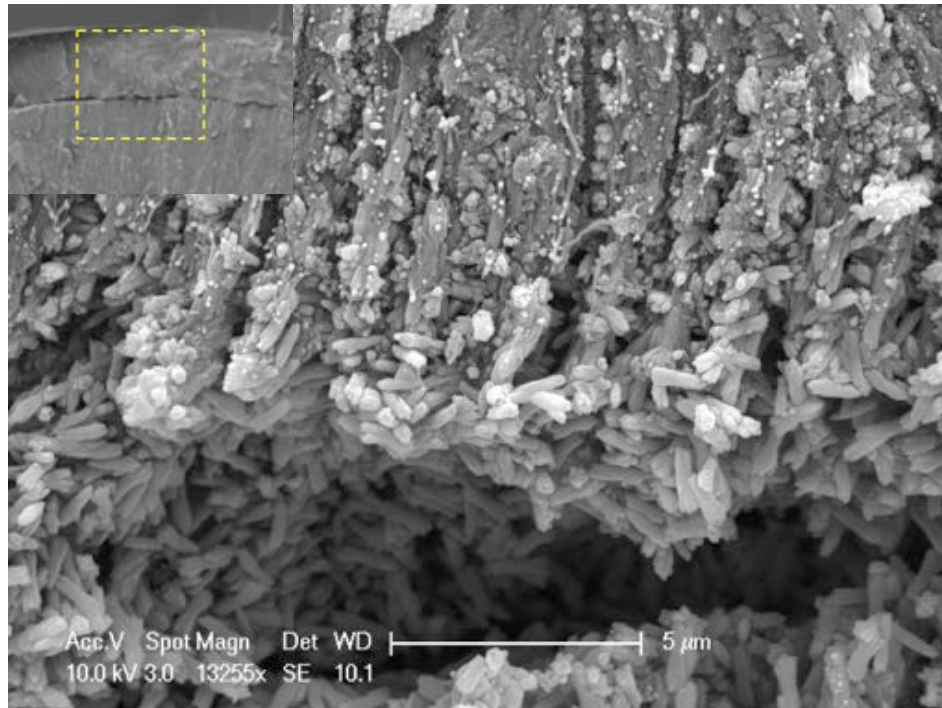


Figure 62.
Spherulitic particles
near the crack
surface not attached
to fibers are
misoriented.

Biomimetics:

Towards the end of year 1 and into year 2 of this project, we started to fabricate biomimetic panels that replicated the periodic region of the club.

We know that through evolutionary processes, biological composites have been optimized to fulfil specific functions. The dactyl club has been designed to withstand the thousands of high-velocity blows that it delivers to its prey. The endocuticle of this multiregional structure is characterized by a helicoidal arrangement of mineralized fiber layers, an architecture which results in impact resistance and energy absorbance. During this project, we applied the helicoidal design strategy observed in the stomatopod club to the fabrication of high-performance carbon fiber-epoxy composites. Using experimental and computational methods, a helicoidal architecture is shown to reduce through-thickness damage propagation in a composite panel during an impact event and result in a significant increase in toughness. These findings have implications not only for the design of composite parts for aerospace, but also automotive and armor applications. The following pages describes this work.

Owing to its design, a natural bio-inspired corollary to the Bouligand structure found in the periodic region can be achieved using fiber-reinforced composites. Unidirectional composite materials consist of aligned fiber layers, similar to those observed in the crustacean exoskeleton. Through the stacking of unidirectional layers (plies), a helicoidal composite can be readily obtained.

Here, we examined three helicoidal rotation angles, and compared results to unidirectional as well as quasi-isotropic (an aerospace industry standard design and a robust baseline architecture) controls. In this work, the impact damage to each sample was investigated through experimental

observations as well as finite element analysis. Following impact testing, the residual strength of the samples was determined through compression testing. This compression after impact protocol provides information on composite toughness, as it interrogates the ability of the sample to carry load following the onset of damage. Experimental and model results for fiber reinforced composites provide insight into toughening mechanisms at work in the stomatopod dactyl club, and reveal design guidelines for impact resistant materials.

Composite fabrication

The composite material used was a carbon fiber epoxy prepreg with a unidirectional reinforcement (HexTow[®] IM7, Hexcel, USA) specifically formulated for out-of-autoclave, vacuum bag only cure (CYCOM5320-1, Cytec Industries, USA). Five sets of composite panels, each measuring 350 mm long and 180 mm wide, were fabricated with 48 prepreg layers that were laid up with different ply orientations. Two sets of standard control composite panels were fabricated. The first was a unidirectional sample, with all plies oriented in the 0° direction. The second control were quasi-isotropic panels consisting of prepreg layers oriented in the 0°, ±45° and 90° directions, with the layup symmetric about the mid-plane. Mid-plane symmetry is critical in composite manufacturing, to prevent the warping that can occur in non-symmetric layups due to residual stresses that develop during elevated temperature cure. In addition to the unidirectional and quasi-isotropic controls, three helicoidal structures were fabricated with rotation angles of 7.8, 16.3, and 25.7 degrees. These rotation angles were chosen such that all panels had a consistent thickness, and mid-plane symmetry could be maintained. Details of the composite layup schemes are presented in Table I.

Table I. Layup details for composite laminates

Sample	Layup
Unidirectional	[0] ₄₈
Quasi-isotropic	[0/±45/90] _{6s}
Small angle	[0/7.8/.../180] _s
Medium angle	[0/16.3/.../180] _{2s}
Large angle	[0/25.7/.../180] _{3s}

For all helicoidal samples (schematic shown in Figure 63A), prepreg plies were cut to specific angles prior to layup. All samples were fabricated to be symmetric about the mid-plane, meaning each right-handed rotation was immediately followed by a left-handed rotation (fiber angle in each sample is represented by the grey scale images in Figure 63B).

After layup, samples were vacuum bagged (> 28" Hg) according to the layup schematic in Figure 63C. Bagged samples were debulked for 4 hours at room temperature to remove trapped air. After the room temperature vacuum hold, samples were cured according to the manufacturer's recommended cure cycle (Figure 63D). All samples were subjected to a freestanding post-cure cycle consisting of a ramp at 2° C/min to 121° C, immediately followed by a 0.6° C/min to 177° C. This lower ramp rate was employed to avoid crossing the instantaneous glass transition temperature of the resin and de-vitrifying the resin. The samples were held at 177° C for 2 hr. Samples were finally cooled back to room temperature at 2° C/min.

After curing, composite samples measuring 6.5 mm in thickness were machined to dimensions of 100×150 mm for mechanical testing. The dimensions of each sample were measured with calipers and recorded. Polished cross-sections of each sample were prepared by embedding in epoxy (SamlKwick, Buehler, USA) and polishing with graded silicon carbide sandpapers down to a grit of 1200 ($15 \mu\text{m}$). Cross-sectional microstructures were examined using a digital stereo microscope (Keyence VHX-600E).

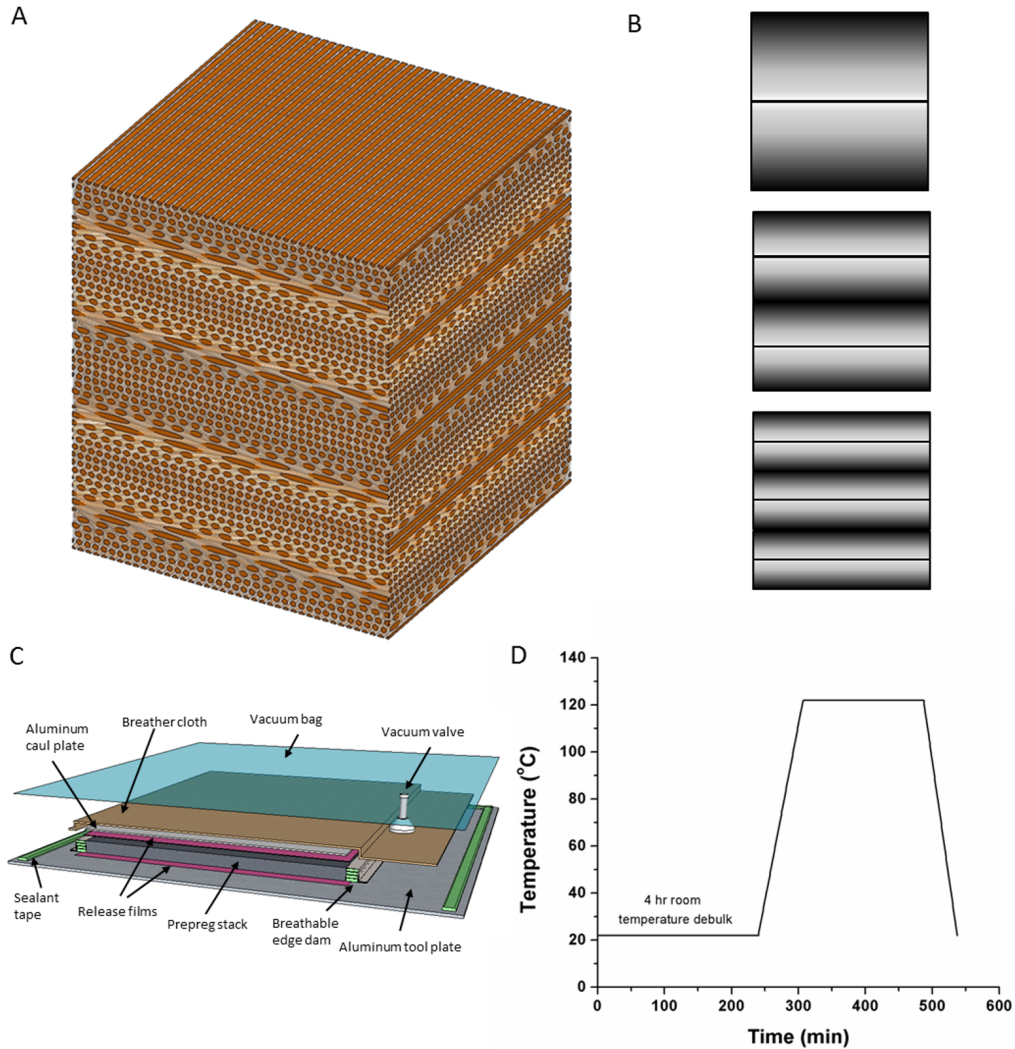


Figure 63. Details of composite processing. (A) Schematic representation of a helicoidal rotation of fiber layers (shown here for the medium angle composite). (B) Grey-scale images to represent fiber rotation angles in helicoidal composites, demonstrating the mid-plane symmetry achieved by following each right-handed rotation with a left-handed rotation. (C) Details of the composite layup and vacuum bagging scheme. (D) Composite cure cycle.

To determine the toughness of each composite, samples were subjected to a standard compression after impact testing protocol (ASTM D7136). Impact testing was performed using a drop weight impact testing system equipped with a hemispherical tip, with a diameter of 16 mm (9250HV, Instron, USA) and providing an impact energy of 100 J. During impact, samples were held in place by circular clamp, with 76 mm diameter holes at the center. After impact,

photographs of each sample were obtained to examine external damage, and dent depth was measured using a depth gauge. Internal damage was probed using a non-destructive ultrasound technique (Ultrasonic C-scans) using a 10 MHz water-coupled transducer in the reflected mode (UPK-T36, NDT Automation, USA). Following ultrasound analysis, samples were end-loaded into a specialized fixture and compressed to failure, following ASTM D7173. The fixture prevents global buckling of the sample during testing, leading to failure as a result of propagation of cracks and delaminations. A displacement controlled compressive loading of 1.25 mm/min was applied using a high-load load frame (5585H, Instron, USA). Load and displacement were recorded during testing and used to calculate residual strength.

The rotational angles examined in our biomimetic composites, 7.8, 16.3 and 25.7 degrees, were constrained by the need to maintain a consistent number of layers and impose mid-plane symmetry. These were, in most cases, larger than those calculated for the stomatopod club, with the smallest angle (7.8 degrees) providing a close match to the innermost region of the club. Despite the inability to directly measure or replicate the angles present in the club, the use of multiple angles provides a means of determining the influence of a small vs. large angle of rotation on material response.

The mechanical properties of helicoidal composites were compared to those of control layups (unidirectional, quasi-isotropic) to examine the influence of the rotated design on impact resistance. With mid-plane symmetry imposed, all samples remained flat after curing, and no warping was observed. Polished sections of each sample confirmed that panels were void-free. Microstructural analysis of each sample type (Figure 64) demonstrates a change in grey-scale intensity through the thickness the sample (with the exception of the unidirectional panel), which is caused by changes in fiber rotation angle. Samples were sectioned such that the 0° direction is perpendicular to the polished face.

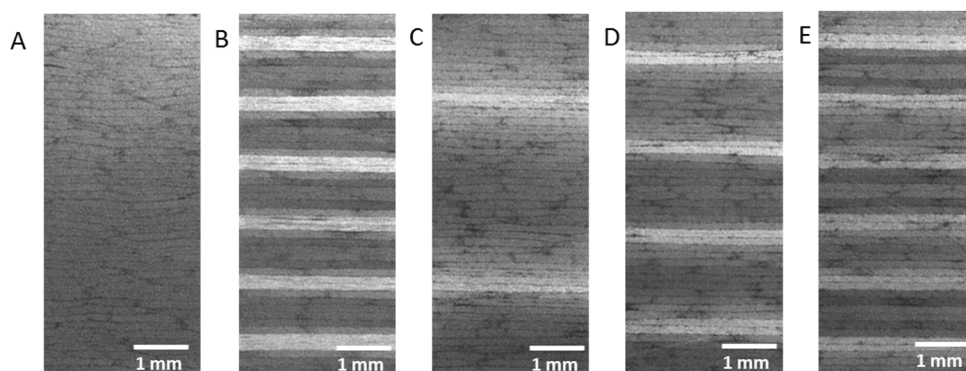


Figure 64. Micrographs of polished sections from the (A) unidirectional, (B) quasi-isotropic, (C) small angle, (D) medium angle, and (E) large angle composite panels.

Impact response

Samples measuring 100 × 150 mm were subjected to high-energy (100 J) impact using a drop tower. Following the impact event, the extent of damage to the panels was assessed. Three samples were tested for each layup condition, yielding consistent results. The images in Figure

65A - E are representative of the damage type for each layup. Initially, external damage was examined on the backside of the panel, opposite the impact event. The high-energy impact produced catastrophic failure in the unidirectional control samples, resulting in a splitting of the panels (Figure 65A). All other samples, however, showed varying degrees of impact damage. For the quasi-isotropic controls (Figure 65B), the impact event resulted in puncture through the backside of the panels, accompanied by fiber breakage. The helicoidal samples, in contrast, did not show indentation puncture, but rather splits on the back surface. It is of note that these splits did not, in all cases, occur immediately opposite to the impact location, but were rather displaced from the central impact point. For the small angle composite panels, large delamination cracks were observed along the long edge of the sample (Figure 65C).

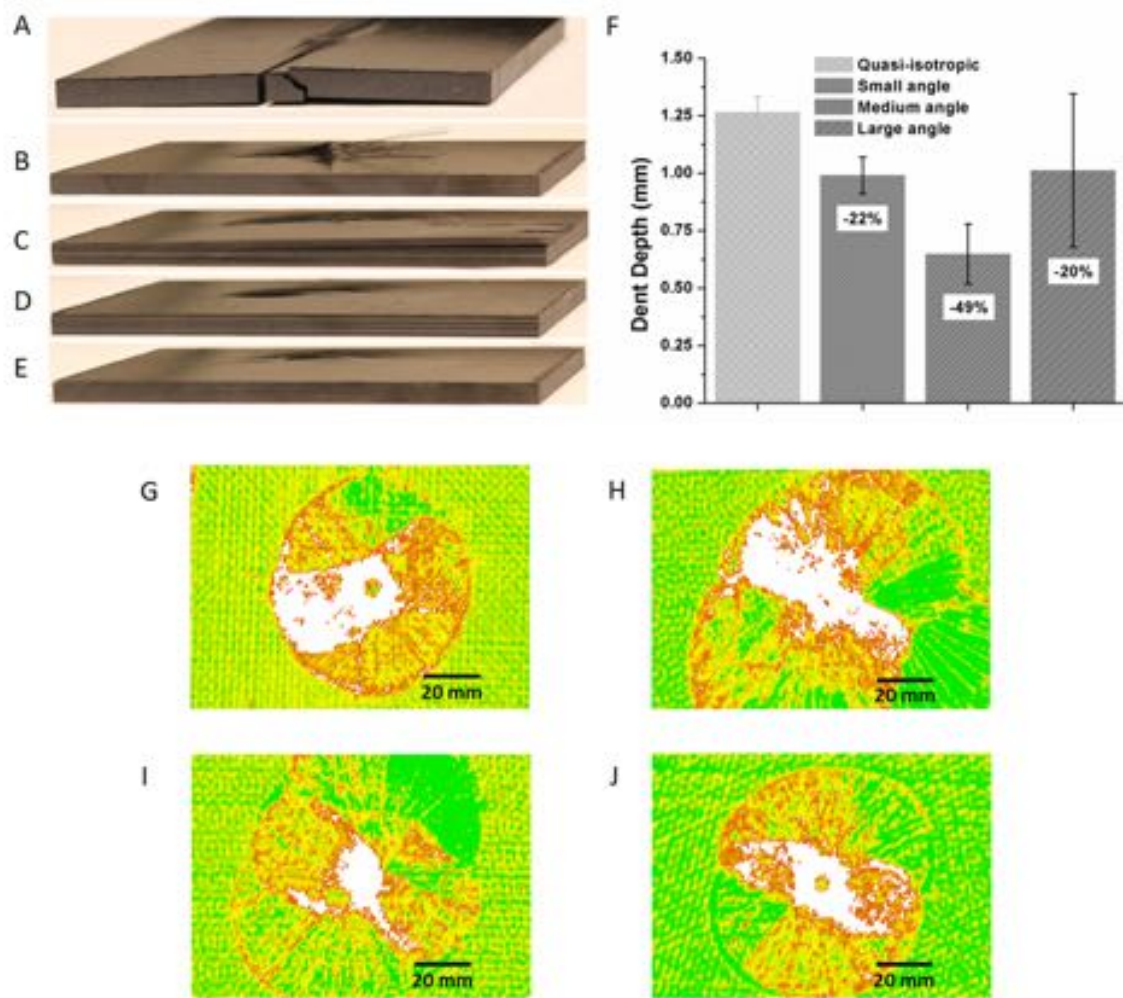


Figure 65. External impact damage. Photographs showing damage in the (A) unidirectional, (B) quasi-isotropic, (C) small angle, (D) medium angle, and (E) large angle composites. (F) Dent depth measurements for each sample. Percent reduction in dent depth listed for helicoidal samples. Ultrasonic C-scan images showing internal damage fields in the (G) quasi-isotropic, (H) small angle, (I) medium angle, and (J) large angle composites.

As a second indication of impact damage, the dent depth produced by the impact (on the impact side of the panel) was measured (Figure 65F). Because the unidirectional panels were split by the impact, it was not possible to measure dent depths for those panels. In all cases, the helicoidal samples showed a reduced dent depth when compared to the quasi-isotropic control. The percent reduction in depth is reported on the plot in Figure 65F. From dent depth measurements, the medium angle composite showed the greatest reduction in external indent damage, with a depth reduction of 49%.

The internal damage field caused by impact was interrogated using a non-destructive pulse-echo ultrasound technique. Scans were performed in a water tank using a 10 MHz transducer in the reflected mode. Representative ultrasonic C-scan images are presented in Figures 65G – I. The color scale on the images represents the reflected signal intensity, with green indicating a reflected intensity of approximately 90%, yellow 50%, and red 10%. White areas are empty pixels, resulting from regions where no signal was detected (indicating a high degree of internal damage). The ultrasound data reveals that the quasi-isotropic control sample (Figure 65G) has the smallest internal damage field. The damage spread in the control sample is also symmetric. The helicoidal samples, however, show a more wide-spread and asymmetric damage field. The extent of the lateral spread of damage is most pronounced in the small angle composites (Figure 65H), where splitting was observed on the sides of the sample (Figure 65C).

Residual strength

Following analysis of impact damage, samples were end-loaded and compressed to failure. This compression after impact test protocol is a composite industry standard test for toughness, as it interrogates the ability of the sample to support a load after the onset of damage. Load vs. displacement data was recorded for each panel type (Figure 66A). Compressive residual strength was calculated from the peak load achieved during the test (P_{max}) divided by the cross sectional area of the panel (A), as detailed in Equation 1.

$$F^{CAI} = \frac{P_{max}}{A} \quad (1)$$

Details of the residual strength in each panel are presented (Figure 66B) with the percent change in residual strength versus the quasi-isotropic control indicated for helicoidal samples. The small angle panels reached the lowest loads during compression and thus have the lowest residual strength. The medium and large angle panels, however, show a marked increase in residual strength when compared to the quasi-isotropic control (16 and 18%, respectively). After compressive failure, the damage behavior in each composite was assessed (Figure 66C - F). Dotted black lines mark the lateral extent of visible cracking. For the quasi-isotropic control (Figure 66C), the damage is localized to a narrow region directly in line with the impact event. However, the damage in the helicoidal samples is spread laterally to varying degrees. The small angle composites, which showed edge cracking following impact, exhibit damage across the entire length of the test specimen, and show considerable cracking (Figure 66D). In the medium angle composite, cracks are distributed laterally, with damage propagating farther outward in lower plies. The large angle composite shows the most narrow damage window for the helicoidal samples, though the damage is still more disbursed than in the case of the quasi-isotropic control.

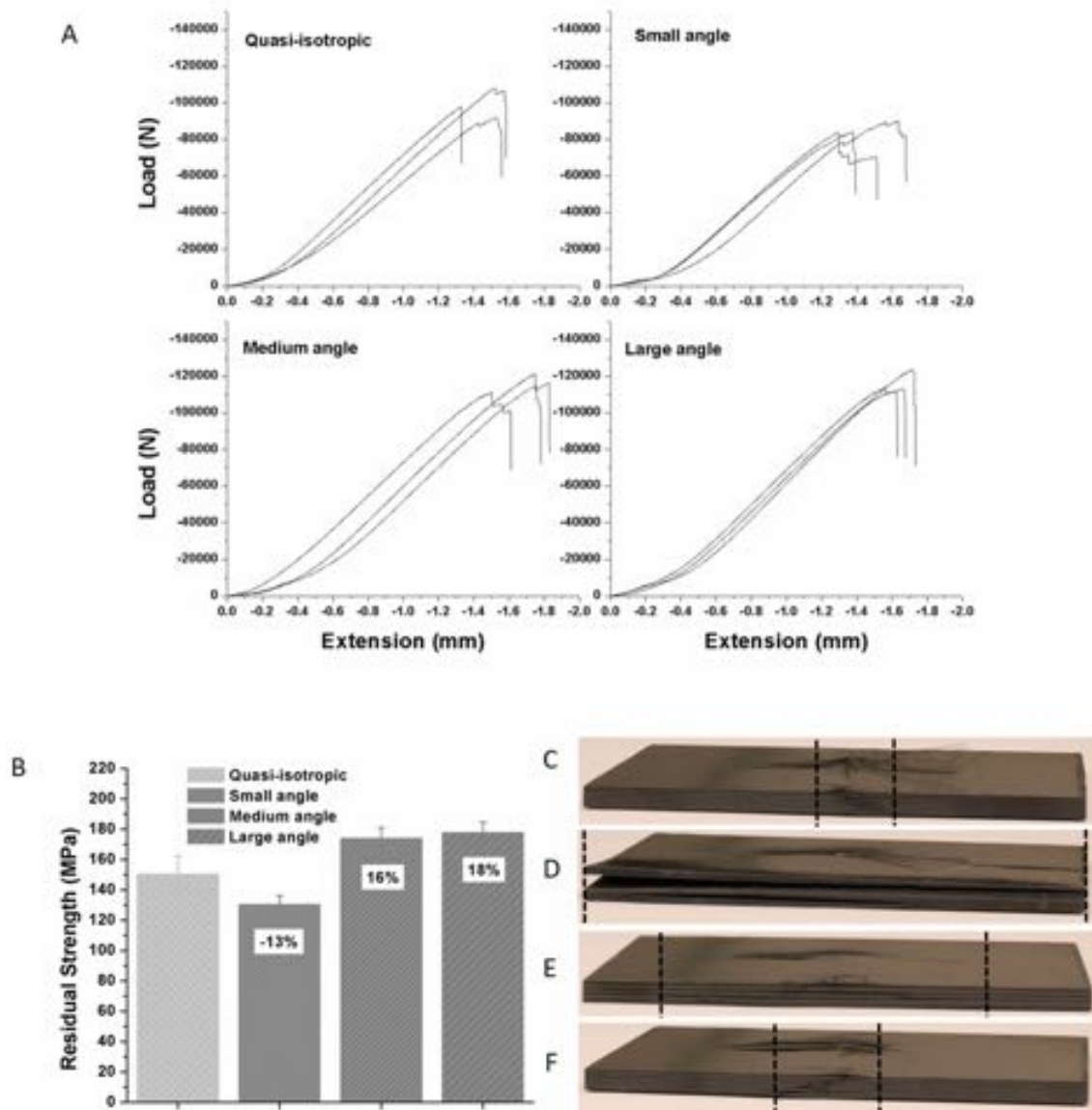


Figure 66. Composite residual strength and compressive damage. (A) Load-displacement curves from compression after impact testing. (B) Residual strength calculated from compressive data, with percent change listed for helicoidal samples. Photographs of damage in the (C) quasi-isotropic, (D) small angle, (E) medium angle, and (F) large angle composites after compression tests.

Modeling of Biomimetic Composites:

To obtain more information about the damage mechanisms at work in helicoidal composites, computational models were employed.

The computational modelling for drop tower test ASTM D7136 on the IM7/5320-1 composite specimens was performed by using dynamic finite element modelling to study and predict the failure mechanisms in the composite specimens under high impact loading circumstances. The

quasi-isotropic, and small-, medium-, and large-angle helicoidal composites with 48 plies were studied and each specimen were modelled by a shell-element layer with the thickness being equal to average laminate thickness (0.135 mm) and the average element size near the impact region is 0.08 mm. This layer contains 144 integration points with each adjacent 3 points representing an individual unidirectional ply with specified fiber orientation as showing in Figure 67. This modelling approach provides the capability of capturing the variations of damage and stress states in each ply based on the global and local behaviors in the whole model and the individual plies. The material was assumed to have transversely-isotropic elastic response until failure which is modelled by Hashin progressive failure criteria which has been extensively verified in the open literature.

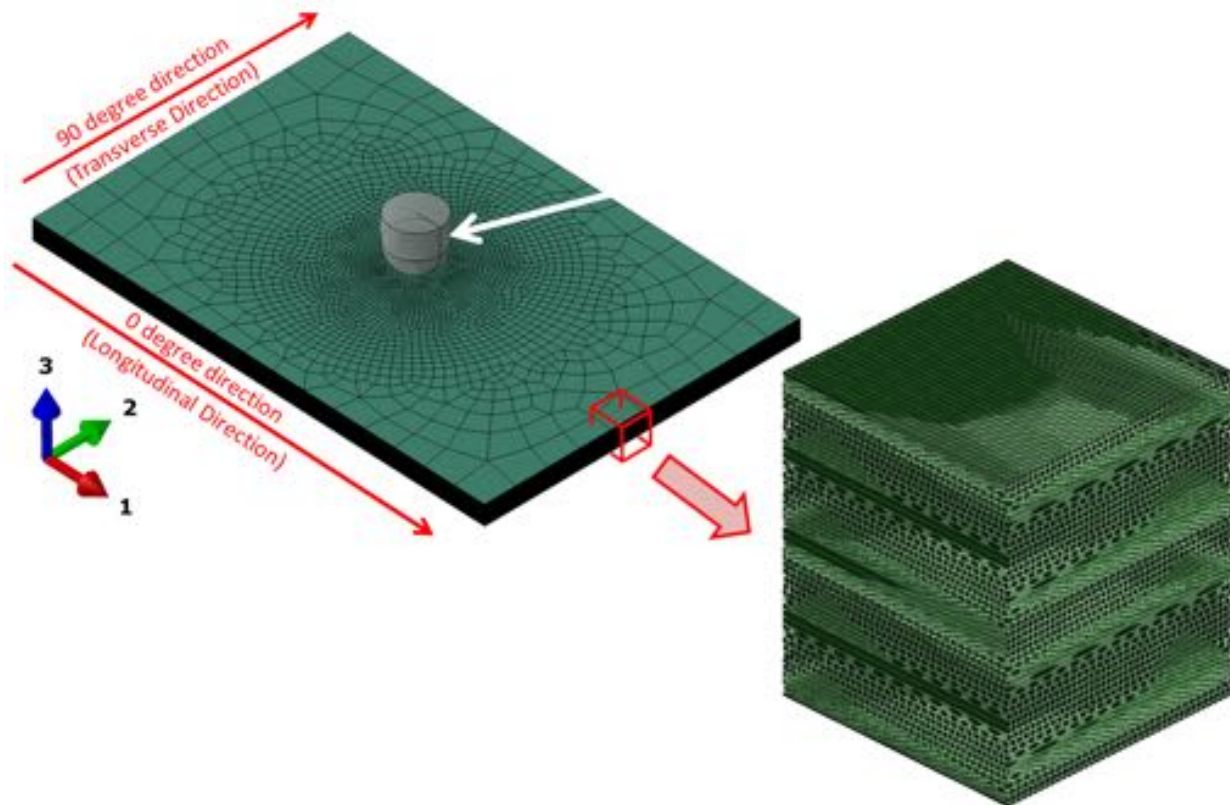


Figure 67. Finite-element model of a drop tower test and details of the helicoidal composite panel.

To effectively visualize the failure modes in the simulation results of the 3-D models, a visualization method has been implemented by displaying only the nodal points that meet Hashin failure criteria. This allows the visualization of the 3-D failure patterns in the interior of the sample. Figure 68 shows a qualitative description of the damage distribution in the interior of the plate at a representative time during the impact event. The dominant failure mechanism near the impact surface of the panel is observed to consist mainly of fiber compression (Figure 68), indicating that fibers near the impact surface undergo buckling and matrix damage. In the bottom section of the panel, the dominant failure mechanism is matrix cracking. This results from the bending mode of the central region of the panel during the impact process, which leads to tensile forces in the bottom section. Damage in the middle region is not significant, mainly because the stress values in the neutral plane are not high enough during the impact process. The model

results show a wide in-plane spread of damage in the small angle composites, which is reduced with a reduction in angle, and smallest in the quasi-isotropic controls.

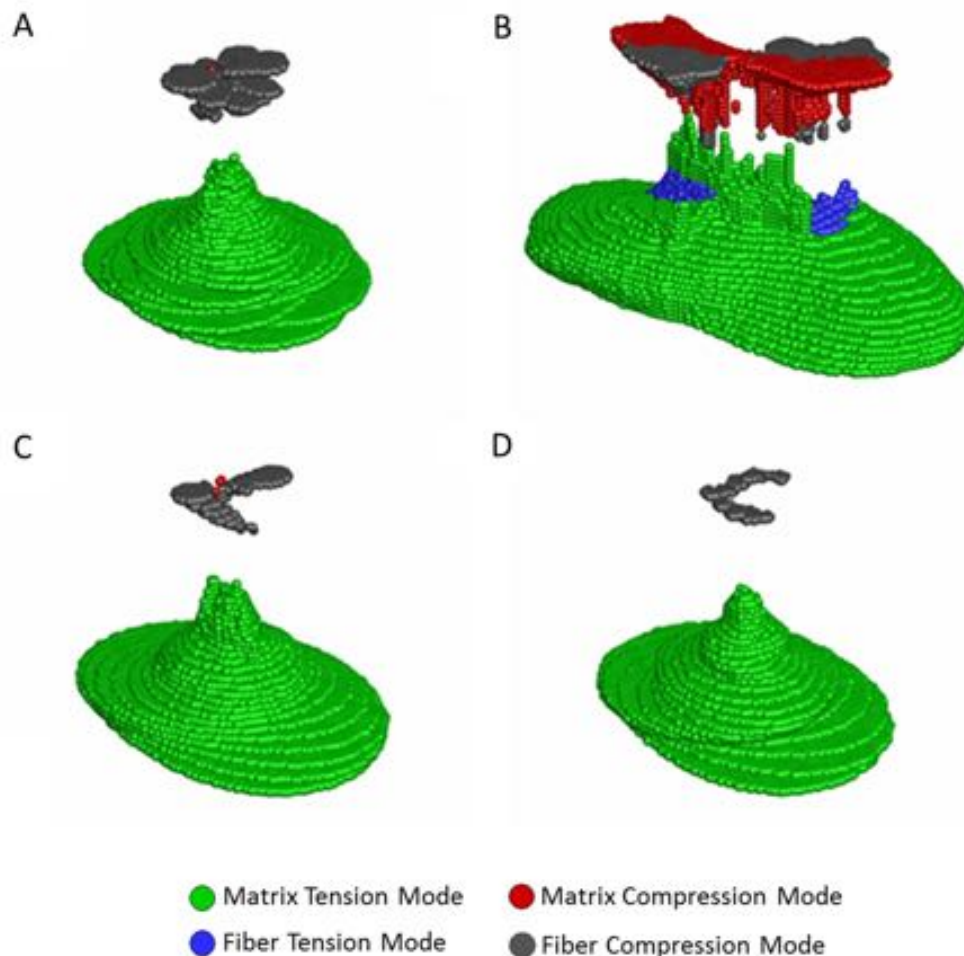


Figure 68. Damaged nodal points within the composite specimens based on Hashin failure criteria for the (A) quasi-isotropic control, (B) small-angle composite, (C) medium-angle composite and (D) large-angle composite. Color code indicates the dominant damage mechanisms. Each layer of colored points represents individual plies.

Thoughts on Biomimetic Helicoids:

The stomatopod dactyl club has evolved to withstand thousands of high-velocity impacts. The helicoidal architecture in the periodic region of this robust biological composite provides a means of dissipating energy from such high-velocity impact events. This is showcased in the nesting of cracks within the periodic region. This fracture pattern indicates that cracks follow the path of least resistance, propagating between mineralized fibers, rather than severing them. This results in a rotating crack front, which yields a large surface area per unit crack length in the direction of crack propagation. The Bouligand structure in the periodic region increases the toughness and energy absorption of the cuticle by redirecting cracks and preventing propagating of damage through to the surface of the club, thereby preventing catastrophic failure. This same

strategy is applied in this work to the production of impact-resistant high-performance composites.

In a fiber-reinforced structure, a helicoidal layup eliminates the large angle mismatch between adjacent layers. As elastic properties are a function of fiber angle, this graded design results in a smooth change in in-plane stiffness, reducing interlaminar shear stresses (a key source of delamination). This reduction in stress results in the ability to withstand greater deflections prior to the onset of delamination. The gradual rotation angle also leads to greater in-plane isotropy. Additionally, as is observed in the stomatopod club, a helicoidal organization of fibers results in a complex pattern of crack propagation. Here we have shown, through experimental results and computational models, that a helicoidal layup results in a wide in-plane spread of damage, accompanied by a non-symmetrical rotating damage field. Cracks in a carbon fiber epoxy composite will move preferentially through the matrix, rather than severing the stiff fibers. With a constant and gradual change in fiber angle in each layer, continuous matrix cracking is prevented and cracks are redirected in every ply, leading to a more tortuous crack path and thus greater energy dissipation. Through in-plane spreading of cracks and crack redirection, catastrophic propagation of damage through the thickness of the sample is prevented, leading to an impact-resistant structure.

Three helicoidal rotation angles were investigated in this work. Following a high-energy impact event, all three showed reduced damage in terms of dent depth and visible damage when compared to unidirectional and quasi-isotropic controls. Not surprisingly, the unidirectional composite failed catastrophically when subjected to impact. In a unidirectional sample, a crack can propagate through the entire thickness of the panel without the need to sever fibers. Thus, the unidirectional control was split down the center, with the crack running parallel to the aligned fiber layers. The quasi-isotropic control, with fibers oriented in multiple orientations, did not fail catastrophically. The impact event did, however, result in puncture through the back side of the panel, indicating that a high degree of damage was transferred through the thickness of the sample. Consistent with this hypothesis is the measurement of dent depth, which was highest for the quasi-isotropic control. In the helicoidal samples, dent depth was reduced, and no puncture was observed. This reduction in external damage is attributed to the in-plane spread of damage, observed in ultrasound C-scans.

Computational modeling was used to provide additional qualitative insight into crack behavior in helicoidal composites. Model results reveal that the tensile damage in the bottom of each sample is mainly dominated by matrix fracture (in green, Figure 68) without showing signs of fiber fracture. This is an indication that cracks are aligned to the fiber direction in the matrix of the bottom layers. While the quasi-isotropic model (Figure 68A) shows a distinct damage pattern in each layer, the helicoidal samples (Figure 68B-D) exhibit a smooth transition between consecutive layers. In other words, the helicoidal samples show a nonsymmetrical damage pattern that rotates from ply to ply. This smooth rotation does not necessarily follow the fiber rotation. However, we surmise that the initial damage and subsequent stress concentration in the bottom layer up is responsible for guiding the damage that occurs in upper layers. For example, if a crack in the matrix occurs in the 0 degree direction in the bottom layer (mostly following the direction of the fibers), the stress concentration will affect the directionality of the damage zone in the second and subsequent layers. Although the model is not capable of indicating the true

orientation of the cracks, it clearly shows the preferential orientation of the damage zone, and the dominant failure mode in each layer. The top layers of the helicoidal samples, near the impact surface, also exhibit different damage patterns when compared to the quasi-isotropic control. A smooth rotation between the compression damage is observed in the helicoidal samples.

Simulation results clearly show the highest degree of in-plane damage in the small angle helicoidal sample. This particular sample also shows extensive compressive damage in the matrix (which is not shown in the other samples). The extensive damage in the small angle simulation is consistent with experimental observations. Simulation results (Figure 69) are consistent with experimental C-scans of impact damage in (Figure 65G-J), validating the model results, and substantiating the fact that a smaller angle change provides wider in-plane damage dissipation.

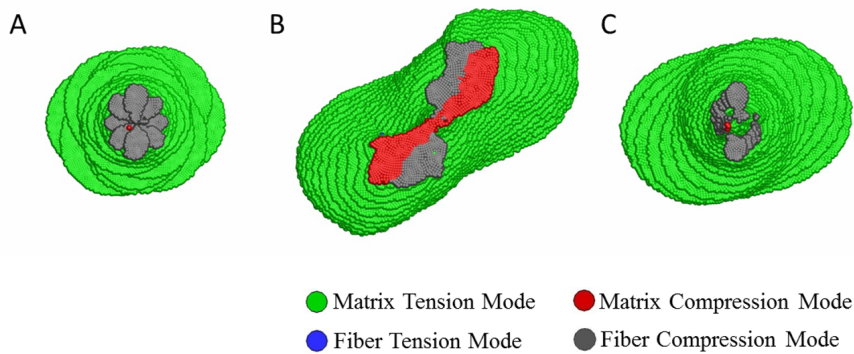


Figure 69. Model results (top view of damaged nodal points) compared with ultrasound C-scans for the (A) quasi-isotropic control (B) small angle composite (C) medium angle composite and (D) large angle composite. The zero degree direction runs left to right.

All helicoidal samples showed a reduction in external impact damage when compared to the control. However, the small angle composite showed the lowest reduction, which is likely a result of experimental factors, the most critical being sample dimensions. Observations of small angles samples following impact testing, as well as ultrasound C-scans, reveal that the in-plane spread of damage resulting from a ply rotation of 7.8 degrees is sufficient to reach the edges of a sample 100 mm in width. The damage, therefore, is not contained within the sample, but rather damage progresses to the edge of the panel, large-scale deformations occur, and the sample surface becomes uneven (Figure 65C). A flat surface is necessary to obtain accurate measurements using a depth gauge, and thus this damage mode influences experimental results. The ability to observe cracks at the edge of the sample, however, provides further insight into damage propagation. The cracks observed along the edges of the small angle composite are at an angle that is not parallel to the panel surface. This indicates that delamination is not the main failure mode, but rather that crack jumping is occurring between angled layers. Similar behavior has been reported in previous studies, as off-axis plies are more susceptible to matrix cracking than delamination.

After impact, the residual strength of the samples, or their ability to carry load following the onset of damage, was measured using an in-plane compression test. Residual strength is a critical measure of toughness in fiber reinforced composites. Composite panels are often damaged in service (for example bird strike in the aerospace industry), and detection of damage in composite structures is a difficult task. Therefore, it is essential that composite designs maintain strength after damage is initiated. The compression after impact testing of helicoidal composites revealed a marked increase in residual strength for the medium and large angle samples. Again, the performance of the small angle composite was adversely influenced by edge cracking. The observation of an increase in residual strength as a function of fiber angle is highly impactful. All samples examined in this study were fabricated with the same number of layers, using the same constituent materials. Introducing a helicoidal layup scheme, however, results in increased toughness and thus increased performance and structural safety.

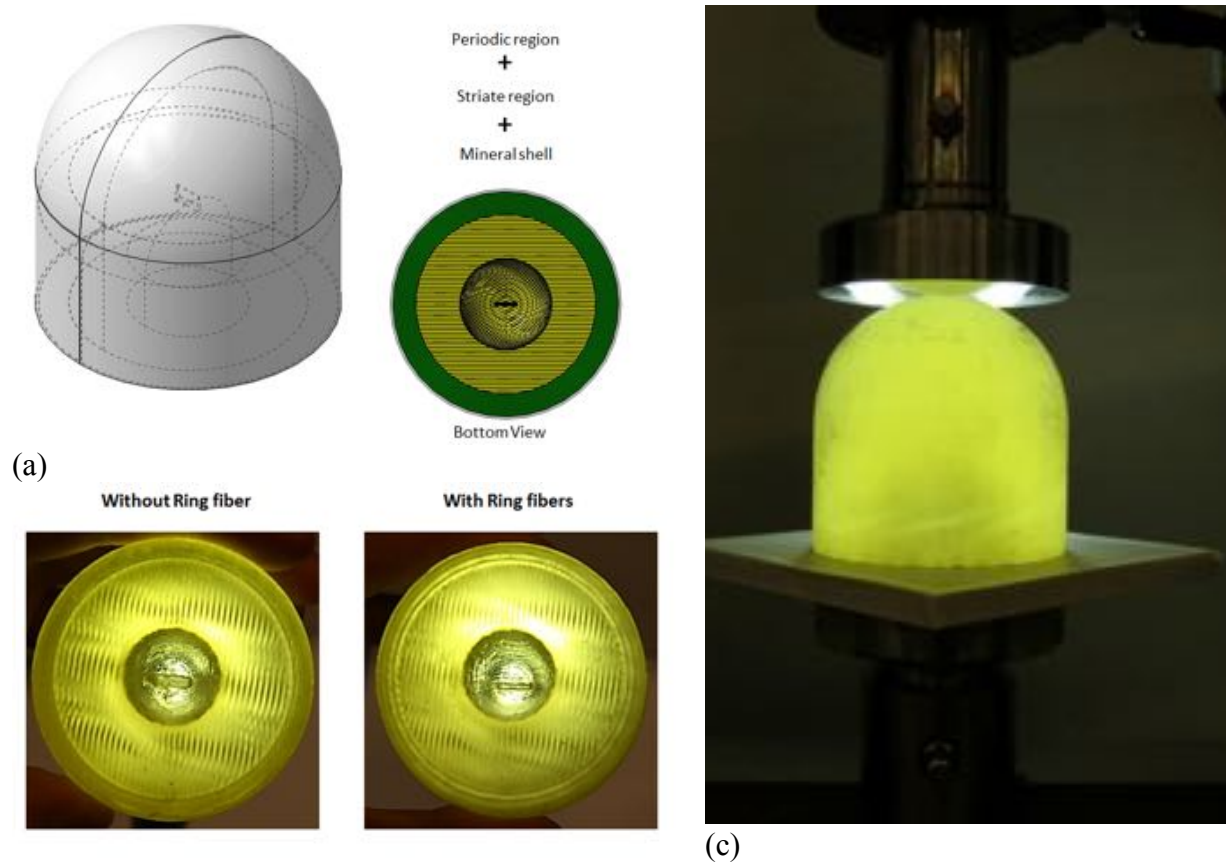
All plies for the carbon fiber epoxy samples fabricated in this work were measured, cut, and laid up by hand. This introduces the possibility of human error, specifically in the form of ply misalignment, which will directly influence sample performance. The potential for misalignment is greatest for smaller rotation angles, another factor which may have influenced the response of the small angle composite. While hand layup of complex laminate geometries is tedious and prone to error, helicoidal composites could be readily produced in industry using automated layup of unidirectional tapes, a common practice. Thus, the findings in this study are of practical importance for aerospace, automotive and armor applications, where impact resistance and weight savings are critical.

Through the examination of multiple helicoidal rotation angles, conclusions can be drawn regarding the influence of angle on material response. As mentioned, results for the small angle composite were influenced by experimental constraints. The medium and large angle data, however, reveal an increase in impact resistance for a smaller angle of rotation. These findings are of interest considering the structural arrangement of the stomatopod dactyl club. From SEM analysis, we hypothesize that the rotation angle in the club is smallest close to the impact surface. Therefore, we can expect optimum energy dissipation in the region most influenced by the high-energy strike. Additionally, a smaller rotation angle equates to a larger pitch length and a higher number of mineralized fiber layers. More fiber layers will result in increased crack redirection, as well as crack arrest, as cracks propagating through the mineral phase are known to stop when an organic fiber is encountered. This toughening mechanism also sheds light on the large pitch length observed in the club.

Prototypes of the dactyl club to study the striated region (year 2):

Preliminary observations have indicated that the role of the striated region of the Stomatopod's Dactyl club was mainly to provide restrained conditions for the periodic region. As the periodic region is mainly constituted by mineralized chitin fibers with relatively weak interfaces under mostly bi-axial tensile conditions, the striated region objective is to reduce the high stress/strain produced by the impact event on the periodic region and therefore minimize cracking. To evaluate this hypothesis we have designed and 3D printed a simplified model of the Dactyl Club as shown in Figure 70A. The three most important regions, impact region, periodic region and striated region have been considered. The periodic region is modeled as a Bouligand structure

and the striated region with ring fibers mimicking the actual fiber directionality observed in the striated region of the dactyl club (Weaver et al. 2012). Figure 70B and C show the 3D printing prototypes with and without ring fibers and the final experimental setup. Figure 71 shows the typical load-displacement curves showing the effect of the striated region.



(b) **Figure 70. (a) Design of the Dactyl Club prototype,(b) samples with and without striated region (c) Compression experiments.**

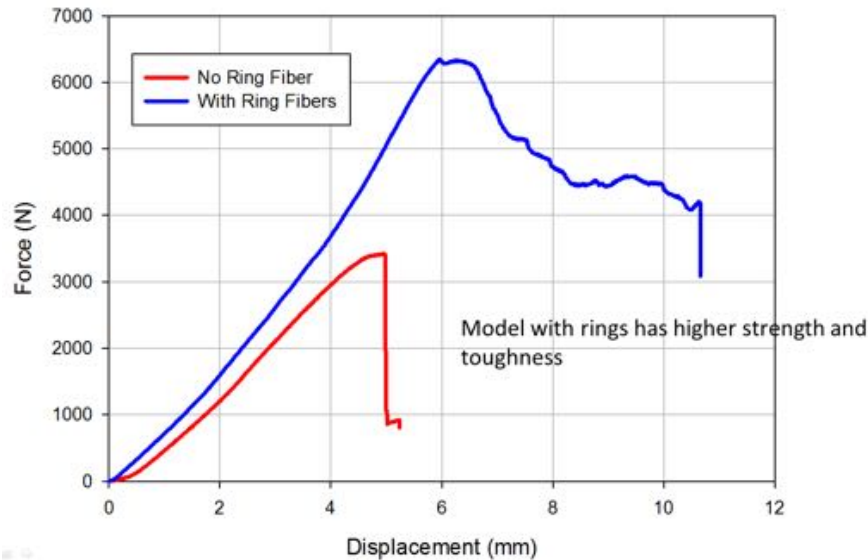


Figure 71. Force-displacement curves of the Dactyl Club prototypes comparing the cases with and without striated region rings.

Fracture Analysis on the Bouligand Structure in Stomatopod Dactyl Club under mode I Uniaxial Loading: Experimental: Year 2

In year 2, we used a 3D printer, Objet350 Connex, to fabricate the 3-point-bending beams of $29.7 \times 29.7 \times 178.2 \text{ mm}^3$ with the notch length of 9.9 mm. The composite structures within the beams are helicoidal fiber-reinforced composites with various pitch angles of 0° , 5° , 10° , 30° , and 45° pitch angles. Note that the pitch angle is the different angle between the orientations of the adjacent fiber layers. Additionally, 0° pitch angle sample is unidirectional fiber-reinforced composite. The diameter of fibers is 0.6 mm and the spacing between adjacent fibers is 0.5 mm. The 28 unidirectional fiber layers are stacked up from bottom to top of the beam. The notch tip always has fibers orientated at 0° where 0° and 90° orientations are aligned in the transversal and longitudinal direction of the beam, respectively. The CAD model of these samples are shown in Figure 72A with the front view showing in Figure 72B in which the fiber orientations are clearly displayed in all models. The 3D-printing prototypes of these samples are shown in Figure 72C where the fibers are made of VeroWhitePlus (RGD835) and the matrix is made of FullCure705. These samples are subjected to quasi-static three-point bending tests with the displacement rate of 0.2 mm/min and the results are showing in Figure 72D and the force – deflection responses are showing in Figure 73.

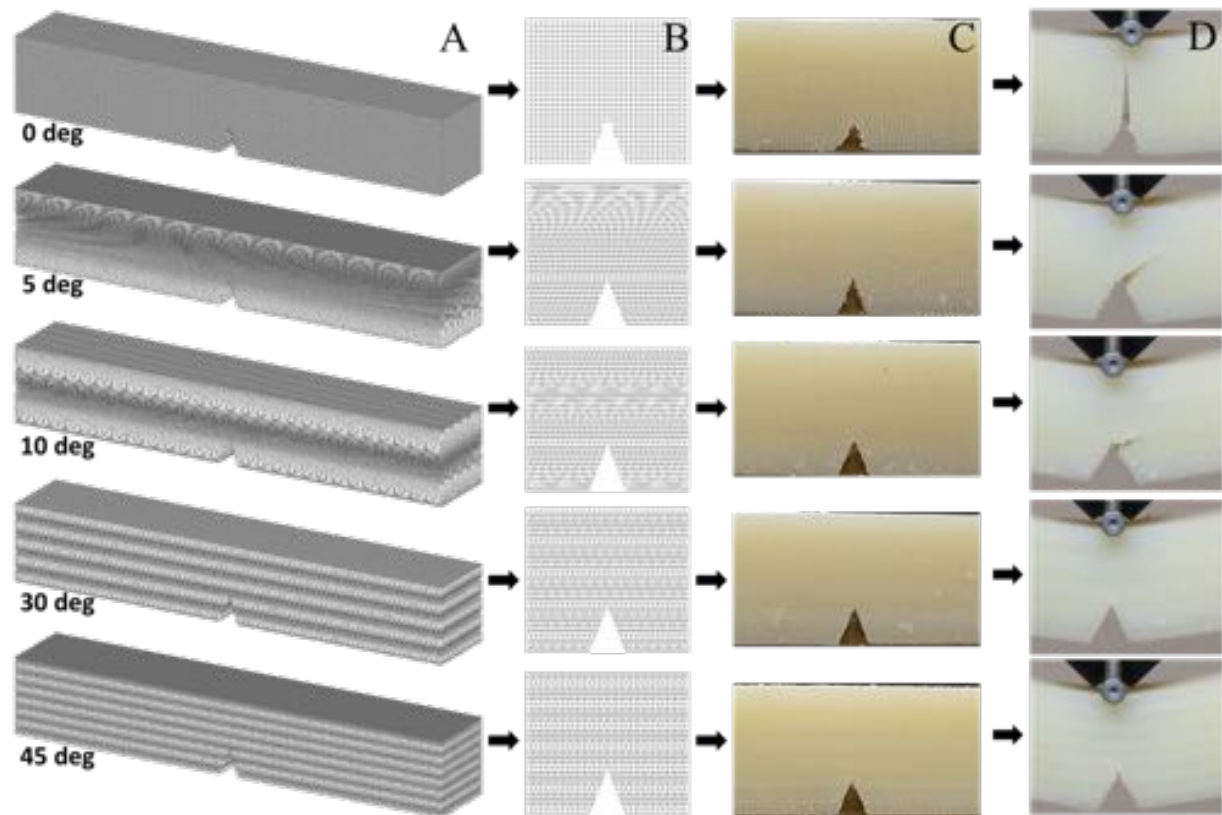


Figure 72. Fiber-reinforced composite models with 0°, 5°, 10°, 30°, and 45° - helicoidal structures from top to bottom, respectively. (A) CAD models. (B) Front view of CAD models. (C) Front view of 3D-printing prototypes. (D) 3-point-bending test results of 3D-printing composite samples.

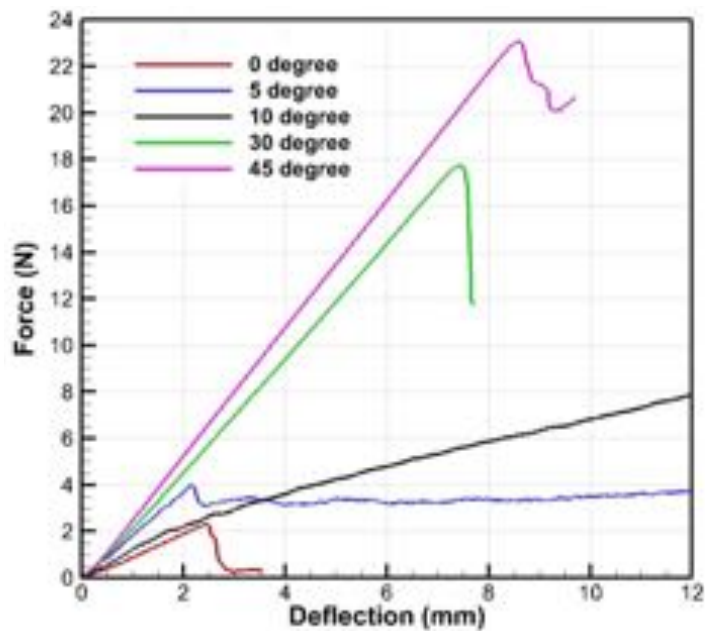


Figure 73. Force-deflection plots of 3-point-bending experiments on composite beams.

Figure 72D shows that the cracks have grown between fibers from the notch tip. The 0°-beam has shown straight crack with the softening behavior, i.e. force decreases after crack initiated and propagated as shown in red line in Figure 73. The 5°- and 10°-beams has the twisted cracks with the toughening behavior, i.e. higher force is required to propagate the twisted crack. In 30°- and 45°-beams, there is no crack visible at the notch tip. Instead, the failure in mode II delamination at a terminal part of the beams takes place and then the beams experience the total failure which is shown as a significant drop in force in Figure 73. Additionally, the difference in stiffness of the samples showing in Figure 73 is a result of the fiber orientation differences in the beams.

From these experiments, the toughening behavior has been seen when the twisted crack has propagated in the helicoidal composites. The further study on the twisted crack is subsequently carried out to get its insight by performing experiments on the solid beam with pre-defined crack path. The pre-defined crack path is designed as an 0.5mm-thick interface of FullCure705 (matrix material) being within the solid beam made of RGD835 (fiber material) with the dimensions defined in previous experiment. This design would force the crack to propagation into the certain directions and patterns. This would be called the pre-defined interface beam. In this work, the samples with straight planar interface (0°-pitch angle) and other 3 twisting interfaces of 5°-, 10°-, and 30°-pitch angles are studied. Note that the pitch angle in this part represents the rate of change in twisting angle over through-the-thickness distance. The CAD models are shown in Figure 73A and the 3D-printing prototypes are shown in Figure 73B.

The quasi-static 3-point bending tests are performed on all pre-defined interface samples and the results are shown in Figure 74 and the force-deflection behaviors are displayed in Figure 75. The results show that the cracks follow the pre-defined paths except 30°-pitch angle sample in which, instead, the crack grows into the solid material and causes failure to the beam as showing as the significant drop in force in small image in Figure 74. In 5°- and 10°-pitch angle beams, the crack also grow into the solid material but after it has propagated along the twisted interfaces for some period of time. While the crack is twisting, the toughening behavior is seen as showing in Fig. 8. Moreover, the increase of fracture strength has been observed in the twisted-crack beams, e.g., the red line in Figure 75 which represents 5°-pitch angle sample.

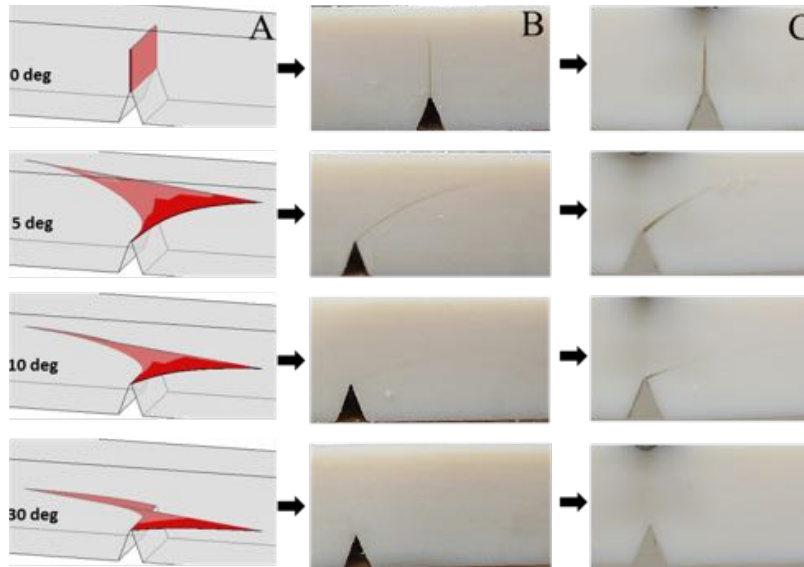


Figure 74. Solid beams with pre-defined interfaces which providing straight crack and twisting cracks of 5°, 10°, and 30° pitch angles from top to bottom, respectively. (A) CAD models. (B) 3D-printing prototypes. (C) 3-point-bending test results of 3D-printing composite samples.

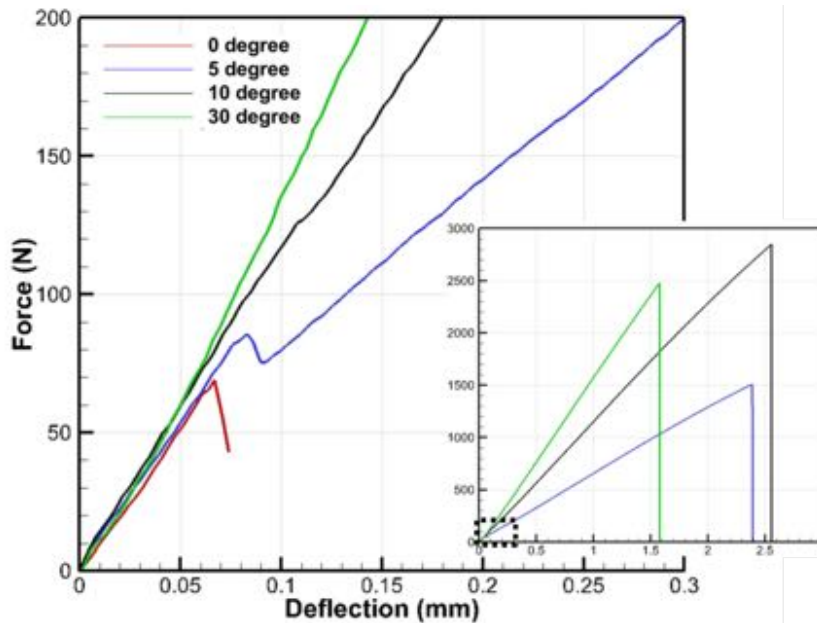


Figure 75. Force-deflection plots of 3-point-bending experiments on the pre-defined interface beams, small image on the right is the extent of the large image.

In the final year of this project, we utilized computational models to understand this crack behavior.

The twisted crack is further investigated by performing the computational modeling based on non-linear finite element analysis and cohesive zone model (CZM) on the pre-defined interface beams of 0°, 5°, 10°, and 30°-pitch angles. The cohesive properties in mode I and II of the

interfaces are characterized by 3-point bending tests of the straight interface beam and end-notch flexural tests, respectively. These give the mode I and II fracture strength $T_{m,I} = 0.82$ MPa, $T_{m,II} = 0.031$ MPa, mode I and II stiffness $k_I = 4 \times 10^{10}$ N/m, $k_{II} = 6 \times 10^8$ N/m, mode I and II fracture energy $G_{c,I} = 8.405$ Pa.m, $G_{c,II} = 0.805$ Pa.m. The Young's modulus (E) of RGD835 is 2 GPa and Poisson's ratio (ν) of 0.3.

The simulation results are showing in Figure 76 in which the normal stress in X-direction is displayed in the beams at the deflection of 0.15mm. Figure 77 is showing the comparison between simulations (solid lines) and experiments (dash lines). The simulations have confirmed that the toughening behaviors and the increase in fracture strength occur in the twisted crack samples.

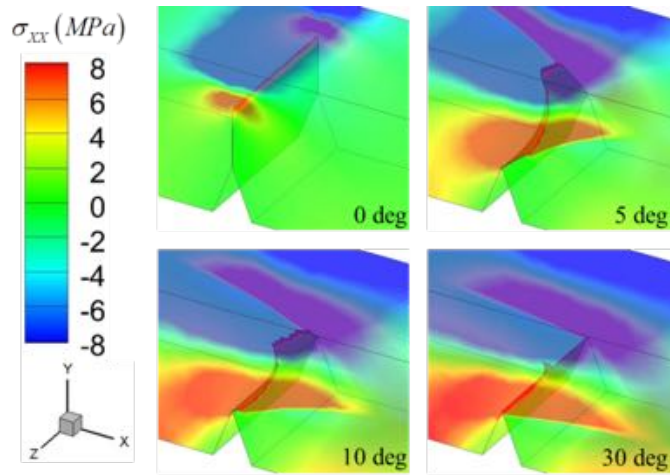


Figure 76. Normal stress in X-direction contour of simulation results of the pre-defined interface beams at deflection of 0.15mm.

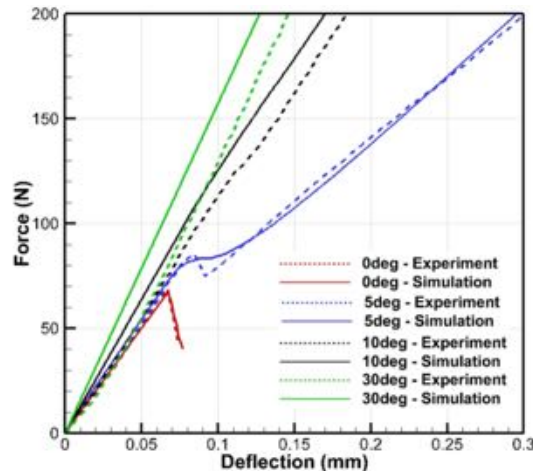


Figure 77. Force-deflection comparison between the results of simulations (solid lines) and experiments (dash lines) of the beams with pre-defined interfaces.

Theoretical Analysis

The continuous twisted crack occurred in the Bouligand structure in the dactyl club is represented as a twisted surface in which the surface is twisted by a twisted angle ϕ and is kinked by a kinked angle α . The mathematical representation of the twisting surface in case of the constant changing in ϕ over distance X ($d\phi/dX = \text{constant}$) can be written in the form of the following.

$$Y = Z \tan \left(X \frac{d\phi}{dX} \right) \quad (1)$$

The local coordinate systems of continuous twisted crack (x', y', z') are to be defined based on the theory of the level set method. This system of coordinate is established by the following three criteria. Firstly, one axis (y') is a unit normal vector of the twisted surface. Secondly, another axis (z') is a unit vector tangent to the crack front. Finally, the last axis (x') is obtained from the cross product of the above axes which designates the crack propagation direction. With these conditions, every single location on the twisted surface would have different local coordinate systems which satisfy our need to analyze continuous twisted crack. The local and global coordinate systems are related by ϕ and effective kinked angle (α^*) as illustrated in Figure 78

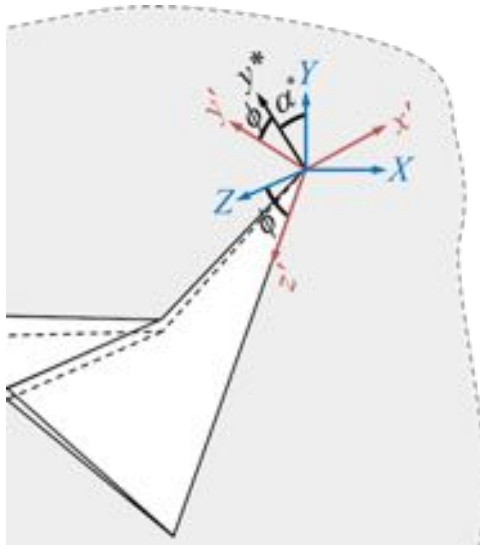


Figure 78. Relation between global (X, Y, Z) and local (x', y', z') coordinate systems at a position on the twisted crack front where y^* is on XY -plane.

Now, by knowing the relation between local and global systems of coordinate, it is found that the local stress field at $\theta' = 0$ at twisted crack front is equivalent to global stress field at $\Theta = \alpha^*$ rotated around X -axis by ϕ . Consequently, the local stress intensity factors (k'_I, k'_{II}, k'_{III}) at the twisted crack front can be expressed as a function global stress intensity factors (K_I, K_{II}, K_{III}). With condition of applying only the uniaxial mode I loading (K_I), the new analytical solution can be written in the form of:

$$\begin{aligned}
k'_I &= \left\{ \cos\left(\frac{\alpha^*}{2}\right) \left[\cos^2\left(\frac{\alpha^*}{2}\right) \cos^2 \phi + 2\nu \sin^2 \phi \right] \right\} K_I \\
k'_{II} &= \left\{ \sin\left(\frac{\alpha^*}{2}\right) \cos^2\left(\frac{\alpha^*}{2}\right) \cos \phi \right\} K_I \\
k'_{III} &= \left\{ \cos\left(\frac{\alpha^*}{2}\right) \sin \phi \cos \phi \left[\cos^2\left(\frac{\alpha^*}{2}\right) - 2\nu \right] \right\} K_I
\end{aligned} \tag{2}$$

Where ν is Poisson's Ratio. The new analytical solution in (2) is normalized by K_I and is then plotted against ϕ and α^* in Figure 79A in which k'_I is dropped and k'_{II} , k'_{III} is presented as ϕ and α^* increase. Moreover, the local energy release rate at the twisted crack front (g) normalized by global energy release rate (G) can be determined from (k'_I , k'_{II} , k'_{III}) as:

$$\frac{g}{G} = \left(\frac{k'_I}{K_I} \right)^2 + \left(\frac{k'_{II}}{K_I} \right)^2 + \frac{1}{(1-\nu)} \left(\frac{k'_{III}}{K_I} \right)^2 \tag{3}$$

The plot of normalized g against ϕ and α^* is displayed in Figure 79B which shows that g is decreased with the increase in the magnitude of ϕ and α^* . This means that the twisted crack front would require higher applied loading to be able to grow the twisted crack. This explains the toughening behavior which has previously been observed in the experiments and simulations.

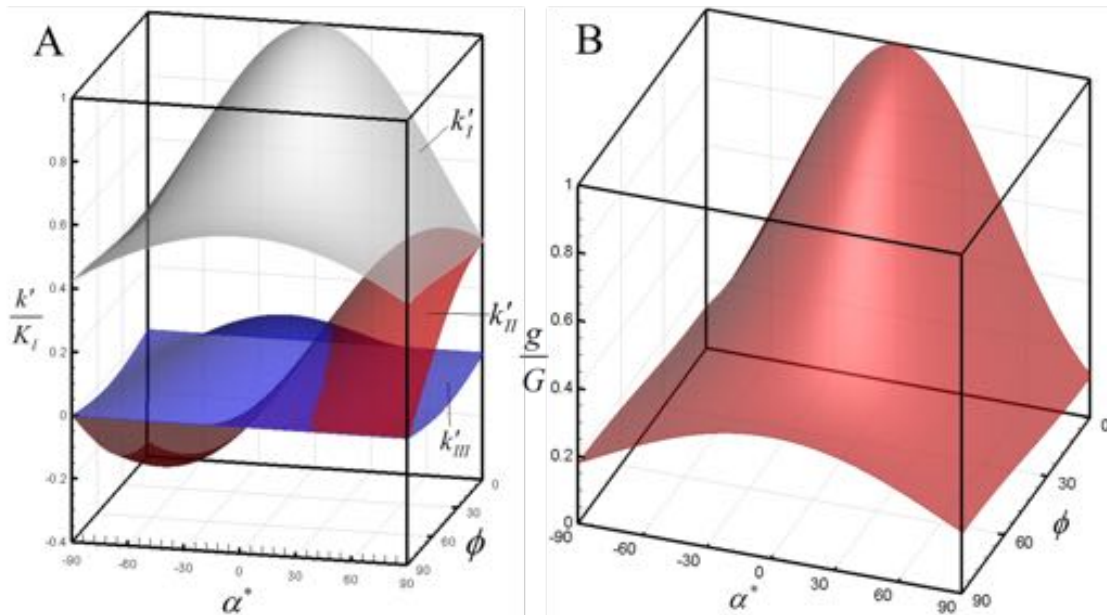


Figure 79. Surface plots of (A) normalized k'_I , k'_{II} , k'_{III} under remote K_I field determined by solution in (2) and (B) normalized g determined by (3) against α^* and ϕ .

The numerical simulations based on finite element method are performed to verify the new analytical solution developed in this work. The K -controlled analysis is chosen to simulate asymptotic stress field around the crack tip. This concept can simplify the LEFM problem and reduce its simulation expense when K is known. Then the J -integral method is used to determine g from K -field simulations.

In K -field analysis, the disc of 1m-radius (R_0) and 0.1m-thickness (t) with twisted crack as showing in Figure 80. The side surfaces of the disc are subjected to plane strain condition to eliminate the effect of finite-thickness. The circumference of the disc is subjected to the displacement field as a result of applied K_I which can be expressed based on LEFM as:

$$\begin{aligned} u_x &= \frac{2(1+\nu)}{E} K_I \sqrt{\frac{R_0}{2\pi}} \cos \frac{\theta}{2} \left(1 - 2\nu + \sin^2 \frac{\theta}{2} \right) \\ u_y &= \frac{2(1+\nu)}{E} K_I \sqrt{\frac{R_0}{2\pi}} \sin \frac{\theta}{2} \left(2 - 2\nu - \cos^2 \frac{\theta}{2} \right) \end{aligned} \quad (4)$$

The displacement field in (4) is theoretically derived based on the LEFM in the case of straight crack and crack tip locating at the center. Nevertheless, it can be applied to this twisted crack model with the assumption that the twisted crack is so small compared with the disc that it looks flat in the macroscopic level and, additionally, it locates close to center of the disc.

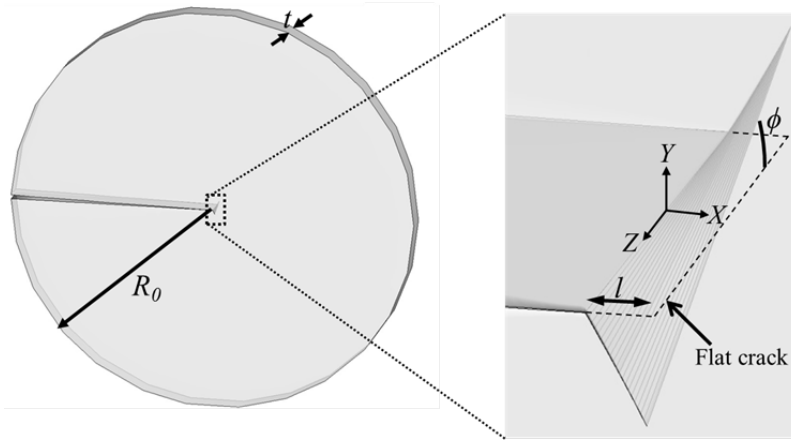


Figure 80. 3D-disc with twisted crack for K -field simulations showing dimension parameters and global coordinate system.

The model showing in Figure 76 is discretized into 754167 nodes and 739200 hexahedral elements with the smallest elements being approximately 0.1mm at the twisted crack. The total length of the twisted crack propagation along X -direction relative to disc radius (l/R_0) is 0.01 with $d\phi/dX=2^\circ/\text{mm}$. The crack propagation in the K -controlled analysis follows an approach proposed by Zavattieri.

The K -controlled analyses of the discs with twisted crack are simulated and g at their crack fronts are extracted by J -integral from the simulation results. All of these g are normalized by G and are

plotted against the positions of the crack in X and Z coordinates and then are compared with the results from the analytical solution in Figure 81 where the light gray and dark gray represent the J -integral and the analytical solution, respectively. Note that the results are shown only in the small region near the center of the disc in which the initial assumptions (crack looking flat and being near center) are satisfied. The comparison has shown that the g/G from J -integral match those of the analytical solution very well which indicates the validity of the new analytical solution developed in this study.

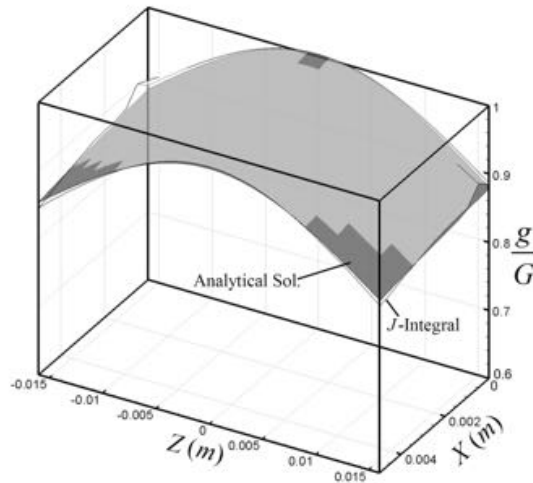


Figure 81. Surface plots of g/G over small area near the center of the disc where light and dark gray surfaces represent results from the simulations and the analytical solution, respectively.

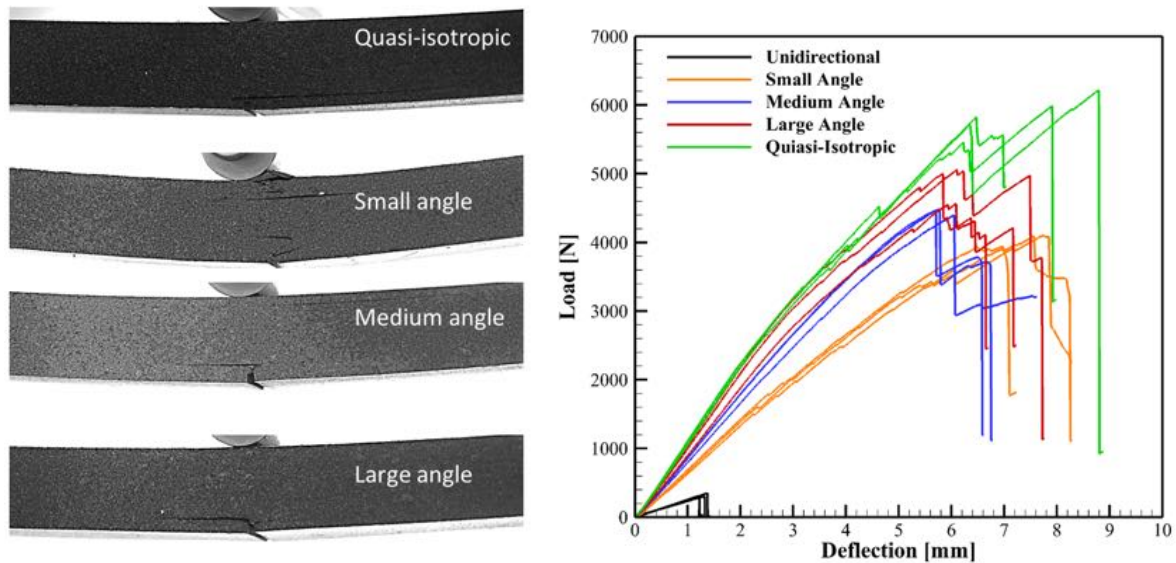


Figure 82. (a) 3 point bending tests showing crack twisting for the 4 type of composite layout tested in our preliminary investigation (b) Load displacement curves.

In the final year, 3D printed composites were made that replicated experiments done using carbon fiber.

The first set of results indicated that crack twisting is observed (See Figure 82), and improvement in toughening is seen in the load-displacement curves (Figure 82B). While we are currently post-processing this data (e.g., we are using DIC and modeling to interpret these results), these preliminary results seem to indicate that indeed we observe similar mechanisms as those observed in the carbon fiber mimics.

Thoughts on models:

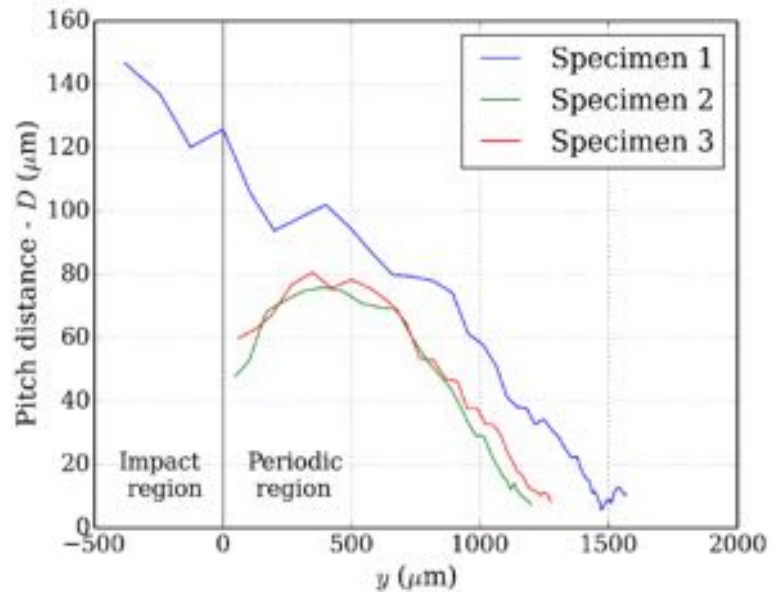
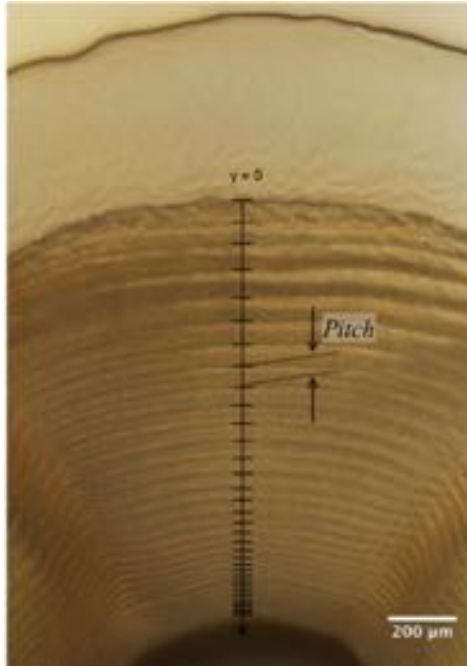
3 main aspects of fracture mechanics have been conveyed to study the Bouligand structure and twisted crack in the stomatopod dactyl club. In experimental works, the quasi-static 3-point-bending tests are performed on the bio-inspired Bouligand-structure composite and predefined-interface samples which are fabricated by 3D-printing prototype. The results from both sets of experiments have shown that the twisted crack is found in the helicoidal composites and the toughening behavior is seen when the crack is twisting. The computational models on the predefined interface experiments are simulated by Finite Element Analysis together with Cohesive Zone Model to further study the twisted crack. The computational results have confirmed the toughening behavior while the twisted crack is propagating. The insight of the mechanism of the twisted crack is uncovered in the theoretical study based on Linear Elastic Fracture Mechanics (LEFM) in which a new analytical solution to local stress intensity factors at the crack front has been developed specifically for the twisted crack occurred in Bouligand structure in stomatopod dactyl club (continuous twisted crack). Additionally, the J -integral is used in the K -field simulations to verify the new solution. The study based on these 3 aspects under uniaxial mode I loading has shown that the crack twisting in the Bouligand structure helps dissipating the energy which results in the toughening effects. The new analytical solution explains such mechanism as a result of the fracture mode changing at the twisted crack front. In summary, the study in 3 aspects of fracture mechanics under applied mode I loading has shown that the Bouligand structure would have the twisted crack and, consequently, the toughening behavior. The toughening mechanism is explained through LEFM that it is a result of fracture mode change at the crack front.

Shear wave filtering in the Bouligand structure:

In the final year of this project, we investigated wave propagation in the Bouligand-like structure from within the dactyl club of the Stomatopod. We incorporate the layered nature in a unitary material cell through the propagator matrix formalism while the periodic nature of the material is considered via Bloch boundary conditions as applied in the theory of solid state physics. Our results show that these materials exhibit bandgaps at frequencies related to the stress pulse generated by the impact of the dactyl club to its prey, and therefore exhibiting wave filtering in addition to the already known mechanisms of macroscopic isotropic behavior and toughness.

To properly analyze the characteristic length scales of the problem, i.e., the wavelength and internal microstructural characteristic dimension, we take information from the dynamic impact event and compare it to the geometric features identified in the periodic region. The optical

micrograph in Figure 83A depicts a transverse cross section of the periodic and impact regions of the dactyl club. Each line corresponds to a complete a 180° -rotation of the fibers. The distance between lines, also called pitch distance, D , is plotted in Figure 83B along the y -direction (where $y = 0$ is the interface between the impact and periodic region) for three different specimens. As it can be observed, both impact and periodic region display a pitch distance gradient varying from $140\mu\text{m}$ in the impact region to less than $10\mu\text{m}$ in the bottom of the periodic region. In some cases, a local maximum in the periodic region near the interface with the impact region is observed. However, even if the values of D have some slight variation with specimen, they show the same trend.



(a) (b)
Figure 83. Pitch gradient in the periodic region. a) Optical micrograph. b) Pitch distance in the periodic region.

The impact event can be represented in terms of a stress pulse, with a duration that ranges from $\Delta t \approx 1.4 \times 10^{-2} \text{ ms}$ to $\Delta t \approx 1.6 \times 10^{-1} \text{ ms}$. In this work, we employ the shortest duration, which translates into signal rich in high frequency content. In order to represent an extreme scenario, we also assume a square shaped pulse based on the fact that the use of a time discontinuity in stress requires more high frequency terms than in the real impact event. Figures 84A and B describe time and frequency domain comparisons between our theoretical square pulse and the impact measurement.

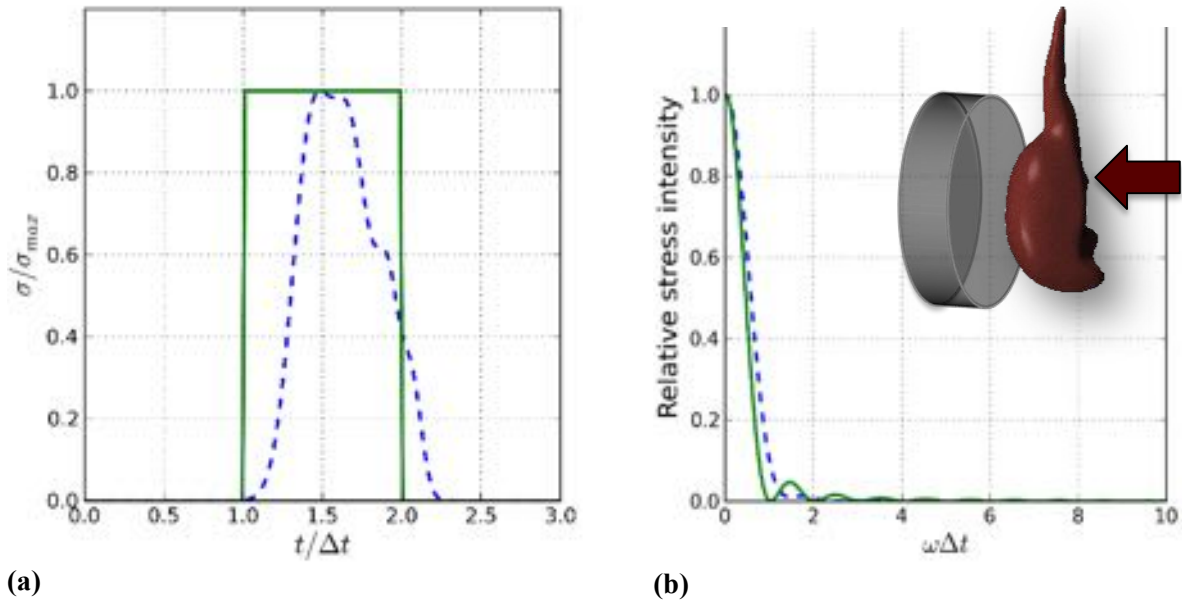


Figure 84. a) Impact pulse from the stomatopod's dactyl club strike on a flat target b) power spectra. The dashed line represents the waveform for the pulse simulated Weaver et al. [2012]. The solid line represents a square pulse that represents higher high-frequency content. Inset: schematics of the dactyl club impacting a target.

A material element cell is represented by an arrangement of N stacked layers of unidirectional fibers embedded in a matrix of thickness d and a pitch distance D . Such material element cell represents the behavior of the bulk Bouligand structure inside the dactyl club. As such, our main assumptions are: (1) the radius of curvature of the layers is much larger than D , and (2) there are enough layers to ignore boundary effects from the impact region or the inner portion of the dactyl club. Figure 85 shows the material element cell in the form of N helicoidally stacked layers of fibers representative of the periodic region of the dactyl club are accounted in the elastic behavior of a homogeneous transversely isotropic layer.

To assess the potential ability of the stomatopod to tolerate the high intensity impact pulse produced upon its daily hunting activity, we now obtain the fraction or amount of energy contained in a single pulse that is actually transmitted by the different microstructural configurations. This is achieved after computing the difference between the total strain energy density imparted by a typical stress pulse and the amount of energy lying inside a band gap bounded by frequencies $\omega_1 - \omega_2$ and associated to a specific microstructural configuration. This transmitted energy, shown as the shaded area in the schematic representation of Figure 85B, is given as

$$E_{trans} = \frac{2}{Y} \left[\int_0^{\omega_1} |\sigma(\omega)|^2 d\omega + \int_{\omega_2}^{\infty} |\sigma(\omega)|^2 d\omega \right]$$

where Y is a conveniently selected elastic moduli of the material which has been introduced for dimensional consistency.

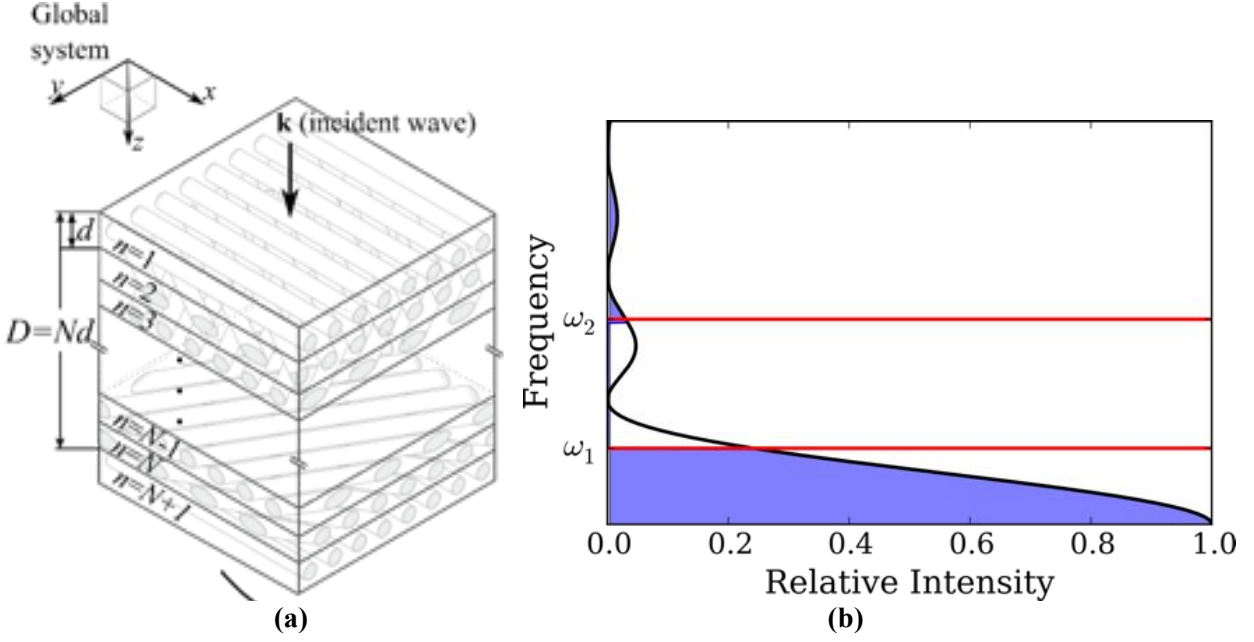


Figure 85. (a) Schematic of the layered model. The parameter, D is the pitch distance (i.e., the distance to make a rotation of 180°); d is the layer thickness; N is the number of layers in each pitch; and α_n is the angle for the n th layer, i.e., $\alpha_n = (n-1) \alpha$. (right). (b) Regions for passing and no-passing energy. The passing energy is computed as the shaded region over all the area under the curve. The band gap is denoted by frequencies $\omega_1 - \omega_2$ denoted by the horizontal (red) lines.

The performance of the different micro-structural configurations is compared on the basis of the fraction of transmitted energy η (or ratio between the transmitted energy and the total energy imparted by a single pulse. E_{total}), defined as:

$$\eta = \frac{E_{\text{trans}}}{E_{\text{total}}}$$

Figure 86 compares the performance of the resulting microstructures from different perspectives. Here, we introduce two dimensionless frequencies, $\Omega = Df/(2\pi c) = D/\lambda$ and $\theta = d\omega/(2\pi c) = d/\lambda$ which define ratios between the relevant microstructural lengths and the wavelength of the propagating wave.

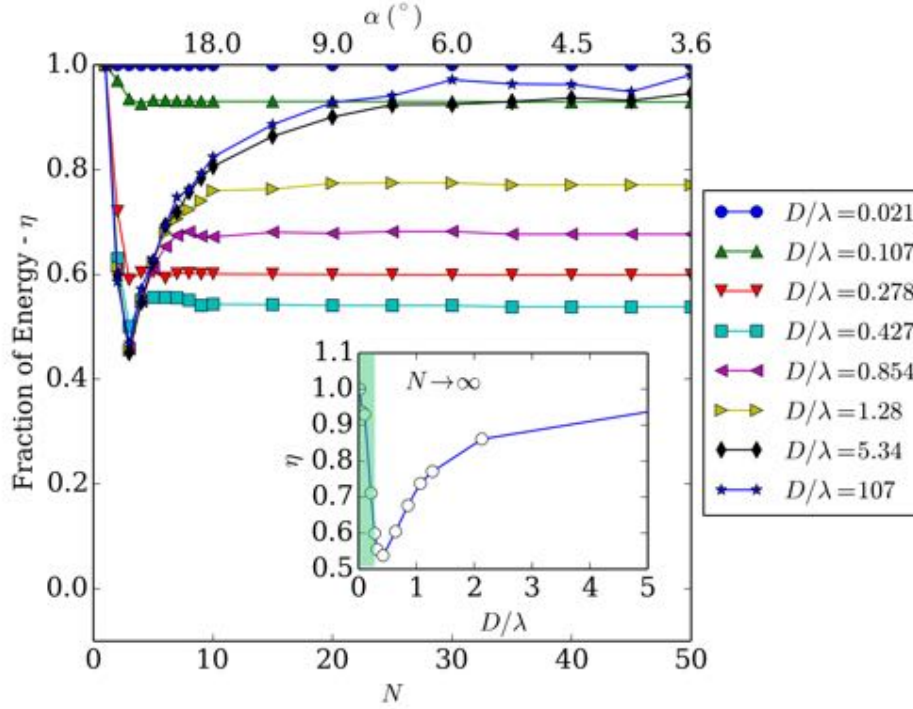


Figure 86. Fraction of transmitted energy, η vs. N for various values of D/λ . The inset plot shows η for $N \rightarrow \infty$. For comparison purposes the range of the stomatopod microstructure is indicated by the shaded area.

Summary of shear wave filtering work:

Using the model of a periodic Bouligand-like structure identified by Weaver et al. [7] in the Stomatopod's dactyl club, we have conducted a study intended to elucidate some of the physical mechanisms responsible for the amazing capabilities of the stomatopods dactyl clubs to sustain high intensity dynamical impacts assuming that the material remains elastic during every single impact. For that purpose, we combined the propagator matrix formalism to represent the layered helicoidal structure, with Bloch-Floquet periodic boundary conditions to account for the spatial periodicity. Using this approach, we were able to identify a dispersive response, with related bandgaps, for propagation modes related to shear waves. These frequency bandgaps were also shown to correspond with the characteristic frequency bands generated from the stress pulse experienced by the dactyl club during the stomatopod's hunting activities. In order to quantify the potential filtering effect of such periodic microstructure, we have also conducted a parametric analysis to study the variation of the fraction of transmitted energy with the number of layers that conforms a representative material cell. We varied the ratio of pitch distance to incident wavelength, D/λ , and the ratio between the layer thickness and the incident wavelength, d/λ . These values undoubtedly govern the number of layers N and pitch angle α , which are part of the microstructural design. For values of D/λ between 0.005 - 0.23 and for a number of layers sufficiently large ($N > 10$), which is presumed to be found within the dactyl club, we found fractions of transmitted energy in the range 0.7 - 1.0. It is thus concluded that in addition to possible inelastic and damage effects, the dactyl club appears to have the ability to sustain high intensity dynamical loads through a shear wave filtering capability introduced by the periodic nature combined with the chirality of its hierarchically arranged microstructure. Lessons from

this study could provide relevant design guidelines for the fabrication of biomimetic impact-tolerant fiber-reinforced composite materials. Future work will focus on employing these models to make predictions and optimize composite designs for very specific applications. Certainly, how efficient the composite will be to absorb energy will depend on the impact conditions. As such, optimum pitch angle, D and d can be determined if the frequency spectrum of the impact is fully understood.

Herringbone pattern modeling:

Due to the mineralization process, the Bouligand structure present in the impact region is shaped into what is known as Herringbone pattern. Figure 87 presents a multiscale representation of these microstructures. Figure 87a shows polarized light micrographs of the impact region showing the herringbone pattern. Figure 87B highlights the SEM micrograph showing the herringbone pattern observed within the bulk of the impact region as a result of rotating fibers. We used this design to form a schematic model (Figure 87C) for the fibers following the Herringbone pattern.

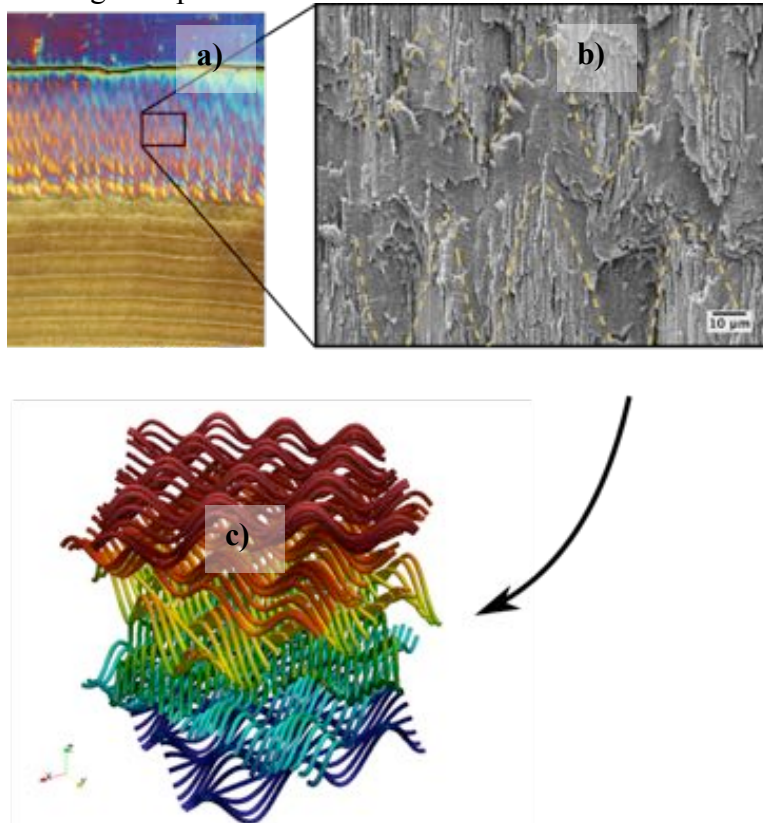


Figure 87. Multiscale model for the Herringbone pattern. a) Polarized light micrographs of the impact region showing the herringbone pattern. b) Region showing the herringbone pattern observed within the bulk of the impact region as a result of rotating fibers. c) Schematic model for the fibers following the Herringbone pattern.

We propose that the original microstructure is a common Bouligand structure that buckles forming a Herringbone pattern, as presented in Figure 88.

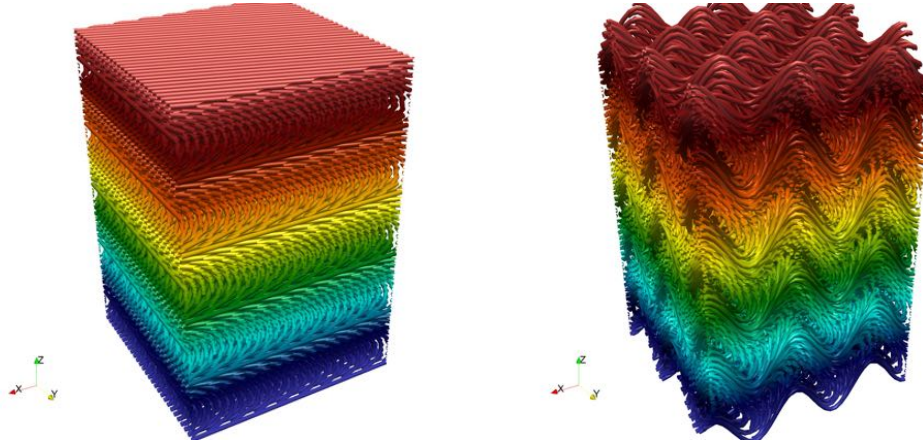


Figure 88. Bouligand structure and its equivalent Herringbone pattern.

Beyond the tasks set out at the beginning of this project, we also looked to transition some of this work to more practical application. Thus, our biomimetic composites were implemented into curved structures (Figure 89). Here, a fiberglass layup was draped over a construction helmet to show that helmets could be fabricated with the helicoidal design. The helmet was also coated with iron oxide/alumina platelets for a hard outer surface. We have made additional helmets and are looking at making more robust and complex composite parts.

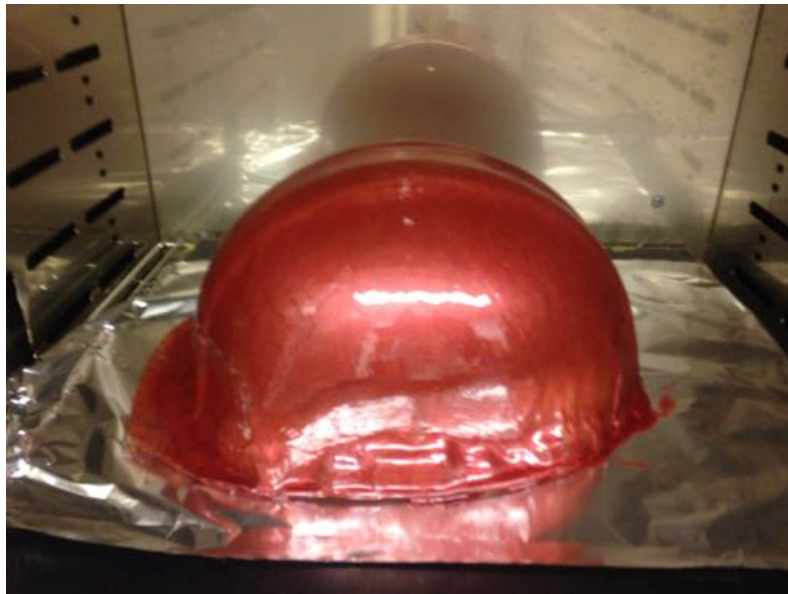


Figure 89. Composite helmet fabricated in the Kisailus Lab at UCR.

In addition, we are now utilizing an electrospinner (acquired through this project) to reduce the fiber diameters in order to make unidirectional fiber sheets that can be stacked into composite structures and subsequently tested for strength and toughness. In the final year of this project, we have electrospun both polyvinyl alcohol (PVA) and polyacrylonitrile (PAN) (Figure 90). By

varying the polymer concentrations, voltage, spinning rate and distance to target, we have been successful in spinning large area unidirectional sheets of nanofibers. These nanofiber sheets are now being annealed (Figure 91) and implemented into composites on a follow up project.

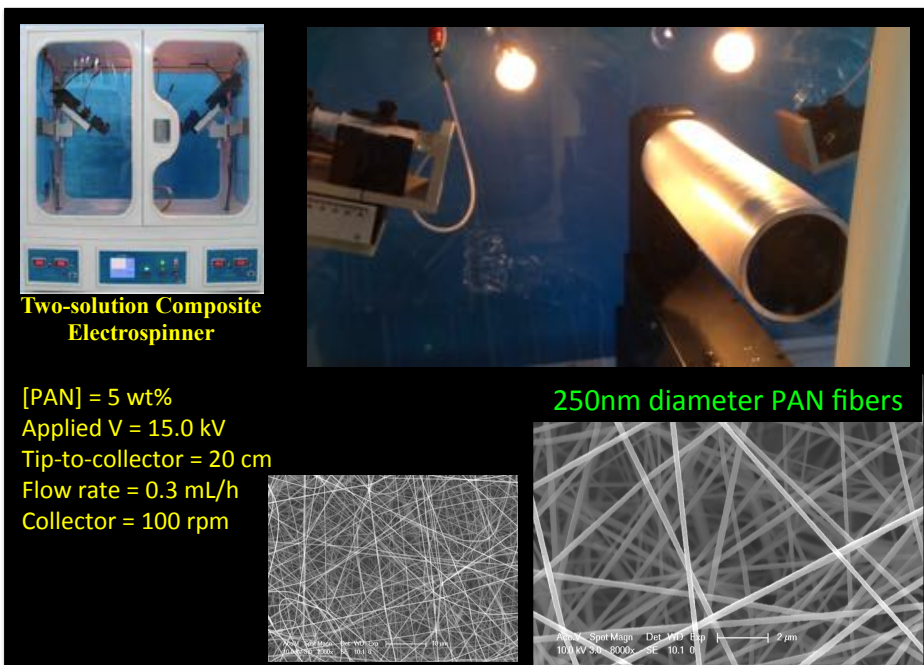
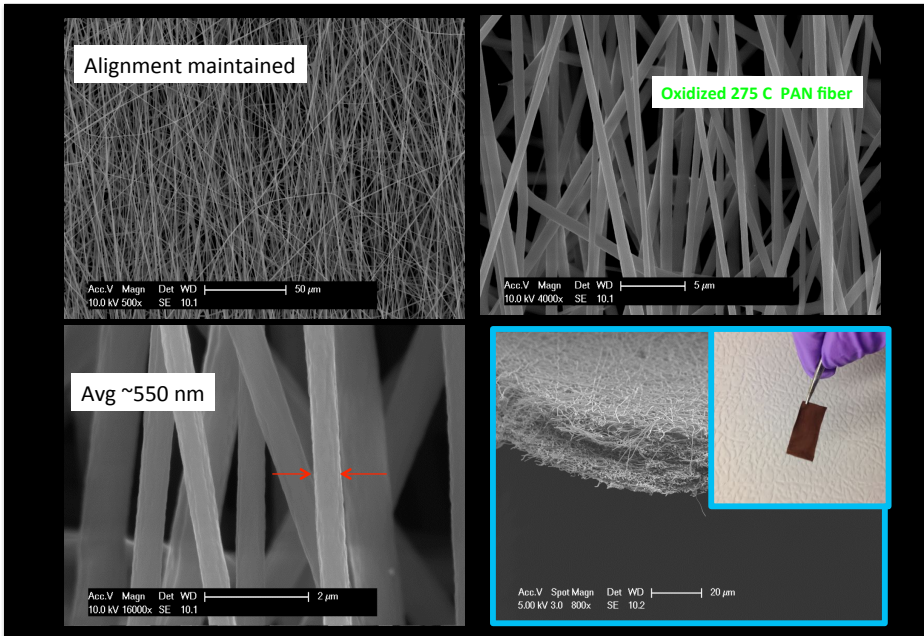


Figure 90.
 Electrosinning of
 PAN nanofibers.



**Figure 91. Highly
 aligned PAN
 nanofibers.
 Annealing and
 stacking of layers
 achieved.**

Conclusions:

We have been able to achieve many of the tasks that we aimed to complete and some that were not in the original proposal. We have uncovered the structure and function of multiple regions within the dactyl club provided insight by using a combination of biomimicry and modeling. We have gone beyond these tasks and developed scaled up versions of biomimetic composites that show performance greater than used in commercial aircraft and can be extended to many applications. Our modeling of wave propagation in the Bouligand structures can also be applied to man-made composites. Possible applications are found in helmets for sports and military protection. Since the duration of the impact is one of the key parameters, since it determines most of the frequency content in the spectrum of the pulse. Thus, designs for next generation composites will consider this.

Table 2. Duration for different impact events.

Event	Duration (ms)
Tennis ball	3.5 – 5
Hockey helmet	~ 6
Football	~ 10
Stomatopod (experiment)	1.6×10^{-1}
Stomatopod (simulation)	1.4×10^{-2}

Future work will provide the necessary design guidelines to manufacture the right composite architectures/layouts that can satisfy different functions.

In fact, our work on electrospinning nanofibers is geared towards making thinner, lighter composites from a myriad of starting materials and thus the application space is unlimited.

One task that we are still investigating is trying to uncover the hierarchical design of the helicoidal scaffold that templates a matrix of amorphous mineral, and how it may assemble via a cholesteric-like mechanism from high aspect ratio fibers.

Finally, we would like to express our sincerest gratitude to Dr. Hugh DeLong, whose support and guidance during this program made this project an overwhelming success. It has enabled fundamental research to be carried out and transitioned to practical application for many Department of Defense applications.

Supported Personnel and Collaborations: Training, Education, and Outreach Achievements

Training, Education, and Outreach Achievements

Kisailus:

- Dr. Lessa Grunenfelder (Ph.D., USC) was a post-doc working on the project.
- Dr. Garrett Milliron (BS, UC Santa Barbara), received his PhD working on the project.
- Mr. Christopher Salinas (BS, UC Riverside), was a PhD student working on the project.
- Mr. Nicholas Yaraghi (BS, U Maryland), was a PhD student working on the project.
- Mr. Steven Herrera (BS, UC Riverside), was a PhD student working on the project.

Undergraduate students: Brian Macdonald, Cyril Jose, Caleb Mohrhauser, Sherri Huo, Jesus Rivera, Charlotte Grigorian, Jeniene Abugherir, Wesley Dong, Jessica Hernandez, Chien Huang, Steven Herrera, Brian Weden, Allen Muntean, Kevin Chan, Joseph Fiore, Megan Landon.

We have had more than 30 groups (elementary, high school, community college students) tour the UCR lab throughout the project.

Zavattieri:

Graduate students:

- Main Student working on this project: Nobphadon Suksangpanya (The entire project)
- Nicolas Guarin (funded from other sources)
- David Restrepo (minimum involvement, funded from other sources)
- Fernando Cordisco (1 semester)

Undergraduate Students

- Michael Jones (Summer Undergraduate Research Fellowships-SURF program Summer 2014)
- Chaoyi Chang – Spring 2013

UCR/Purdue Media coverage/Press Releases:

Discovery Channel (February 2014): Daily Planet

Washington Post Full page story (April 26, 2014, Page 3):

http://www.washingtonpost.com/national/health-science/peacock-mantis-shrimps-swift-deadly-punch-inspires-superstrong-composite-materials/2014/04/26/ef5aa6a6-cc7f-11e3-95f7-7ecdde72d2ea_story.html

National Geographic (May 2015): "Everything You Didn't Know About Animals" featuring the mantis shrimp and Kisailus interview on The National Geographic Wild Channel.

https://www.youtube.com/watch?v=_8K3bx42jVM

<http://qa.tested.com/science/496090-biomimetics-studying-striking-power-mantis-shrimp/>

<http://www.foxnews.com/tech/2014/04/24/shrimps-inspire-stronger-materials-for-airplanes-armor/>

<http://www.gizmag.com/mantis-shrimp-super-tough-composite-materials-uc/31768/>

<http://slashdot.org/submission/3512437/punching-mantis-shrimp-inspires-super-tough-composites>

<http://www.buzzfeed.com/kellyoakes/mantis-shrimp-are-made-of-stronger-stuff-than-aeroplanes>

<http://www.iflscience.com/technology/mantis-shrimp-inspired-material-stronger-airplanes?sf2693458=1#OWVkwqoX1FYrjVzo.99>

http://www.washingtonpost.com/national/health-science/peacock-mantis-shrimps-swift-deadly-punch-inspires-superstrong-composite-materials/2014/04/26/ef5aa6a6-cc7f-11e3-95f7-7ecdde72d2ea_story.html

top of NSF home page - <http://nsf.gov/index.jsp>

<http://www.foxnews.com/tech/2015/01/10/look-back-at-some-military-tech-innovations-2014/>

Mantis Science paper:

http://www.nytimes.com/2012/06/12/science/peacock-mantis-shrimp-has-a-knockout-punch.html?_r=0

<http://articles.latimes.com/2012/jun/08/science/la-sci-0609-strong-shrimp-claws-20120609>

<http://news.discovery.com/animals/endangered-species/peacock-mantis-shrimp-claw-120607.htm>

<http://www.csmonitor.com/Science/2012/0608/How-a-shrimp-s-200-lb.-punch-could-lead-to-better-football-helmets>

<http://cen.acs.org/articles/90/i24/Peacock-Shrimp-Packs-Punch.html>

<http://www.reuters.com/video/2012/06/26/feisty-crustaceans-strength-could-be-key?videoId=236190201>

<http://www.nbclearn.com/sciencenews/cuecard/63288>

<https://engineering.purdue.edu/CE/AboutUs/News/Features/materials-research-based-on-mantis-shrimp>]

<http://www.sciencedaily.com/releases/2012/06/120607142355.htm>]

<http://blogs.discovermagazine.com/notrocketscience/2012/06/07/how-mantis-shrimps-deliver-armour-shattering-punches-without-breaking-their-fists/#.UPwLQzm6h60>]

<http://www.livescience.com/20811-hard-hitting-crustacean-claw-engineering.html>]

<http://www.scientificamerican.com/podcast/episode.cfm?id=hulk-take-break-shrimp-smash-12-06-07>

<http://www.alaskadispatch.com/article/bam-how-shrimps-200-lb-punch-could-lead-better-football-helmets>]

<http://www.purdue.edu/newsroom/purduetoday/releases/2013/Q2/purdue-civil-engineers-increasingly-look-to-nature-to-improve-material-performance.html>

<https://engineering.purdue.edu/CE/AboutUs/News/ImpactCE/CE-Impact-Spring-2013.pdf>

<http://machinedesign.com/materials/smart-materials-stem-nature>

<http://www.purdue.edu/newsroom/releases/2014/Q3/conference-returns-to-purdue-after-51-years.html>

<http://ucrtoday.ucr.edu/21729>

<http://www.naefrontiers.org/Media/PressReleases16984/45548.aspx>

<http://www.purdue.edu/newsroom/releases/2015/Q2/creatures-dactyl-club-filters-shear-waves-to-resist-damage.html> , <http://phys.org/news/2015-06-creature-dactyl-club-filters-resist.html>

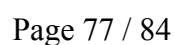
<http://ucrtoday.ucr.edu/29973> ,

<http://www.sciencedaily.com/releases/2015/06/150617144502.htm>

Finally, UCR hosted 3 outreach events (1 per year) at the Riverside Metropolitan Museum in May of 2013, 2014 and 2015. [**https://riversideca.gov/museum/design-by-nature.asp**](https://riversideca.gov/museum/design-by-nature.asp)

In each year, approximately 10 of my 12 undergraduates working in the Biomimetics and Nanostructured Materials Lab presented their research to a public audience. IN addition for each year, we had 10-15 middle school students from Mira Loma middle school working with our undergraduates in the lab to develop demonstrations that the public could understand. Thus, at the museum event, both undergraduates and middle school students co-presented to the public.

The program for this event is shown below:



Collaborators:

Air Force Lab:

Dr. Rajesh Naik was a collaborator on the project. Dr. David Mollenhauer (AFRL) is a new collaborator helping with 3D weaving.

Northwestern University:

Prof. Horacio Espinosa is a new collaborator working on impact resistant materials.

UC Berkeley:

Prof. Rob Ritchie is a collaborator working on impact resistant materials.

UC Riverside:

Prof. Cheryl Hayashi is a collaborator working on high strength fibers for biomimetic composites. Prof. Nigel Hughes is a collaborator working on investigating trilobites.

UC San Diego:

Dr. Dimitri Deheyn was and is a collaborator. We have been investigating the ultrastructural features and mechanical properties of a bioluminescent snail (*Hinea*).

Prof. Joanna McKittrick is a new collaborator working on impact resistant materials.

Prof. Marc Meyers is a new collaborator working on impact resistant materials.

University of Western Sydney:

Dr. Ric Wuhler is a new collaborator helping with high resolution EDS mapping

Publications:

“Biological and Biomimetic Composites,” *CAMX-Conference on Composites and Advanced Materials Expo*. Dallas, Texas, October 26-29, 2015. American Composites Manufacturers Association & Society for the Advancement of Material and Process Engineering, ***accepted***.

“Shear Wave Filtering in Naturally-Occurring Bouligand Structures,” Nicolás Guarín-Zapata, Juan Gomez, Nick Yaraghi, D. Kisailus, Pablo D. Zavattieri, *Acta Biomaterialia*, **23**, (2015) 11-20.

“Crustacean-derived biomimetic components and nanostructured composites,” L.K. Grunenfelder, S. Herrera, D. Kisailus, *Small*, **10** (16) (2014) 3207-3232. DOI: 10.1002/smll.201400559.

“Bio-Inspired Impact Resistant Composites,” L.K. Grunenfelder, N. Suksangpanya, C. Salinas, G. Milliron, N. Yaraghi, S. Herrera, K. Evans-Lutterodt, S.R. Nutt, P. Zavattieri, D. Kisailus, *Acta Biomaterialia*, **10** (9) (2014) 3997-4008. DOI: 10.1016/j.actbio.2014.03.022

“Fracture mitigation strategies in gastropod shells,” C. Salinas and D. Kisailus, *Journal of Materials*, **65** (4) (2013) 473-480. DOI: J10.1007/s11837-013-0570-y

“Ecologically driven ultrastructural and hydrodynamic designs in stomatopod cuticles,” L.K. Grunenfelder, G. Milliron, S. Herrera, I. Gallana, N. Yaraghi, N.C. Hughes, K. Evans-Ludderodt, P. Zavattieri, D. Kisailus, (to be submitted).

“Modified Bouligand Structure Enhances Stress Redistribution in the Stomatopod Dactyl Club Exocuticle,” N. Yaraghi, et al. (to be submitted).

“Theoretical analysis of Twisted Crack based on Linear Elastic Fracture Mechanics,” N. Suksangpanya et al. (in preparation).

“Fracture Analysis on the Bouligand Structure in Stomatopod Dactyl Club under mode I Uniaxial Loading,” N. Suksangpanya et al. (in preparation)

Invited paper to *Annual Review of Physical Chemistry* on “Biomimetic Materials,” ***in prep.***

Invited paper to *Chemical Society Reviews* on “Structure-property relationships in an impact tolerant bio-composite,” ***in prep.***

Patents:

Kisailus:

A MAGNETICALLY CONTROLLED CASTING PROCESS FOR MULTISTRUCTURAL MATERIALS, US Patent Application #: 13/767,699

DEVELOPMENT OF SHOCK RESISTANT AND TOUGH MATERIALS, US Patent Application # 13/957,708.

UCR Patent disclosure: “Development of Highly Textured Compression Resistant Coatings.” UC Case No. 2015-361-1

Presentations:***Kisailus (invited):***

“Structure Function Relationships in Impact resistant biominerals,” Gordon Research Conference on Biomineralization, Girona, Spain, August 14-19, 2016.

“From Nature to Engineering: Biological, Biomimetic and Bioinspired Nanostructured Materials,” Gordon Research Conference on Structural Nanomaterials, Hong Kong, July 10-15, 2016.

“Biological and Biomimetic Composites,” Gordon Research Conference on Multifunctional Materials and Structures, Ventura, CA, January 31 - February 5, 2016.

“Convergent Evolution to Engineering: Multi-Functional Bio-composite and Biomimetic Materials,” Materials Research Society (MRS) Fall Meeting 2015, Boston, MA, Nov. 30-Dec. 5, 2015.

“Investigation of an Impact Resistant Crustacean. Part 1: Ultrastructure and Nanomechanics,” ASME 2015 4th Conference on Nanoengineering for Medicine and Biology, Minneapolis, MN, April 19-22, 2015.

“Investigation of biological and biomimetic composites”, TMS Meeting, Orlando, Florida; March 2015.

“Structure and Mechanics of the Stomatopod Dactyl Club Exocuticle”, Materials Research Society (MRS) Fall Meeting 2014, Boston, MA, Nov. 30-Dec. 5, 2014.

“Crash Avoidance and Visibility Composites Research,” Department of Transportation, Washington, DC; September 2014.

“Investigation of an Impact Resistant Crustacean Part 1: Ultrastructure and Nanomechanics,”, SEM Annual Conference & Exposition on Experimental and Applied Mechanics, Greenville, SC, USA June 1 - 5, 2014.

“From Nature to Engineering: Bio-mimetic and Bio-inspired Materials,” 19th German-American Kavli Frontiers of Science Symposium, Alexander von Humboldt Foundation, National Academy of Sciences, Irvine, California; April, 2014.

“Investigation of an impact resistant crustacean. Part 1: ultrastructure and nanomechanics”, Materials Research Society (MRS) Fall Meeting 2013, Boston, MA, Dec. 1-6, 2013.

“Damage-tolerant Composites Derived from Impact Resistant Organisms.” International Symposium on Nature Inspired Technology, South Korea; January, 2013.

"The stomatopod dactyl club: A formidable damage-tolerant biological hammer." Gordon Research Conference on Biomineralization, New London, NH; August 2012.

Kisailus (plenary/keynote):

“From Nature to Engineering: Bio-mimetic and Bio-inspired Materials,” **Plenary address.** 2nd International Fusion Materials Symposium, Tokyo, Japan; November, 2014.

“Case Studies in Biomimetics and Nanostructured Materials,” **Keynote Address.** 2nd Biomimicry Europe Innovation and Finance Summit, Zurich, Switzerland; September 2014.

“From Nature to Engineering: Bio-mimetic and Bio-inspired Materials,” **Keynote Address.** International Symposium on Biomineralization, Freiberg, Germany; August, 2013.

Zavattieri (invited):

“Size scales in biomineralized and biomimetic materials”, SEM Annual Conference & Exposition on Experimental and Applied Mechanics, Costa Mesa, CA, June, 2012.

Application of Cohesive Zone Models for Biomineralized and Biomimetic Materials”, 49th Annual Technical meeting of the Society of Engineering Science (SES), Georgia Tech on Oct. 10-12, 2012.

“Investigation of an impact resistant crustacean. Part 2: mechanics and modeling”, Materials Research Society (MRS) Fall Meeting 2013, Boston, MA, Dec. 1-6, 2013.

“*Investigation of an Impact Resistant Crustacean Part 2: Mechanics and Modeling*”, SEM Annual Conference & Exposition on Experimental and Applied Mechanics, Greenville, SC, USA June 1 - 5, 2014.

“Numerical Investigation of the Mechanics of the Dactyl Club of the Mantis Shrimp”, 17th US National Congress on Theoretical & Applied Mechanics (USNCTAM), June 15-20, 2014, Michigan State University, Lansing Michigan.

“Shear wave filtering in the Mantis shrimp’s dactyl club,” 51st Annual Society of Engineering Science (SES) Meeting, Purdue University, Oct. 2014.

“Numerical and Experimental Investigations on Biomimetic Material: Stomatopod Dactyl Club,” 51st Annual Society of Engineering Science (SES) Meeting, Purdue University, Oct. 2014.

“Toughening mechanisms in naturally-occurring helicoidal composite materials,” TMS 2015 144th Annual Meeting & Exhibition, March 15-19, 2015, Orlando, FL.

“Investigation of an Impact Resistant Crustacean. Part 2: Mechanics and Modeling,” ASME 2015 4th Conference on Nanoengineering for Medicine and Biology, Minneapolis, MN, April 19-22, 2015.

“Fracture analysis on the bouligand structure in stomatopod dactyl club,” 15th Pan-American Congress of Applied Mechanics, PACAM XV, Champaign, IL, May 18-21, 2015.

“Mechanical Investigation of Bouligand Microstructures,” 13th US National Congress on Computational Mechanics, USNCCM, San Diego, CA, July 26-30, 2015.

“Biomaterialized and Biologically-Inspired Impact Resistant Materials: Mechanics and beyond”, Poster at the fifth Indonesian-American Kavli Frontiers of Science symposium in Makassar, Indonesia, July 28-31, 2015.

Symposium SM9: Structure and Properties of Biological Materials and Bioinspired Designs 2016 MRS Spring Meeting and Exhibit, Phoenix, Arizona, March 28-1, 2016.

Zavattieri (Plenary):

“Multiscale mechanics of natural fibers”, NSF Pan American Advanced Studies Institute (PASI) on Polymer and Composite Materials from Renewable Resources and Biorefinery: from Chemistry to Applications, Costa Rica, August 2013.

“Mechanical Investigation of Biomaterialized and Biologically-Inspired Materials: Lessons learned from Nature,” International Seminar on Biomaterials, Biomechanics and Regenerative Medicine, RutaN, Medellin, Colombia, May 16, 2014.

"Numerical Investigation of Naturally-Occurring High Performance Materials", XXI Congress on Numerical Methods and their Applications (ENIEF 2014), San Carlos de Bariloche, Argentina 23th-26th September 2014.

“Combined 3D Printing and Multi-scale Modeling for the Development of Biomimetic Materials”, Multiscale/3D Printing Cement Workshop, Vanderbilt University, July 16-17, 2015.

“Combined 3D Printing and Multi-scale Modeling for the Development of High Performance Biomimetic Materials”, Seminar of Nanosurfaces: Advanced Processing and Characterization – II International Seminar on Biomaterials, Biomechanics and Regenerative Medicine, RutaN, Medellin, Colombia, Sept. 16-18, 2015.

Zavattieri Seminars:

“Mechanical investigation of naturally-occurring high performance materials”, Stanford University, March 14, 2013.

Mechanical Investigation of Biomaterialized and Biologically-Inspired Materials: Lessons learned from Nature, EAFIT University, Medellin, Colombia, May 19, 2014.

Mechanical Investigation of Naturally-Occurring High Performance Materials: Lessons learned from Nature, Whistler Center for Carbohydrate Research, Purdue University, May 30, 2014.

Naturally-Occurring High Performance Materials: Lessons learned from Nature, Biomimicry Group, Arizona State University, March 26, 2014 (via teleconference).

Investigación de la Mecánica de Materiales Compuestos Naturales y Biomiméticos de Alto Rendimiento, Universidad Nacional de La Plata, La Plata, Argentina, June 26, 2015.

Zavattieri Short Courses at other universities:

“*Biomimetic Materials*” short course (~10 hours), Universidad del Norte, Barranquilla, Colombia, as part of the doctorate program, Monday, May 12 to Wednesday, May 14, 2014

Awards/Achievements:

Kisailus:

Early Promotion to Full Professor (2015)

Nick Yaraghi (Kisailus PhD student): NDSEG Fellowship (2015)

Awarded Kavli Fellow of the National Academy of Sciences (2014)

Promotion (Tenured) (2013)

Endowed Chair: Winston Chung Endowed Chair of Energy Innovation, UC Riverside

Zavattieri:

Recipient of the NSF Faculty Early Career Development (NSF CAREER) award, 2013.

IM:PACT (Instruction Matters: Purdue Academic Course Transformation) fellow, 2013.

Recipient of the Roy E. & Myrna G. Wansik Research Award. Purdue University, 2013.

Early Tenure awarded, 2014.

National Academy of Engineering (NAE), US Frontier of Engineering (USFOE) Symposium Alumn, 2014.

Purdue University Faculty Scholar, 2015

Kavli Frontier of Science Fellow of the National Academy of Science (NAS), 2015

Interactions/Transitions:

Kisailus:

We have established relationships with Airbus, Boeing, DOT, TALOS – to initiate collaboration

Acquisition of Nanoindenter via AFOSR-DURIP, capable of large area indentation

Acquisition of FTIR microscope via ARO-DURIP, capable of large area mapping

Acquired new fiber and composite mechanical testing unit, electrospinner, muffle furnace (AFOSR)

Acquired new 300W laser sintering 3D printer (open source, ceramic and metals)

Conference Organization:

Symposium Organizer, MRS, Spring 2016

Executive Committee of the American Association for Crystal Growth (2015-2018)

Chairing Session on Multifunctional Materials at 20th Int'l Conference on Composite Materials (July 2015)

Conference Chair, American Association for Crystal Growth, June 2014

Conference Organizer, American Association for Crystal Growth, June 2012

Zavattieri:

Active Member of the Society of Hispanic Professional Engineers (SHPE).

- Chair: 2012 - 2014 SHPE Undergraduate and Graduate Student Technical Paper Competition.
- Chair of paper presentations for SHPE Research and Innovation in STEM (RISE) Symposia

Organization of symposia where the work of this project was presented:

2nd International symposium on the mechanics of biological systems and materials, as part of the SEM XII International Congress and Exposition on Experimental and Applied Mechanics, June 2012.

“Computational Modeling of Damage and Fracture in Solids,” 49th Annual Technical Meeting of Society of Engineering Sciences (SES), Georgia Tech, Atlanta GA, Oct. 10-12, 2012.

3rd International symposium on the mechanics of biological systems and materials, as part of the SEM XIII International Congress and Exposition on Experimental and Applied Mechanics, June 2013.

“Material Design and Biomimetic Material Concepts,” 50th Annual Technical Meeting of Society of Engineering Sciences (SES), Brown University, Providence, RI, July 28-31, 2013.

“Computational and Experimental Investigations of Bio-Inorganic Interfaces” in the Biological and Biomimetic Materials track for the 2014 Society of Engineering Science (SES) 51st Annual Technical Meeting, Purdue University, Oct. 1-3, 2014.

“Bridging Scales in Heterogeneous Materials,” MRS Fall Meeting, 2014

“Multiscale Mechanics of Biological and Bioinspired Material,” ASME 2015 4th Conference on Nanoengineering for Medicine and Biology, Minneapolis, MN, April 19-22, 2015

Conference Organization:

Main organizer and Secretary of the 51st Society of Engineering Science (SES) Annual Technical SES at Purdue 2014

Track organizers (for Biological and Biomimetic Materials and the Mechanics of Solids Tracks), and Symposium organizer.

1.

1. Report Type

Final Report

Primary Contact E-mail**Contact email if there is a problem with the report.**

david@engr.ucr.edu

Primary Contact Phone Number**Contact phone number if there is a problem with the report**

951-827-4310

Organization / Institution name

UC Riverside

Grant/Contract Title**The full title of the funded effort.**

Uncovering and Validating Toughening Mechanisms in High Performance Composites

Grant/Contract Number**AFOSR assigned control number. It must begin with "FA9550" or "F49620" or "FA2386".**

FA9550-12-1-0245

Principal Investigator Name**The full name of the principal investigator on the grant or contract.**

David Kisailus

Program Manager**The AFOSR Program Manager currently assigned to the award**

Dr. Hugh DeLong

Reporting Period Start Date

05/15/2012

Reporting Period End Date

05/14/2015

Abstract

Based on the three years of this project, we have been largely successful in staying on schedule and achieving the milestones outlined in the proposal. The research goal of this project is to study and understand the structure-function relationships in damage-tolerant impact/shock-resistant stomatopod dactyl club while addressing the ongoing quest to develop the new generation of scalable high-performance biologically-inspired multifunctional materials. We achieved this by (i) providing details of the nano- and microstructural features of the stomatopod dactyl clubs with state-of-the-art microscopy and synchrotron x-ray studies, (ii) deriving the structure-property relationship through a combined experimental/computational methodology to properly characterize the mechanical properties of the different regions of the dactyl club and (iii) studying the multiscale hierarchical structure of the periodic region to elucidate critical energy and shock mitigation mechanisms. Our ultrastructural investigations have identified that within this multi-regional composite structure, specific regions play very specific roles. We uncovered structural details from the striated region, which exists on the sides of the club. Unidirectional mineralized fibers in this region wrap circumferentially around the club, keeping it under compression during impact and preventing crack growth. To confirm this, we produced new models at multiple length scales and across length scales to show the effects of this outer layer. We compared this to the spearing dactyl of another species of mantis, in which this striated region is located on all sides (supporting flexural loads).

We also observed a unique structure within the impact region of the dactyl. Specifically, the helicoidal structure previously identified in the periodic region extended into the impact region with a change in periodicity and forming a herringbone-like structure based on compression of this helicoid. Evidence is provided for the effects of this “herringbone structure”, which in combination with an outer dense particulate apatite layer, enhances stress redistribution under compressive loading. Within the periodic region, which contains the helicoidal structure, we observed that the periodicity enables not only crack twisting (as demonstrated by models and 3D printed samples), which toughens the club, but also shear wave filtering, as confirmed using analytical models. In addition, we have fabricated carbon fiber based biomimetic composites that recreate the structure within periodic region in order to highlight its ability to absorb energy by redistributing impact. These biomimetic composites outperformed those used in the aircraft industry (e.g., quasi-isotropic found in Boeing and Airbus commercial aircraft) by 49% (based on dent-depth) and more than 15% higher compressive strength after impact. We have also identified macro-morphological designs that reduce hydrodynamic drag over ballistic forms and initiated observations for the telson and merus regions of the mantis. We have published multiple papers in high impact journals, graduated multiple Ph.D. students, mentored post-doctoral and undergraduate students and held outreach events involving middle school students and the general public. Finally, new interactions with other investigators have lead to new research directions.

Distribution Statement

This is block 12 on the SF298 form.

Distribution A - Approved for Public Release

Explanation for Distribution Statement

If this is not approved for public release, please provide a short explanation. E.g., contains proprietary information.

SF298 Form

Please attach your SF298 form. A blank SF298 can be found [here](#). Please do not password protect or secure the PDF. The maximum file size for an SF298 is 50MB.

[AFD-070820-035-SF298.pdf](#)

Upload the Report Document. File must be a PDF. Please do not password protect or secure the PDF. The maximum file size for the Report Document is 50MB.

[AFOSR report-Mantis-Kisailus-FA9550-12-1-0245-Final copy reduced.pdf](#)

Upload a Report Document, if any. The maximum file size for the Report Document is 50MB.

Archival Publications (published) during reporting period:

“Biological and Biomimetic Composites,” CAMX-Conference on Composites and Advanced Materials Expo. Dallas, Texas, October 26-29, 2015. American Composites Manufacturers Association & Society for the Advancement of Material and Process Engineering, accepted.

“Shear Wave Filtering in Naturally-Occurring Bouligand Structures,” Nicolás Guarín-Zapata, Juan Gomez, Nick Yaraghi, D. Kisailus, Pablo D. Zavattieri, Acta Biomaterialia, 23, (2015) 11-20.

“Crustacean-derived biomimetic components and nanostructured composites,” L.K. Grunenfelder, S. Herrera, D. Kisailus, Small, 10 (16) (2014) 3207-3232. DOI: 10.1002/sml.201400559.

“Bio-Inspired Impact Resistant Composites,” L.K. Grunenfelder, N. Suksangpanya, C. Salinas, G. Milliron, N. Yaraghi, S. Herrera, K. Evans-Lutterodt, S.R. Nutt, P. Zavattieri, D. Kisailus, Acta Biomaterialia, 10 (9) (2014) 3997-4008. DOI: 10.1016/j.actbio.2014.03.022

“Fracture mitigation strategies in gastropod shells,” C. Salinas and D. Kisailus, Journal of Materials, 65 (4) (2013) 473-480. DOI: 10.1007/s11837-013-0570-y

Changes in research objectives (if any):

None.

Change in AFOSR Program Manager, if any:

None.

Extensions granted or milestones slipped, if any:

None.

AFOSR LRIR Number

LRIR Title

Reporting Period

Laboratory Task Manager

Program Officer

Research Objectives

Technical Summary

Funding Summary by Cost Category (by FY, \$K)

	Starting FY	FY+1	FY+2
Salary			
Equipment/Facilities			
Supplies			
Total			

Report Document

Report Document - Text Analysis

Report Document - Text Analysis

Appendix Documents

2. Thank You

E-mail user

Sep 11, 2015 11:47:59 Success: Email Sent to: david@engr.ucr.edu